Technical Report

CREATION AND DEPLOYMENT OF THE NEREUS AUTONOMOUS UNDERWATER CHEMICAL ANALYZER AND KEMONAUT, AN ODYSSEY CLASS SUBMARINE

Richard Camilli

MITSG 03-32TH

MIT Sea Grant College Program

Massachusetts Institute
of Technology
Cambridge, Massachusetts
02139

CREATION AND DEPLOYMENT OF THE NEREUS AUTONOMOUS UNDERWATER CHEMICAL ANALYZER AND KEMONAUT, AN ODYSSEY CLASS SUBMARINE

Richard Camilli

MITSG 03-32TH

Sea Grant College Program
Massachusetts Institute of Technology
Cambridge, Massachusetts 02139

NSF Grant No.: EAR-0330272

Creation and Deployment of the NEREUS Autonomous Underwater Chemical Analyzer and Kemonaut, an Odyssey Class Submarine

by

Richard Camilli

B.A., Biology (1996)
Cheyney University

M.S., Civil and Environmental Engineering (2000)
Massachusetts Institute of Technology

Submitted to the Department of Civil and Environmental Engineering
In Partial Fulfillment of the Requirements for the Degree of
Doctor of Philosophy in Civil and Environmental Engineering

at the

Massachusetts Institute of Technology

June 2003

Signature of Author.....
Department of Civil and Environmental Engineering
November, 2002

Certified by .....
Harold F. Hemond
Professor of Civil and Environmental Engineering
Thesis Supervisor

Accepted by.....
Oral Buyukozturk
Chairman, Departmental Committee on Graduate Studies

Creation and Deployment of the NEREUS Autonomous Underwater Chemical Analyzer and Kemonaut, an Odyssey Class Submarine

by

Richard Camilli

Submitted to the Department of Civil and Environmental Engineering
on March 27, 2003 in partial fulfillment of the requirements for
the Doctor of Philosophy in Civil and Environmental Engineering

ABSTRACT:

NEREUS is a compact self-contained low-power submersible membrane-inlet mass spectrometer, designed to measure dissolved volatile gasses in the water column. It is capable of intelligent data collection, analysis and state-based mission control while operating as a stand-alone instrument or onboard the Kemonaut autonomous underwater vehicle (AUV). Kemonaut is an Odyssey class AUV with increased payload carrying capacity and dynamic stability, and is intended for freshwater and coastal marine applications to depths of 300 meters. The NEREUS-Kemonaut system characteristics allow for greatly improved dissolved gas data collection rates, accuracy and mapping resolution over presently available technologies. Applications particularly well suited for the NEREUS-Kemonaut system include identification and mapping of pollution sources such as chemical spills, investigation of enigmatic freshwater and marine ecosystems, assessment of subsurface natural resources and estimation of marine-related greenhouse gas cycling.

A gift is pure when it is given from the heart to the right person at the right time and at the right place, and when we expect nothing in return.

The Bhagavad Gita

To my mother

(This is kind of hefty, so I made a special refrigerator magnet to go with it. See section 2.2.1)

TABLE OF CONTENTS

Chapter 1 INTRODUCTION 15
1.1 Autonomous machines 16
1.2 Autonomous underwater vehicles 17
1.3 Mass spectrometry 19
1.4 Autonomous In-situ mass spectrometry 20
1.5 Applications 24
1.6 System performance 26
Chapter 2 MECHANICAL AND ELECTRONIC HARDWARE 27
2.1 Vacuum system 28
2.1.1 Vacuum envelope 28
2.1.2 Inlet apparatus 29
2.1.3 Ion pump 32
2.2 Analyzer 34
2.2.1 Analyzer magnet 35
2.2.2 Cycloid analyzer 37
2.3 Electronic Control 41
2.3.1 Embedded computer 42
2.3.2 Communication 42
2.3.3 Data acquisition and instrument control 43
2.3.4 Mass Selector 44
2.3.5 Emission regulator 47
2.3.6 Electrometer 49
2.4 Power system 60
2.5 Component housings, frame, and mounting apparatus 62
2.5.1 Frame 63
2.5.2 Mounting plate 64
2.5.3 Instrument cover 65
2.5.4 Attachment disk 66
2.5.5 Electronics housings 67
2.5.6 Hardhat protector 68
2.6 Instrument startup and sphere sealing 70
Chapter 3 SOFTWARE 73
3.1 Embedded Code 73
3.1.1 Embedded display and user interface 74
3.1.2 Instrument Control 76
3.1.3 Calibration 77
3.1.4 Operational modes 80
3.1.5 Signal Averaging 81
3.1.6 Data handling 82
3.1.7 Data storage 82
3.2 Supervisory control 83
3.2.1 Communications protocol 84
3.3 Remote Graphical User interface 86

3.3.1 Main window 87
3.3.2 Command initialization 88
3.3.3 Data parsing 89
3.3.4 Data visualization 90
3.3.5 Data storage and retrieval 93
3.4 Quantitative peak evaluation 94
Chapter 4 AUTONOMOUS UNDERWATER VEHICLE DESIGN 97
4.1 Odyssey II design overview 98
4.2 Odyssey III design 101
4.3 Kemonaut development 101
4.3.1 Design and construction 103
4.3.2 Control and navigation 109
4.3.3 Assembly 109
4.3.4 Stability and ballasting 112
Chapter 5 NEREUS BENCH TESTING 115
5.1 Dissolved gas gradient sampling 118
5.2 Computerized operation and noise analysis 120
5.3 Instrument sensitivity 124
5.4 Ion fragmentation 125
5.5 Temperature associated peak height variation 126
5.5.1 Temperature dependent detection limits 128
5.6 Variability in ion pump efficiency 130
5.7 Instrument response time 132
5.8 Submerged testing 137
Chapter 6 DEPLOYMENT AND SEA TRIALS 139
6.1 Tethered deployments 139
6.2 Towed deployment 150
6.3 AUV deployment 157
Chapter 7 CONCLUSIONS AND FUTURE WORK 167
7.1 Toward routine operation 168
7.2 System optimization 169
7.3 Sensor integration and real-time data interpretation 170
7.4 Future prototypes 171
REFERENCES 173
NEREUS CIRCUIT DIAGRAM 181
NEREUS EMBEDDED CODE 183
THETIS SPECTRAL VIEWER CODE 203
NEREUS DATA INTERPRETER CODE 253

TABLE OF FIGURES

Figure 1-1: Rendering of the Kemonaut AUV 19
Figure 1-2:NEREUS instrument pictured beside laboratory microscope 24
Figure 2-1: The NEREUS instrument with upper glass hemisphere removed 27
Figure 2-2: Vacuum Envelope cutaway view 29
Figure 2-3: Membrane compression and sagging resulting from hydrostatic pressure 30
Figure 2-4: Sample inlet apparatus 31
Figure 2-5: Ion pump, cycloid and vacuum envelope assembly 33
Figure 2-6: Machined ion pump housing 34
Figure 2-7: Asymmetrically shaped analyzer magnet 36
Figure 2-8: Ion trajectory of cycloidal mass analyzer 37
Figure 2-9: NEREUS cycloid tube constructed from a modified CEC 21-620 39
Figure 2-10: Conflat flange with dual BNC feed through 41
Figure 2-11: Scan controller detail 46
Figure 2-12: Software controlled emission regulator on/off relay 48
Figure 2-13: Teledyne parametric op-amp electrometer design by Hemond 50
Figure 2-14: Optimal feedback resistor value 51
Figure 2-15: NEREUS electrometer circuit 53
Figure 2-16: Electrometer sensitivity vs. sampling frequency 54
Figure 2-17: NEREUS electrometer 55
Figure 2-18: Electrometer shielding and mounting 56
Figure 2-19: Power spectral density of electrometer with and without compensator 57
Figure 2-20: Cross correlation of electrometer noise with and without compensation 58
Figure 2-21: Power spectrum density comparison of NEREUS and Hemond-Teledyne electrometers 59
Figure 2-22: Layout of NEREUS components within pressure sphere 63
Figure 2-23: NEREUS instrument frame 64
Figure 2-24: Mounting plate placement of analyzer, detector and ion pump assemblies. 65
Figure 2-25: Composite instrument cover 66
Figure 2-26: Embedded computer with memory card 68
Figure 2-27: The NEREUS instrument, sealed within its pressure housing 69
Figure 3-1: Remote calibration GUI for NEREUS instrument 78
Figure 3-2: Valid command string example 85
Figure 3-3: Thetis Spectral Viewer login window 87
Figure 3-4: Thetis Spectral Viewer main window 88
Figure 3-5:Thetis GUI command radio button fields and tool bar 89
Figure 3-6: Thetis GUI status bar 89
Figure 3-7: Thetis GUI histogram field with red temporal window 91
Figure 3-8:Thetis GUI spectrum field 92
Figure 3-9: Thetis Spectral Viewer main window with data table visible 93
Figure 3-10: NEREUS Peak Interpreter GUI 94
Figure 4-1: Odyssey I vehicle (courtesy of MIT Sea Grant) 98
Figure 4-2: Odyssey IId Xanthos AUV 100
Figure 4-3: MIT Sea Grant Odyssey III Caribou AUV 101

Figure 4-4:Glass pressure sphere placement within the Kemonaut AUV 104
Figure 4-5: Cut-away view of Kemonaut, exposing upper floatation foam and lift harness 107
Figure 4-6: Exploded diagram of Kemonaut vehicle components 108
Figure 4-7: Positioning of the NEREUS instrument within the Kemonaut forward payload bay 110
Figure 4-8: Partially assembled Kemonaut, showing the NEREUS instrument and composite girder 111
Figure 4-9: Structural integrity test of fully laden Kemonaut vehicle 111
Figure 4-10: Kemonaut ballasting in Upper Mystic Lake 113
Figure 5-1: NEREUS setup using Keithley electrometer and 10-turn potentiometer 115
Figure 5-2: First NEREUS scan completed on January 8, 2002, showing ambient air spectrum containing water, nitrogen, oxygen, and argon peaks. 116
Figure 5-3: NEREUS ambient air spectrum using on board electrometer with $10^{10}\ \Omega$ feedback resistor 117
Figure 5-4: Measurements of dissolved gases in a synthesized gradient using Mishawum Lake water 119
Figure 5-5: Conceptual diagram of NEREUS control and data acquisition design 121
Figure 5-6: Ambient air spectrum, performed using computer control and data acquisition at mass step interval = 0.1 M/Z. This spectrum reveals the presence of nitrogen, oxygen, argon, water vapor, and carbon dioxide. 122
Figure 5-7: Comparison of typical noise characteristics of the NEREUS instrument when operated using differing signal averaging regimes 123
Figure 5-8: RMS noise versus time required for completion of a high resolution, 1385 data point, scan using a 100MHz embedded computer. 123
Figure 5-9: A high-resolution spectrum of ambient air detailing nitrogen gas and an apparent ^{14}N-^{15}N isotopic peak. 124
Figure 5-10: \Ion peak height of dissolved gases in atmospheric equilibrium as a function of temperature 127
Figure 5-11: Model of NEREUS ion peak height sensitivity as a function of temperature. Data points are normalized to NEREUS spectrum data from filtered water at 22°C. 128
Figure 5-12: NEREUS ion signal variability, recorded while submerged in a flume. Spectrum scans executed using a peak jumping algorithm. 131
Figure 5-13: Calculated overall NEREUS time to steady state measurement for various gases 134
Figure 5-14: NEREUS time response to carbon dioxide 135
Figure 5-15: Time response of Hemond backpack portable mass spectrometer to nitrogen gas 136
Figure 5-16: NEREUS time response to benzene 137
Figure 6-1: Tethered NEREUS configuration with Hydrolab 140
Figure 6-2: NEREUS spectrum from at 2 meters depth in the Halls Brook Holding Area 141
Figure 6-3: NEREUS depth profile of ion peaks in the Halls Brook Holding Area 142
Figure 6-4: Hydrolab depth profile of dissolved oxygen, salinity and temperature in the Halls Brook Holding Area 142

Figure 6-5: Location of tethered NEREUS deployment in Boston Harbor 143
Figure 6-6: Microscopic comparison of a new membrane (left), and after heat forming and deployment to 12 meters depth (right) 144
Figure 6-7: Boston Harbor spectrum at 1.5 meters depth 145
Figure 6-8: Boston Harbor spectrum at 3 meters depth 145
Figure 6-9: Boston Harbor spectrum at 4.5 meters depth 146
Figure 6-10: Boston Harbor spectrum at 6 meters depth 146
Figure 6-11: Boston Harbor spectrum at 7.5 meters depth 147
Figure 6-12: Boston Harbor spectrum at 9 meters depth 147
Figure 6-13: Boston Harbor spectrum at 10.5 meters depth 148
Figure 6-14: Boston Harbor spectrum at 12 meters depth 148
Figure 6-15: Depth profile of Boston Harbor 149
Figure 6-16: Oxygen signal correlation of NEREUS and Hydrolab data from Boston Harbor 150
Figure 6-17: 3-D map of towed NEREUS deployments in Upper Mystic Lake 152
Figure 6-18: Oxygen signal correlation of NEREUS and Hydrolab data from Upper Mystic Lake, Dec. 13 153
Figure 6-19: Oxygen signal correlation of NEREUS and Hydrolab data from Upper Mystic Lake, Dec. 15 154
Figure 6-20: Chemical profile of Upper Mystic Lake, December 15, 2002 156
Figure 6-21:The Kemonaut AUV prior to deployment in Boston Harbor 157
Figure 6-22:Nautical Chart of Boston Harbor showing GIB placement and overall area of operation 159
Figure 6-23: Kemonaut pressure transducer record 160
Figure 6-24:2-D GIB hydrophone surface track log of Kemonaut dive missions 162
Figure 6-25: 3-dimensional GIB hydrophone track log of Kemonaut dive missions 163
Figure 6-26: A typical NEREUS spectrum that was recorded while onboard the Kemonaut AUV, showing dissolved nitrogen, oxygen and argon 165
Figure 6-27: NEREUS record of dissolved gas ion signal during Kemonaut deployment in Boston Harbor 165

Table 1-1: Comparison of submersible mass spectrometer specifications 23
Table 2-1: Cycloid pin out 40
Table 2-2: Waterproof cable pin assignments 43
Table 2-3: Cycloid electric field potentials 47
Table 2-4: Power system wiring harness connector 60
Table 2-5: Current requirements and fuse ratings of electronic circuits 61
Table 2-6: 10 base-T power connector wiring 62
Table 3-1: Embedded computer BIOS settings 75
Table 3-2 Parallel port registers and functions 77
Table 3-3 Command string functional elements and values 85
Table 5-1: Approximate scan input potentials. 118
Table 5-2: Ion fragmentation ratios 125

Equation 2-1: Fundamental thermal noise of feedback resistor 50
Equation 3-1: Mass calibration equation 79
Equation 3-2: Peak-finding algorithm 95
Equation 5-1: Membrane permeability as a function of temperature 127
Equation 5-2: Inlet gas flux as a function of membrane geometry, permeability, and gas concentration. 129
Equation 5-3: Fick's second law of diffusion 133
Equation 5-4: Analyte gas influx 133
Equation 5-5: Membrane response time lag 133

16th century painting of Alexander The Great descending in a glass diving bell

Chapter 1

INTRODUCTION

The aquatic environment is interwoven throughout the history of mankind, serving as a transportation conduit as well as a source of sustenance, religion, wealth, beauty and death. Approximately 37% of the world's population lives within 100 km of an ocean [1], yet humanity's understanding of the hydrosphere has remained extremely limited. At present, our understanding of the dark side of the moon exceeds what is known about the bottom of the Earth's oceans. Like the surface of the moon, the submarine environment is inhospitable to humans, requiring technological devices for exploration, and since ancient times mankind has sought to observe the submarine environment *in-situ*. Writings as early as Aristotle's *Physika Problemata* chronicle the use of submergence systems that, "enable the divers to respire equally well by letting down a cauldron; for this does not fill with water, but retains the air, for it is forced down straight into the water; since, if it inclines at all from an upright position, the water flows in" [2]. Many legends also surround Alexander The Great's use of a diving bell [3], known as the Colimpha, during his siege of Tyre to observe demolition divers removing underwater obstacles from the harbor. The advantages of *in-situ* observation have persisted through modern times, leading to the use of manned submersibles such as the Trieste, Archimede, Alvin, and NR1 for scientific survey of the deep [4]. Although extremely useful, the danger and operational costs associated with these manned submersibles [5] have prompted the development of smaller robotic survey platforms, including buoyed sensors, drifters, remotely operated vehicles (ROVs), and autonomous underwater vehicles (AUVs). AUVs, which are the newest of these technologies, are doubtlessly the most challenging of the unmanned systems to develop because of their reliance on embedded expert systems for navigation control and operations decision-making, but they also appear to hold the greatest promise.

1.1 Autonomous machines

Water clocks, arguably the first autonomous machines, have existed since at least the reign of Amenhotep I in Ancient Egypt, some 3500 years ago. Over the millennia technological advancement has expanded the domain autonomous machines to include the steam engine built by Hero of Alexandria in 100 AD and the mechanical automata of General de Gennes, Jacques de Vaucanson and Henri Maliardet in the 17th through 19th centuries [6], but it was not until the latter half of the 19th century that the fundamental value of closed-loop feedback in control systems was recognized [7]. Shortly thereafter, the advent of long-range weapons systems and telephone switching electronics initiated the rapid development of highly accurate inertial guidance systems for warships and aircraft. By WWII control and guidance systems had advanced to the point of allowing unmanned weapons such as the Vengeance I buzz bomb, an early form of cruise missile, to be used against Britain, a technological accomplishment that cost the lives of thousands of people. Ironically, the M9 gun director and SCR-584 radar system, a then radically advanced type of semi-autonomous anti-aircraft weapon capable of automatic target tracking and firing, was used to fend off the buzz bombs, downing 57% of the missiles that they engaged [7].

During this same wartime period less sinister autonomous systems were under development in England by an American neurological researcher, W. Grey Walter. His creations, a light and impact-sensitive mobile robot named *Machina speculatrix* and a later, more advanced, mobile robot further equipped with memory and sound sensitivity, *Machina docilis,* were used to demonstrate that machines could exhibit traits of spontaneity, autonomy, Pavlovian conditioning, and self-regulation. While studying these machines, Walter identified several emergent behaviors that were sufficiently sophisticated to be described in anthropomorphized terms such as "speculative mode", "learning", "reflex" and "free will" [8, 9]. In the decades since Walter's work a great deal of research has been dedicated to developing autonomous agents which rely on embedded intelligence to operate within complex natural environments in order to fulfill predetermined mission objectives. The resulting multitude of highly specialized systems includes, among others, walking robots such as Genghis [10], space probes such as the

DS1 [11], and autonomous unmanned submersibles including the MIT Odyssey Class AUVs [12].

1.2 Autonomous underwater vehicles

Although AUV use for oceanographic research complements the strengths of manned submersibles and tethered robotic vehicles, the challenges and benefits of AUV operations are fundamentally different from those of existing platforms [13]. As a result, AUV technologies are evolving in a niche where they will serve as a low-cost mechanism for "spatio-temporal sampling; using multiple vehicles in combination for mapping out rapidly evolving phenomen[a]; and transiting long distances to a site for making observations as a part of a first response team at the sight of interest" [14]. Unlike other unmanned platforms such as moorings, tow fish, and remotely operated vehicles, an AUV does not require a tether, thus allowing a spatial survey to be conducted faster, follow bathymetry better and operate in high sea states; translating into increased data collection per unit time or cost, especially when *a priori* knowledge of the survey area is limited. Presently, there are several dozen types of AUVs in operation around the world, ranging in size from the diminutive 37 kg 1.6 meter long REMUS vehicle [15], to the massive 12 meter long ISE Theseus with its one-ton cargo capacity [16]. In recent years several AUV designs have transitioned from the experimental stages into commercially available vehicles, including the Kongsberg Hugin 3000 and the MIT allied Bluefin Odyssey III.

The Odyssey Class AUVs, originally developed at MIT Sea Grant, are relatively small, easily deployable, low component cost survey platforms that have been used in numerous missions throughout the world [13]. These vehicles make use of low-cost, mass produced, hollow glass spheres to house vehicle electronics, sensors and power systems in a dry, one-atmosphere environment. This maximizes buoyancy efficiency and permits the use of a free flooding vehicle fairing, thus minimizing vehicle displacement. However, the minimization of vehicle displacement makes the tradeoff between range (i.e. power storage) and payload capacity a critical design consideration [17].

There is a need for *in-situ* chemical sensors for AUVs. The creation of such sensors presents significant challenges, particularly for smaller vehicles like the Odyssey class

designs. Issues such as size, power consumption, and instrument signal stability have, until recently, excluded the use of highly capable analytical instruments such as mass spectrometers and gas chromatographs on these platforms. Thus, AUV generated chemical data has usually been limited to a select few parameters using ion-sensitive electrodes, mainly: dissolved oxygen, salinity, ORP, pH, nitrate, phosphate and ammonia. However, as Bales and Levine aptly state, "To achieve widespread acceptance within the oceanographic community, AUVs must also deliver, as a minimum, data of comparable quality to that collected today. Sensing and measurement systems designed for deployment from the surface (e.g. on a sampling rosette or tow-body) do not always meet the size and power limits imposed by AUVs" [18]. In general, ion-sensitive electrodes do not meet this stringent standard.

This research focuses on an emerging role of mass spectrometry for submerged, autonomous, *in-situ* operation. Specifically, we detail the development and deployment of the Kemonaut AUV and the NEREUS autonomous submersible mass spectrometer. The Kemonaut is a small, shallow water, AUV capable of operating to depths of 300 meters. It possesses a unique forward payload bay for carrying scientific instrumentation, such as NEREUS. The NEREUS instrument provides a means for rapid and *in-situ* quantification of many gases which have, until now, required offsite analysis. Although NEREUS is designed for operation aboard the Kemonaut AUV (Figure 1-1), it can also be used within a Bluefin Odyssey III AUV as well as a host of other platforms. Operation of the NEREUS instrument onboard an autonomous underwater vehicle enhances the advantages of *in-situ* analysis of dissolved volatile chemicals by increasing the range and overall accessibility of data collection areas.

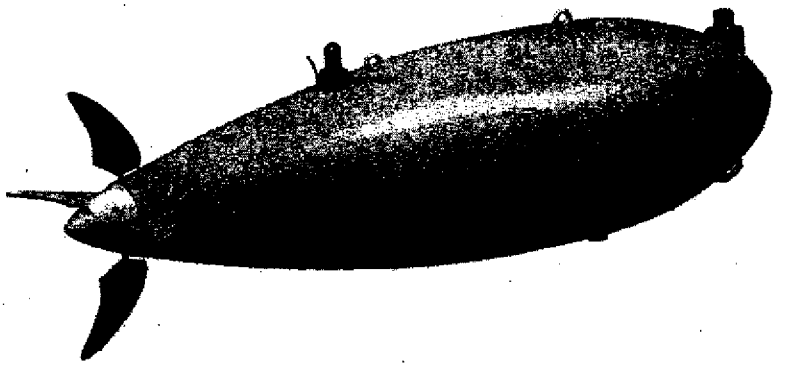

Figure 1-1: Rendering of the Kemonaut AUV

1.3 Mass spectrometry

The principles of mass spectrometric analysis are well understood. Ion repulsion and attraction, a central phenomenon governing mass spectrometry, was observed nearly 150 years ago by J. Plucker in his investigations of magnetically induced light pattern deformations within a glow tube. In 1897 J.J. Thomson demonstrated that cathode rays could be deflected by electrostatic and magnetic fields [19], followed in 1898 by W. Wein's discovery that a type of ray emitted during electrical discharge at low pressure, known at that time as a Goldenstein ray, was actually a positively charged ion beam and could also be deflected by a magnetic field [20]. This phenomenon was later elucidated with Thomson's investigations of the parabolic trajectories of hydrocarbons and other polyatomic ions in his book, *Rays of Positive Electricity and Their Application to Chemical Analyses* [21]; thus establishing that ions could be separated based on their mass to charge ratio when accelerated through a magnetic field. From this work came the mass spectrograph, a predecessor of the mass spectrometer, which relies on a photographic plate to record the presence of ion beams. However, the variable ion sensitivity of this early instrument's photographic plate prohibited precise quantification of ion intensity. For this reason, Thomson modified his parabola mass spectrograph through replacement of the photographic plate with a Faraday cup and electroscope. By varying the magnetic field strength and measuring the resultant ion current, he thereby

created the first mass spectrometer and produced a mass spectrum that quantitatively described the relative abundances of individual gases present in a mixture [22]. The terms mass spectrometer and mass spectrograph would be later coined by F.W. Aston in 1920 [20].

In subsequent years mass spectrometers have evolved to allow for precise mass determinations, measurement of relative ion abundances, and electron impact studies. This has lead to mass spectrometric analysis becoming a standard procedure in a wide range of investigations outside chemistry and physics, including among others, industrial process control, clinical diagnoses, isotope fractionation, radioactive half-life determinations, and environmental monitoring. In 1942 Consolidated Engineering Corporation built the world's first commercially available mass spectrometer for the Atlantic Refining Corporation [20]. As new applications have emerged, specialized instruments have been developed to better suit particular constraints, resulting in highly innovative component variations such as ion source, mass selector, and detector. Technological advancements, particularly in the areas of integrated circuitry and materials science (such as magnetic materials) have permitted the development of more compact mass spectrometers. This, in turn, has enabled mass spectrometers for *in-situ* investigations ranging from terrestrial battlefields [23], to Jupiter's atmosphere [24]. These "field portable" instruments were reduced in size and ruggedized to be transported by spacecraft [25], aircraft [26], and large land vehicles [27, 28] . More recently, a generation of miniaturized mass spectrometers have been developed which are sufficiently compact and lightweight to be carried by a person to a measurement site [23, 29-31].

1.4 Autonomous In-situ mass spectrometry

Mass spectrometers are well suited for autonomous *in-situ* analysis of dissolved gases in a water column, because a mass spectrometer can quickly detect multiple dissolved chemicals at low concentrations, and can work without exhaust or consumable reagents. By implementing automated control and data processing (such as calibration and fragment peak separation) sample components can be quickly identified and quantified in the presence of mixtures. In contrast, conventional environmental chemical analysis

such as gas chromatography or wet chemistry involves collecting and transporting samples to a laboratory for off-site analysis, resulting in sampling and measurement that is generally labor intensive and time-consuming. Additionally, error often arises because of chemical and physical changes occurring to the sample during transport such as degassing and biological or photochemical degradation. Although *in-situ* devices such as dissolved oxygen probes avoid the drawbacks encountered with off-site analysis, they are commonly limited to detecting one or a few gas species [32], with separate sensors required for each specie and sensitivities of typically about 1 ppm. Continuous sampling techniques, such as the Weiss equilibrator, are generally limited to shipboard use with modest sampling depths, and have equilibration times that vary with gas species and range from minutes to hours [33, 34]. The resulting data sparseness often leads to temporal aliasing (translating into spatial aliasing when sampling from a moving platform), which can mask important chemical and biological features in an aquatic environment.

Various approaches have been undertaken to address the design constraints of submersible mass spectrometer operation. Instruments such as the TUHH submersible membrane introduction gas chromatograph – mass spectrometer (GCMS) use a commercially available EM640 field portable GCMS housed within a cylindrical metal pressure vessel [35]. This system, which uses a hollow fiber analyte introduction system, displaces approximately 400 kg and draws several hundred watts, requiring that it function aboard a remotely operated vehicle (ROV) which is powered and controlled via a tether from a surface ship.

Recently AUVs have been developed with reliability, payload carrying capacity, and mission endurance adequate for deployment of a mass spectrometer. Nevertheless, mass spectrometer operation aboard an AUV still introduces several critical instrument payload design constraints, including manditory autonomous operation, small size, and exceptionally low power consumption [14]. Instruments such as the University of South Florida Center for Ocean Technology's (COT) quadrupole and ion trap mass spectrometers [36] utilize off-the-shelf but repackaged Leybold Inficon Transpector and Varian Saturn 2000 analyzers, respectively. Both use a membrane inlet system designed for operation aboard an AUV. The COT quadrupole instrument has been deployed aboard

the 6.4 meter 1.4 ton displacement ARCS AUV [37], but both systems consume power at high rates (in excess of 100 watts), have delicate membrane inlet systems that limit depth of operation to 30 meters and sampling rates no greater than 12 samples per hour for their operating time of a few hours.

The core design concept of the NEREUS membrane inlet mass spectrometer, was to develop an in-situ dissolved gas analyzer that is fast, robust and highly optimized for operation onboard a small autonomous underwater vehicle and various other submerged platforms, including as a self-contained autonomous moored system [38]. To address these and other constraints, the NEREUS system is completely self contained within a 17-inch-diameter glass pressure sphere, compatible with the Odyssey-class AUVs. It weighs 22 kilograms, and is capable of operation to depths of 100 meters (a depth that can be extended with minor modification) on a self contained power supply drawing less than 20 watts, while sampling at rates exceeding 240 samples per hour. The NEREUS system is also unique in that it requires no reagents, has no moving parts, and possesses an autonomous control system capable of adapting its mission directives and sampling regimes to better monitor its environment. Much of the NEREUS prototype draws upon prior research focused on component development [39], which culminated in the construction of vital NEREUS elements such as the vacuum envelope and data acquisition system, and the modeling of system behaviors such as membrane kinetics and vacuum maintenance within the analyzer. A previous generation backpack portable mass spectrometer [29], served as the conceptual model from which the preliminary NEREUS design was based. Drawing from these resources, NEREUS development proceeded with completion of a prototype *(chapter 2)* and bench testing *(chapter 3)*. After bench testing, it was deployed as a stationary "buoyed" type sensor *(chapter 5)*. Upon successful demonstration as a buoyed type sensor, the Kemonaut vehicle was designed and built *(chapter 4)*. NEREUS was then configured for operation onboard the Kemonaut AUV and deployed *(chapter5)*.

	NEREUS	COT Quadrupole	COT Ion Trap	TUHH GC-MS[12]
Power (w)	20	95	150	500
Weight (kg)	21	50	75	65
Size (m^3)	0.014	0.035	~0.6	0.118
Analyzer mass range (AMU)	2-150	2-200	unknown-500	2-640
Maximum sampling rate (/hr)	600	12	12	6
Detection limit (ppb)	1-10	1-10	1-0.1	10-100
Instrument endurance	Weeks	Days	Days	Unknown
Depth rating (m)	100	30	30	300
Vehicle platform	AUV	AUV	Intended for AUV	ROV

Table 1-1: Comparison of submersible mass spectrometer specifications

When used in conjunction with the Kemonaut or Odyssey III vehicles, NEREUS can rapidly generate high-resolution data for mapping temporal and spatial distribution of dissolved gasses on local to basin scales. The relatively light 200 kg displacement and 300 meter depth rating of the Kemonaut vehicle enable routine single day operations, with minimal support equipment (e.g. a small dinghy and transponder array), throughout the entire water column of many freshwater bodies such as inland lakes and rivers, as well as shallow marine coastal areas like Chesapeake Bay and Cape Cod Bay. The larger Odyssey III, which is capable to 6000 meters depth and possesses and endurance of up to 7 days [41] can, with minor modifications, be deployed with the NEREUS system to generate high resolution maps of volatile chemicals, covering a linear distance of over 1,000 kilometers, containing approximately 7,000 high resolution spectra of multiple chemical species. In contrast, current technologies require orders of magnitude longer time frames to generate equivalent data sets.

[1] Does not include submersible inlet apparatus
[2] EM640 specifications from 40. Einfeld, W., et al., *Environmental Technology Verification Report.* 1997, US Environmental Protection Agency, Office of Research and Development: Washington DC. p. 1-78.

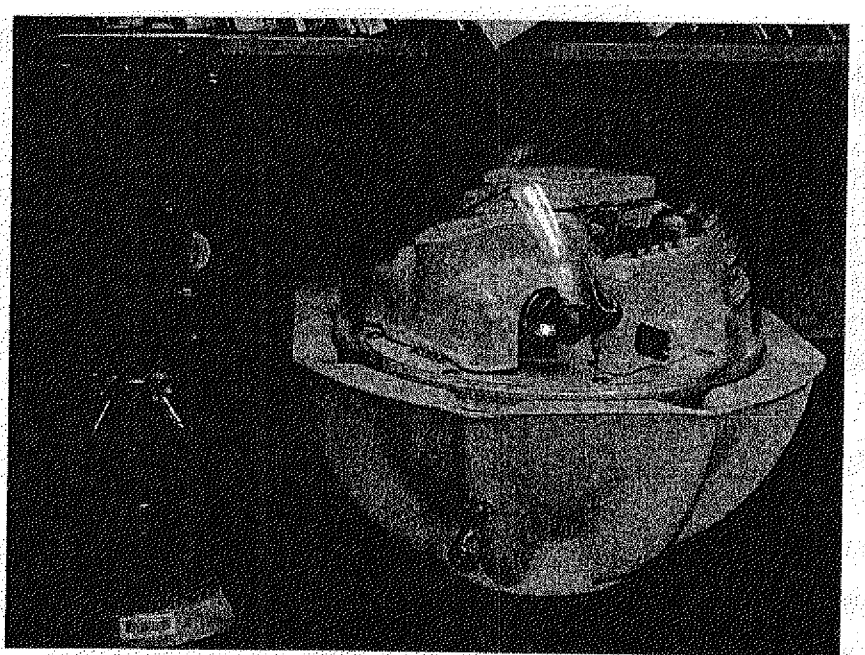

Figure 1-2:NEREUS instrument pictured beside laboratory microscope for size reference

1.5 Applications

Dissolved gases in marine and freshwater environments can vary significantly both spatially and temporally [42-45]. Potential applications for the NEREUS-Kemonaut system are numerous, including geochemical, ecological, hydrological, and chemical fate analyses.

Geochemical applications are wide ranging, including marine mapping of dissolved gases from hydrothermal vents, active volcanic areas and low temperature ocean floor seeps. Investigations are valuable for offshore oil exploration [46] and global climatological research [47, 48]. Methane is often observed in increased concentrations in areas of freshwater inputs [49, 50], anaerobic zones of bottom sediments [51], oil and gas deposits, destruction of crystallohydrates, and emission along fractures in the earth's crust [52].

In-situ mass spectrometric analysis of terrestrial volcanic emissions is used as an indicator of volcanic activity, particularly with regard to Carbon/Sulfur ratios and Helium concentration [53, 54]. Active undersea volcanic areas are also known to emit volatile

chemicals into the water column [55-58]. Thus, analysis of gases dissolved in marine waters may be useful for predicting undersea eruption events. For example, Kick'em Jenny, an undersea volcano just north of the island of Grenada last erupted in December of 2001. Micro-beam survey of the volcano has revealed a massive horseshoe shaped fault scar which most likely resulted from a major slope failure of an earlier cone, suggests that the volcano may be unstable and a future hazard for the region [59]. Survey of dissolved chemicals such as SO_2, CO_2, and He in waters overlaying the cone crater, which lies about 190 meters below the sea surface, may be useful in predicting the activity of the volcano. Advanced warning of impending eruptions are particularly important in volcanic regions such as this to allow adequate time for evacuation of nearby islands to prevent large scale loss of life [60, 61].

Deep-sea hydrothermal vents have also been subjects of increased interest for global climatological and biological research. For example, sources such as anhydrite chimneys of the North Fiji Basin have been shown to emit gases in concentrations exceeding 14.5 parts per thousand of carbon dioxide, 49 ppm of methane, and approximately 937 ppb of helium [62].[3] In some cases, the reduced gases from these vents are known to give rise to entire chemosynthetic ecosystems [63, 64] which oxidize methane or sulfide to produce energy. Detection of gases at these concentrations is possible with the NERUS instrument.

Hydrologic research often utilizes dissolved gas data to determine source and age of waters. NEREUS is a potentially convenient tool for studying mixing of waters in marine and fresh water bodies. Concentrations of oxygen, nitrogen, carbon dioxide, and methane can provide valuable clues as to origins and inflow rates of ground and surface waters into lakes, rivers, and coastal areas [65, 66]. The ability of the NEREUS system to identify and quantify the distribution of these biogenic gases in a water column is also useful for many aspects of ecological research. High spatial and temporal resolution data is valuable for monitoring phenomena such as algal blooms, seasonal stratification & turnover, productivity, and eutrophication [43]. In addition, the NEREUS system could be used to unobtrusively monitor water quality, especially urban runoff, shipping lanes, and point sources of pollution such as sewage outfalls [18].

[3] For consistency, concentrations are expressed as a mass fraction

Mapping of marine oil spills for impact assessment and cleanup is yet another potential NEREUS application. Oil spill surveillance relies almost exclusively on remote sensing such as infrared, ultraviolet, and radar imaging from satellites and planes [67, 68]. These approaches are only suitable for detecting surface slicks, and are unable to detect dissolved petroleum fractions at depth. Oil spill assessment based on surface slick as well as sub-surface data is important when DNAPL or water-soluble fractions are present and when wave induced mixing is a factor. For instance, approximately 77% of the 825,000 gallons of petroleum from the North Cape oil spill was dispersed into the water column [69]. Estimates of this spill's size, based upon oil-slick area, underestimated the magnitude of the disaster, thus contributing to an ill-prepared cleanup response. Although NEREUS would be unable to detect many of the heavier hydrocarbons with low volatility or mass to charge ratios greater than 150, such as poly-aromatic hydrocarbons in an occurrence such as this, NEREUS sensitivity models predict detect limits of many petroleum fractions, including benzene, toluene, butane, and methane in concentrations down to the tens of parts-per-billion level. Furthermore, the petroleum "fingerprinting" may be possible based on the relative distribution of these hydrocarbon constituents [70].

1.6 System performance

Freshwater and marine deployments have been conducted with the NEREUS instrument and the Kemonaut AUV. Tethered and towed operations of the NEREUS instrument have established the ability to map dissolved volatile chemical species in the water column. Sea trials of the Kemonaut AUV demonstrated the unique ability of this Odyssey class AUV to carry the NEREUS instrument as payload. Analysis of vehicle design and performance indicates that the Kemonaut-NEREUS combination is well suited for scientific survey of dissolved gases in freshwater and marine environments to depths of 100 meters. NEREUS data collected during these operations confirm the ability of the instrument to efficiently collect meaningful chemical data in a variety of platform configurations.

Chapter 2

MECHANICAL AND ELECTRONIC HARDWARE

The NEREUS instrument is fully self-contained within a 17" Benthos glass pressure sphere (Figure 2-1). This housing was chosen based on its compatibility with Odyssey class AUVs and its ability to withstand the high compressive loads experienced at abysmal depths. Design and construction of the prototype for operation onboard the AUV, while within the pressure sphere, required careful analysis and optimization. Foremost among design concerns were: instrument miniaturization, response time minimization, chemical sensitivity maximization, power consumption minimization to

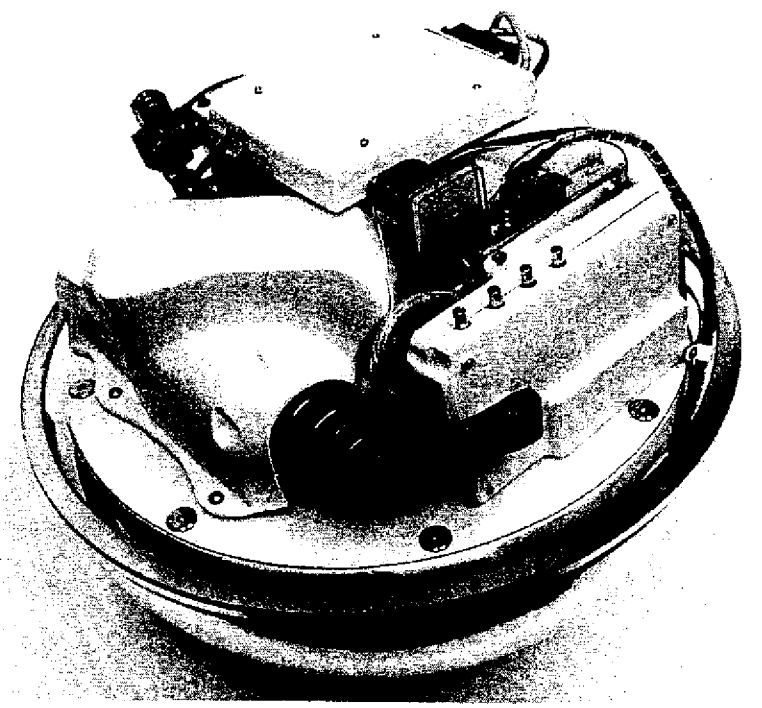

Figure 2-1: The NEREUS instrument with upper glass hemisphere removed

Mapping of marine oil spills for impact assessment and cleanup is yet another potential NEREUS application. Oil spill surveillance relies almost exclusively on remote sensing such as infrared, ultraviolet, and radar imaging from satellites and planes [67, 68]. These approaches are only suitable for detecting surface slicks, and are unable to detect dissolved petroleum fractions at depth. Oil spill assessment based on surface slick as well as sub-surface data is important when DNAPL or water-soluble fractions are present and when wave induced mixing is a factor. For instance, approximately 77% of the 825,000 gallons of petroleum from the North Cape oil spill was dispersed into the water column [69]. Estimates of this spill's size, based upon oil-slick area, underestimated the magnitude of the disaster, thus contributing to an ill-prepared cleanup response. Although NEREUS would be unable to detect many of the heavier hydrocarbons with low volatility or mass to charge ratios greater than 150, such as poly-aromatic hydrocarbons in an occurrence such as this, NEREUS sensitivity models predict detect limits of many petroleum fractions, including benzene, toluene, butane, and methane in concentrations down to the tens of parts-per-billion level. Furthermore, the petroleum "fingerprinting" may be possible based on the relative distribution of these hydrocarbon constituents [70].

1.6 System performance

Freshwater and marine deployments have been conducted with the NEREUS instrument and the Kemonaut AUV. Tethered and towed operations of the NEREUS instrument have established the ability to map dissolved volatile chemical species in the water column. Sea trials of the Kemonaut AUV demonstrated the unique ability of this Odyssey class AUV to carry the NEREUS instrument as payload. Analysis of vehicle design and performance indicates that the Kemonaut-NEREUS combination is well suited for scientific survey of dissolved gases in freshwater and marine environments to depths of 100 meters. NEREUS data collected during these operations confirm the ability of the instrument to efficiently collect meaningful chemical data in a variety of platform configurations.

less than 25 watts, ultra-high vacuum maintenance within the vacuum system, autonomous operation and data interpretation, resistance to vibration, impact, and roll-over. NEREUS can be ostensibly divided into five component groups: vacuum system, analyzer, electronic hardware, software, and mounting apparatus.

2.1 Vacuum system

Two paramount challenges to submerged deployment of marine sensors are to survive the hydrostatic pressures encountered at depth and the corrosive effects of seawater. In addition to those considerations, *in-situ* mass spectrometer design presents the unique requirements of ultra-high vacuum and magnetic field maintenance. Therefore, the vacuum system, which consists of the membrane inlet apparatus, inlet tube, vacuum envelope, and ion pump were fabricated using #304 stainless steel. Although stainless steel is generally more porous to gases than other metals such as aluminum, 304 stainless was chosen for constructing the sample inlet apparatus, sphere penetration, inlet line, and vacuum envelope, based on weldability, low magnetic permeability, chemical inertness, and mechanical strength. Like the pressure sphere, the sample inlet apparatus, which serves as the interface between NEREUS' high vacuum analyzer and its aquatic environment, is required to withstand ambient hydrostatic pressure. In addition to external pressure considerations, the inlet system must also allow for adequate permeation of analyte gases into the vacuum chamber while maintaining an internal vacuum of no greater than 10^{-8} Torr.

2.1.1 Vacuum envelope

The vacuum envelope is roughly the size of the soft drink can (Figure 2-2) and was designed to be small enough to fit within the pressure sphere, yet permit satisfactory conductance of excess gases into the ion pump [39]. Volume minimization also serves to decrease the overall vacuum system's internal volume, thereby minimizing pump down requirements and increasing conductance, thus decreasing the residence time of analyte gases in the region of the cycloid. The cycloid maintains a high vacuum seal with the vacuum envelope by way of eight bolts that firmly compresses a 2.112" diameter PTFE O-ring between the 3 3/8" diameter envelope flange and the cycloid flange.

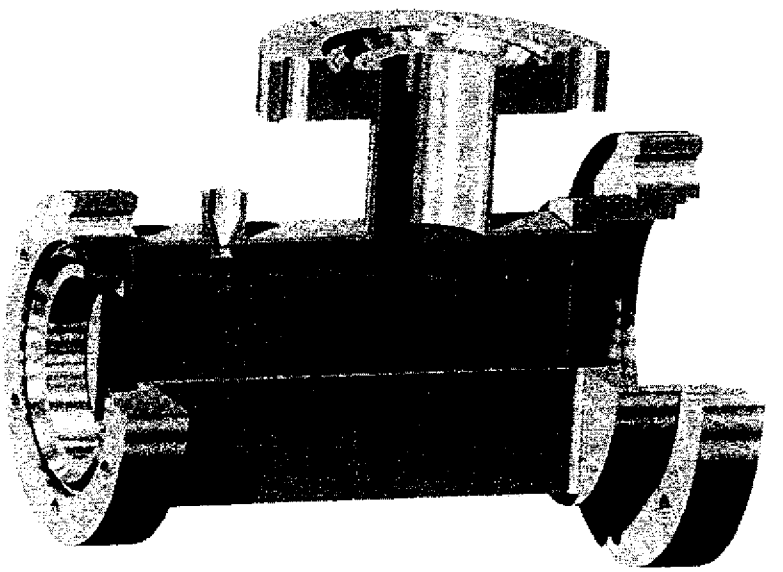

Figure 2-2: Vacuum Envelope cutaway view

2.1.2 Inlet apparatus

Preferential selectivity of dissolved gases over water and water vapor is accomplished by means of a thin semi-permeable membrane that is passively exposed to the water column, thereby allowing analyte gases to diffuse into the vacuum system. The membrane inlet is positioned outside the pressure sphere and connected to the analyzer with a small diameter (approximately 2mm) flexible stainless steel inlet tube. The inlet tube traverses the lower hemisphere through a .6 inch diameter penetration point and 1.5" diameter mounting flat. Although differing in dimension and backing plate material, this inlet design is similar to the membrane inlet described by Hoch and Kok to permit continuous sampling of gases from photosynthetic organisms, that utilizes a thin polyethylene sheet which is held in place over a porous plate by a threaded annular crew

cap and Teflon washer [71]. Whereas, the NEREUS inlet apparatus consists of a 1mil thickness polyethylene membrane placed over a stainless steel micro-etched backing plate and secured by a Teflon washer in series with an annular stainless steel cap that is threaded onto the stainless steel inlet body [72]. Polyethylene is superior to other membrane materials such as PDMS for submerged operation because its relatively low permeability to water [73]. In addition, the small .01" diameter holes of the porous backing plate along with the low compressibility of this material, relative to other polymers, help avoid excessive compression and sagging encountered at depth with other inlet designs (i.e. silicone rubber tubing), thereby minimizing unwanted permeability variation as a function of depth.

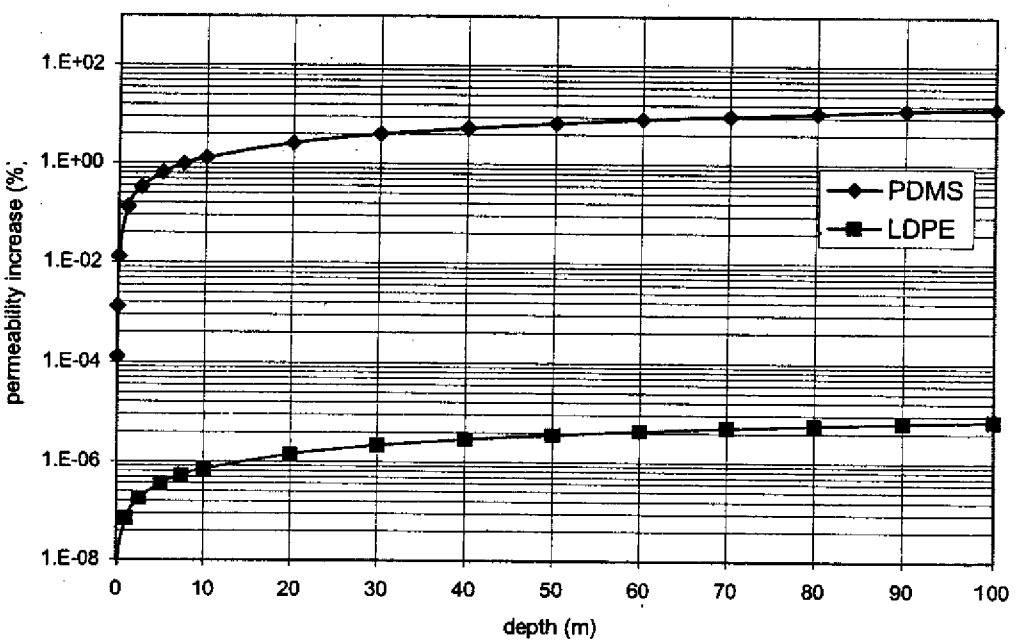

Figure 2-3: Membrane compression and sagging resulting from hydrostatic pressure affecting membrane permeability for the NEREUS inlet system using 0.001" thick LDPE material versus 0.018" thick silicone tubing inlet system. Permeability change calculated using Young's modulus to determine membrane thickness at a given pressure, which is then applied to calculate change in gas flux rate as a function of pressure dependent membrane thickness (refer to Equation 5-4). Values expressed as percent change normalized to value at 0 depth or 1 atmosphere.

The NEREUS membrane inlet threads onto a VCR fitting on the inlet feedthrough, which functions to transport analyte gases to the analyzer residing within the glass

pressure sphere, while preventing water from entering the glass pressure sphere. The feedthrough traverses the lower hemisphere wall using an integrated 1 ½ inch diameter flange with a recessed rubber O-ring that contacts a ground glass flat surrounding a 0.6 inch diameter feed-through hole on the lower hemisphere's external surface, providing a water-tight seal (Figure 2-4). The feedthrough is secured onto the pressure sphere using a rubber washer, to prevent damage to the glass, in series with a 3" stainless steel washer, followed by a stainless steel backing nut.

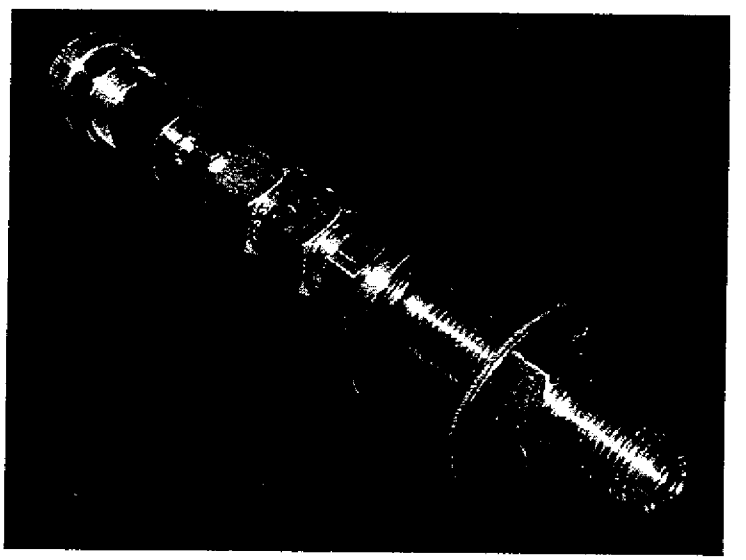

Figure 2-4: Sample inlet apparatus

Portions of inlet tubing residing on the interior of the pressure sphere are constructed of thin walled corrugated tubing because these sections are only required to withstand approximately one atmosphere of pressure, but must be flexible to accommodate partial disassembly of the instrument during maintenance procedures. A flexible corrugated inlet line is connected to the internal junction of the inlet tube penetration to carry sample permeant to a ¼ inch diameter manifold, located at the rear of the instrument. This manifold bifurcates and attaches to two parallel high vacuum bellows valves (model SS-BNV51), linking to separate, bent rigid, lines that terminate at a quick-flange type fitting and at the vacuum envelope inlet. These parallel lines allow, respectively, the vacuum system to be rough pumped down to a point at which the ion pump can begin useful

operation, and the vacuum envelope and ion pump to be sealed off from the inlet during storage. All vacuum system connections use VCR type couplings.

The inlet apparatus is the most likely component to fail under high hydrostatic pressure. This is due to the fact that the inlet membrane resides outside of the pressure sphere and is exposed to ambient water pressure while maintaining a near-perfect vacuum on its internal surface. Possible failure modes include backing plate collapse caused by excessive hydrostatic pressure, membrane rupture caused by excessive hydrostatic pressure, as well as excessive water vapor influx across an intact membrane due to a thermally or chemically induced increase in membrane permeability. In addition to the problems associated with a catastrophic failure of the inlet, significant water vapor input can cause a reduction in signal response through the collision of water molecules with analyte ions. Based on calculations previous calculations [39], inlet membrane and backing plate strength was determined to allow for an absolute maximum deployment depth of approximately 100 meters, with the backing plate being the limiting factor. Destructive pressure testing of the inlet system design has shown the inlet to successfully withstand pressures greater than 100 psi, corresponding to a water depth of approximately 75 meters [72]. To date the NEREUS system has been successfully deployed to a depth of 25 meters.

2.1.3 Ion pump

The vacuum system must first be rough-pumped down to a pressure of no greater than 10^{-5} Torr before the instrument's onboard ion pump can be used to create and maintain free molecular low conditions within the vacuum system [39]. This 8 l/s diode type ion pump is bolted directly to the vacuum envelope at a 2 ½ inch conflat flange fitting located near the center of the vacuum envelope to maximize conductance of excess gas away from the cycloid. The ion pump is powered by a high gain DC-DC converter which accepts the +12 volt input from the battery and generates +3000 volts at its output. When operating at under normal gas loads at steady state conditions, the ion pump typically draw less than 200 μA, or 0.6 watts. The ion pump and power supply, combined, require less than 2 watts of power.

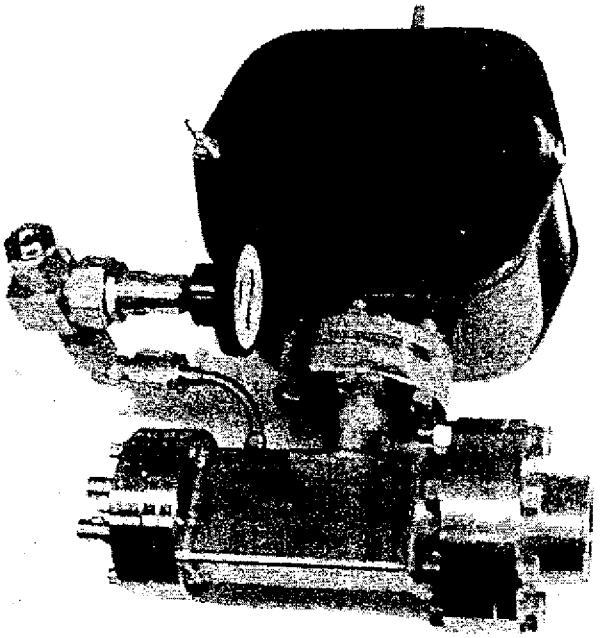

Figure 2-5: Ion pump (with un-machined housing), cycloid and vacuum envelope assembly

Owing to the ion pump's weightiness, the pump housing has been radically machined to help reduce overall instrument weight to a point of neutral buoyancy. This entailed machining away the pump housing's mild steel sidewalls to a total cross sectional area of 2 in^2, thereby still permitting sufficient return path for the ion pump's magnetic flux density of 1,270 Gauss. Additionally, concave lenticular surfaces were machined into the external faces of the pump housing. These surfaces were produced by machining a series of concentric circles of parabolically decreasing depth as a function of distance from the center, intended to accommodate the increasing magnetic flux density developed in relation to distance from the center. The resulting housing weighs 2.8 kg, a 33% reduction from its initial weight of 4.2 kg, yet maintains a flux density of 1,270 Gauss across its interior.

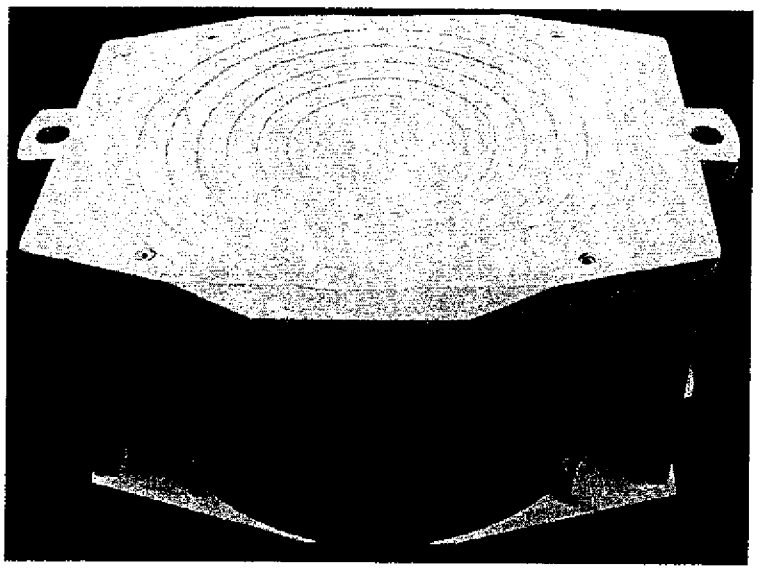

Figure 2-6: Machined ion pump housing

2.2 Analyzer

The analyzer component group, which is mostly contained within the vacuum envelope, includes the ion source, cycloidal mass selector, Faraday cup detector, and elecrometer. A permanent magnet, which is positioned outside of the vacuum envelope provides a homogenous B-field for the cycloid. During operation, sample gases first diffuse from the water column in across the membrane inlet, and then migrate through the inlet tube, toward the vacuum envelope. The limited volume of the inlet system, particularly within the vacuum envelope, has the added advantage of short residence time. Once gas molecules enter the vacuum envelope, they are ionized and then accelerated through the mass selector, finally impacting the Faraday cup detector.

Electric field for the cycloid is produced by a high voltage operational amplifier which supplies a variable potential to accelerator plates within the analyzer. Total instrument power consumption is kept below 20 watts, in part through a high frequency,

duty cycle modulated, emission regulator [38]. To further reduce power consumption, a permanent magnet is used to generate the required B field across the analyzer region.

2.2.1 Analyzer magnet

The analyzer magnet is of an asymmetric U-shaped geometry with an air gap of 1 inch and pole piece diameters of 3.5 inches. The pole pieces and yoke are constructed of low carbon steel to allow for maximum magnetic permeability, while the coercive force of the magnet is generated by two cylindrical NdFeB magnetic members, each residing between a pole pieces and the yoke. Pole pieces are shaped to minimize fringing effects within the air gap region, whereas the yoke is shaped asymmetrically to minimize space requirements and mass. The analyzer magnet of the Hemond backpack instrument served as an initial benchmark for the NEREUS magnet, with a weight goal of less than 11 kg and a flux density of at least 3,500 Gauss for the NEREUS analyzer magnet.

Preliminary magnet designs were prepared using SoldWorks CAD software for shape optimization [39] based on the maximum magnetic permeability (B_{max}) of low carbon steel and a minimum calculated cross sectional area of 3.85 in^2. This type of steel was chosen because of its higher B_{max} relative to standard mild steel. The yoke and pole pieces of the magnet body were then machined from this metal, using a venerable Monarch lathe and Bridgeport end mills at the Parsons Lab machine shop. The magnet's two cylindrical NdFeB elements were constructed by Group Arnold at low cost by virtue of pie shaped magnets that have been compressed and sintered together into a cylinder. These cylindrical magnets are nickel plated to protect the brittle magnetic material from cracking and to minimize exposure to damaging hydrogen gas. Once initial machining and fabrication was complete, four bolt holes were drilled and tapped into the rear of the magnet body to secure the yoke pieces together. Then, using extreme care, the magnetic elements with their pole pieces were positioned on the yoke and are held securely in place using only the magnetic field itself. It is worthwhile noting that serious dangers are posed to fingers and hands by metal objects such as wrenches, which can be caught within the magnet's field and rapidly accelerated to high velocities.

Flux measurements of this initial design revealed a flux density of 4,200 Gauss. To further decrease space requirements and weight, the magnet was carefully disassembled and a subsequent machining of the magnet yoke was undertaken to aggressively trim away areas of low magnetic flux. Areas of reduction were selected presuming curved lines of magnetic flux through the magnetic return circuit and that cross sectional area requirements directly above the magnetic elements range from zero at the distal end of the body, to maximum at the proximal end. Therefore, the external intersections of the magnet body (where the bolts are attached) were rounded using a 1.125 in radius of curvature and a 16° bevel was machined on one of the side surfaces (the surface facing the electrometer and ion pump when fully assembled) and on the surfaces directly above and below the magnetic elements. The resulting magnet weighs approximately 8 kg and generates a flux density of 4,270 Gauss across the air gap, along its central axis.

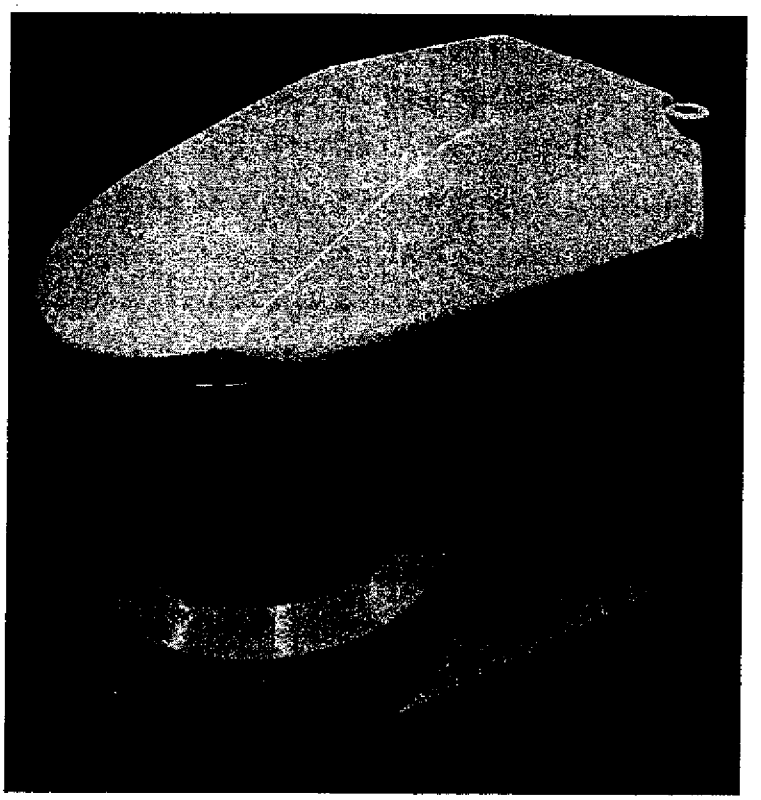

Figure 2-7: Asymmetrically shaped analyzer magnet

2.2.2 Cycloid analyzer

NEREUS employs a modified CEC 21-620 cycloidal type analyzer, as described by Robinson and Hall [74], which uses orthogonally crossed fixed homogenous magnetic and variable homogenous electric fields to impart trochoidal trajectories to sample ions (Figure 2-9). The cycloidal ion trajectory is given by Bleakney and Hipple [75]. This geometry has the inherent property of perfect direction and velocity focusing, making the analyzer less sensitive to misalignment and vibration, and because the ion trajectories loop in on themselves a relatively compact flight path, and therefore size, is achievable. These geometry characteristics allows for a mass range of approximately 2-150 atomic mass units, and a mass resolving power of 100 [20], permitting detection of dissolved biogenic gases, atmospheric gases, light hydrocarbons, and the differentiation of many isotopes.

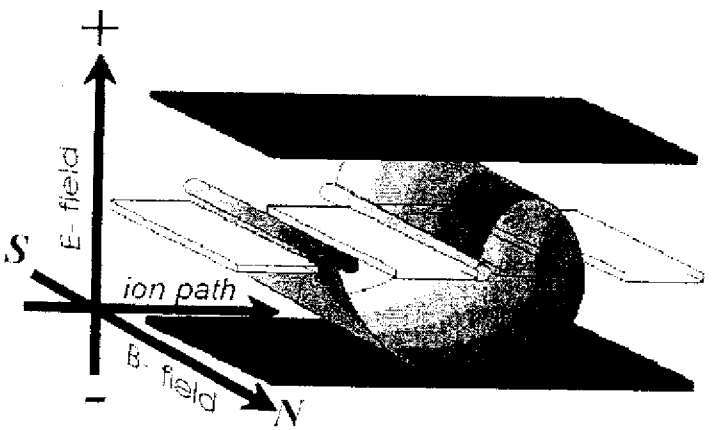

Figure 2-8: Ion trajectory of cycloidal mass analyzer

Modifications to the cycloid include the addition of a cycloid-mounted inlet tube, which directs incoming analyte gases into the ionization chamber, described in detail by Camilli [39]. Also, the cycloid used within the NEREUS prototype lacked an electron trap. To correct this shortcoming, an electron trap was fabricated from a stainless steel double-butted bicycle spoke that was cut and filed into an L-shape with a flattened square tip. This electron trap is held in position by a stainless steel armature, fabricated from a discarded desktop PC motherboard shield, which is bolted to plate 0 and, in turn, bonded

to the electron trap with non-conductive epoxy. In addition, an aluminum shim has been inserted between the cycloid's mounting arch and plate 0, thereby providing an offset to properly align the cycloid within the vacuum envelope. The shim measures 0.865" x 0.105" x 0.275" with two 0.15" diameter holes drilled with a 0.6" spacing to accommodate two cycloid mounting screws. The relatively close tolerances of the cycloid within the vacuum envelope necessitate that the cycloid be aligned to within 1 millimeter of its required position to prevent short-circuiting of the electric field plates to the walls of the vacuum envelope.

Samples are first ionized by the ion source housed within the ionizing chamber portion of the cycloid, located immediately in front of the ion pump inlet. These ions are produced using a heated tungsten filament to thermionically emit electrons that are then accelerated by a 70volt potential, causing these electrons to impact and ionize analyte molecules that have entered the ionization chamber. An electron trap located to the exterior of the ionizing chamber collects free electrons and negatively charged ions. Positively charged ions are then repelled out from the ionizing chamber by a repeller plate (held at a positive potential relative to the ion chamber) and accelerated into the cycloid mass selector by the injector, which carries a positive charge smaller than that of the repeller. Once within the mass selector region of the cycloid, the analyte ions are acted upon by the fixed magnetic field developed by the analyzer magnet and orthogonal electric field created by five electric plates, causing the ions to assume curved trajectories toward one of two Faraday cup detectors. By varying the potential of the electric field in unison with the repeller and injector potentials, ion beams of varying m/z can be made to come into focus on one of the two Faraday cups. Ions with mass-to-charge ratios (m/z) of 12 or less can be made to assume trajectories in the direction of the 180° sector Faraday cup, while ions with m/z of 12 or more can be focused on the cycloidal path Faraday cup. All control signals are sent to the cycloid through its Amphenol type 17 pin connector which is secured to the 3 1/8" flange opening of the vacuum envelope. Connection pins and functions are listed in Table 2-1: Cycloid pin out.

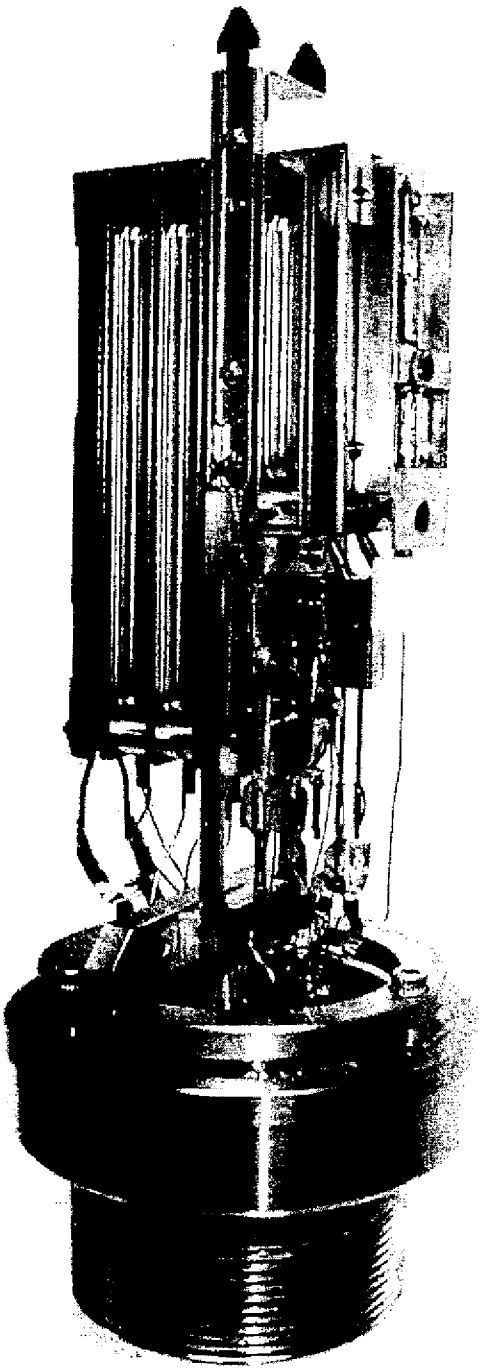

Figure 2-9: NEREUS cycloid tube constructed from a modified CEC 21-620

Cycloid pin	Function	Mass selector pin
A	Filament	
B	Shield/ground	1 & 2
C	Plate heater	
D	Plate heater	
E	Plate 0/ ground	6
F	Electron trap	
G	Plate 2	7
H	Plate heater (omitted)	
J	Plate heater (omitted)	
K	Filament heater	
M	Plate 5	3
N	Plate 1	5
P	Plate 3	4
Q	Injector	9
R	Repeller	10
S	Filament	
T	Plate 4	8

Table 2-1: Cycloid pin out

The ion beams generate an ion current which is detected by the Faraday cup and sent to the electrometer via one of the two BNC type feed-through ports located on the vacuum envelope's 2 ½ inch conflat flange (Figure 2-10). The conflat flange contains two machined recesses that prevent the Faraday cup pickups from contacting the conflat flange and producing a short circuit. Ion current is sent from the Faraday cup pickups to curved music box-like tines that extend perpendicularly from the internal feed through rods. These contacts are constructed from the same lightweight stainless steel material as the electron trap mounting bracket and are tin soldered to the feed through rods. Using these feedthrough contacts, the electrometer senses this ion current and transforms it to an

amplified voltage signal. This electrometer output voltage is then converted to a digital signal by a data acquisition (DAC) board and transmitted to an embedded computer, which interprets and stores this data.

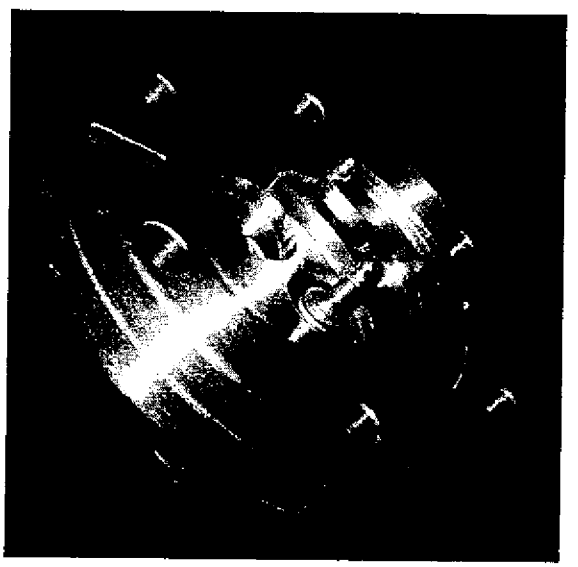

Figure 2-10: Conflat flange with dual BNC feed through

2.3 Electronic Control

Autonomous operation requires that the MIMS instrument be able to perform all necessary functions via a pre-programmed embedded computer system (i.e. a computer system residing within the instrument housing). Minimum functionality includes powering instrument on & off at predetermined intervals, mass step calibration, accelerator potential control, emission regulator control, data collection and handling, and systems diagnostics. To fulfill these operation needs as well as power and space limitations, NEREUS uses embedded PC-104 computer coupled with mass selector controller, data acquisition system, electrometer, and an emission regulator.

2.3.1 Embedded computer

Although higher clock frequency Pentium® type systems offer the highest performance, it comes at an energy use premium. Given the power constraint of approximately 5 watts for the computer and DAQ board, an Ampro 386 SX core module operating at 25MHz was initially utilized in combination with an Ampro VFP-II VGA flat panel controller. The IDE bus of the 386SX module does not permit use of a flashable solid-state (PC card) disk for non-volatile memory storage, therefore, the 1 MB EEPROM was partitioned allowing it to function as a hard drive. After successful short-term deployments, the core module was replaced with a 486DX module operating at 100 MHz; thereby permitting use of a removable solid-state flash disk and thus extending available mission time. In addition to the increased storage space, the faster clock speed and onboard math co-processor of the substituted core module accelerates command line execution, resulting in an increased sampling speed of up to approximately 1500 samples per second while adhering to a power budget of less than 5 watts.

Each data point requires information concerning scan voltage, m/z, and time, imposing a memory requirement of up to a maximum of 248 data bits per sample. To address the data storage needs, NEREUS uses a commercially available 128MB SanDisk Compact Flash disk (commonly used in digital cameras), which has the advantages of extremely small form factor, low power consumption, high tolerance to vibration, impact, and pressure fluctuation, low cost, and modular data transfer from the NEREUS computer to a laptop (i.e. by physically exchanging cards). Presently the embedded computer uses this solid-state disk as a bootable disk, which contains the operating system and instrument code compiled as an executable file. The operating system and instrument code together require approximately 500KB, allowing the remaining 127MB to be reserved for data storage. Because NEREUS employs signal averaging, memory requirements are decreased to less than 2 MB per hour of operation, thus permitting at least 2 ½ days worth of data storage when the instrument is in continuous operation.

2.3.2 Communication

In addition to onboard data storage, the embedded computer is capable of communicating to send data or receive commands from either of two RS232 serial ports

operating either a null modem to AUV control computers or a half handshake protocol to a radio transceiver via a tethered surface float. The radio transceiver receives power from the internal NEREUS power system, with a total power requirement of approximately 150 mW, and operates using a 418 MHz FM frequency with an effective broadcast range of approximately 150 meters when the companion laptop transceiver is within clear line-of-sight and broadcasts to shorter distances when obstructions are present. Communications with either radio transmitter or standard wired serial link require transmission at 9,600 bits per second through a 50 ft. long 9-pin Impulse MIL-9-MP waterproof marine cable pin arrangement is described in Table 2-2.

Impulse cable pin color		Function	DB-9 pin
1	Black	GND	5
2	White	Power	9
3	Red	TXD	3
4	Green	RXD	2
5	Orange	RTS	7
6	Blue	CTS	8
7	Purple	DSR	6
8	Yellow	CD	1
9	Brown	DTR	4

Table 2-2: Waterproof cable pin assignments

2.3.3 Data acquisition and instrument control

The controller/data acquisition system, or DAQ board, is a revised version of the circuit previously described by Camilli [39] , which functions as a compact (12cm x 9 cm), low power (1.5 watt), 16-bit resolution controller and sensor. It is compatible with computers using 8X86 through Pentium® microprocessors, interfacing via a printer port conforming to a PS-2/bi-directional protocol (IEEE1284). The IEEE 1284 standard permits a maximum data width of 8-bits; consequently, the DAQ board makes use of a multiplexor array, which allows for a "two pass" 16-bit transfer of both controller and

sensor data. The DAQ board relies on an Analog Devices 7884 ADC to send commands to the mass selector and an Analog Devices 569 DAC to quantify electrometer voltage; both converters possess sample-and-hold capabilities, permitting simultaneous operation of the sensor and controller.

This generation DAQ design incorporates several improvements over the previous generation described by Camilli [39]. Included is an optional –5V input offset circuit for electrometer input (jumper selected), thereby enabling use of the full –5V to +5V scale of the AD7884 analog-to-digital converter. Additionally, all 5 status register bits of the parallel port have been made available for possible use as indicators of instrument states such as excessive internal pressure, ion pump failure, fail-safe activation, and low battery condition. Bit 3 of the control line operates a relay controlling the emission regulator's on/off state, thus permitting a computer selectable low power sleep mode. Additionally, digital-to-analog output is now routed to an on-board isolation operational amplifier, which uses the scan board's "floating" power supply to generate scan board input voltages. Finally, the new DAQ design makes use of Analog Devices' BQ and AN line of integrated circuits, which offer improved noise characteristics over AQ models.

Error correction algorithms have been incorporated into the DAQ board execution code to increase accuracy. The controller correction is simply a computed 4mV offset, while the sensor correction is a slope-offset algorithm designed to accommodate a 2's complement architecture. To further decrease sampling error, a signal-averaging regime has been included into the sensor code. Previous DAQ board performance testing demonstrated capabilities of sense and control functions with sample speed independent 16-bit accuracy, and operational speed dependent on the command line execution rate of its host computer [39].

2.3.4 Mass Selector

Electrical potential is delivered to the repeller, injector, and accelerator plates by an isolated high-gain circuit. This circuit is adapted from the Hemond scan board [29]; a design that is, in turn, based on a CEC controller developed in the early 1950s [74] which relies upon vacuum tubes common to that era.

The NEREUS scan control input voltage, generated by the embedded computer and DAQ, is relayed via an onboard BurrBrown model 124 isolation operational amplifier. The output of the iso opamp is routed to the negative input of a heat-sinked operational amplifier (Apex model PA88) acting as an inverting amplifier. This high voltage opamp provides a gain of approximately –60 X relative to the input scan control voltage. It is necessary to isolate this high voltage circuit so that the repeller, injector, and accelerator plates can make use of a "floating" ground reference, thereby allowing accelerator plates #1, #3, and #5 (focus) to develop substantially negative potentials without requiring a dedicated negative power supply.

The operational amplifier makes use of a "floating ground" power supply created by a ±15 volt DC-DC converter (PICO model 12GR150), with the +15 volt output transformed into +300 volts by a second set of three serially connected 100 volt DC-DC converters (PICO model 12A100). The +300 volt output is then routed through a 1000 ohm resistor to limit current. A 10μF accumulator capacitor is shunted to the common terminal of the circuit to stabilize the 300 volt output, while two 150 volt zener diodes in series protect the circuit from reverse polarity damage. Finally, the +300 volt and –15 volt supplies are routed to the supply pins of the PA88.

The output of the PA88 is connected to a resistor ladder, which acts as a voltage divider for the accelerator plates. These plates are arranged so that the even numbered plates (2 and 4) develop respectively increasing positive potential, and the odd lumbered plates (1,3, and 5) develop increasing negative potential, respectively. Plate 0, which also serves as the cycloid mounting spar is held at ground potential relative to the negative electrode of the battery pack and vacuum envelope. Resistor ladder arrangement is detailed in Figure 2-11.

The scan board was initially unable to generate the requisite plate voltages for focusing ions with m/z less than 17. Major revisions to a second resistor ladder operating in parallel with the accelerator plate ladder to source voltage to the injector and repeller plates, were made to reduce the overall current demand placed on the PA88 opamp and 100 volt DC-DC converters. It is likely that this scanning limit is a result of increased plate voltage needed to match the 20% increase in field strength of the scan magnet over previous magnet designs. To accomplish current reduction and thereby enable higher

plate voltages without requiring increased power, variable voltage to the injector and repeller plates is provided by way of two parallel 100K Ω 1 watt potentiometers connected to the PA88 output and shunted to the common terminal via a 100K Ω resistor tail. Through this modification the overall resistance of the circuit was increased from 45.8K Ω to 55K Ω, resulting in a 20% decrease in power demand and thereby extending the scan range to m/z of less than 12. After completing these modifications, accelerator plate voltages were tuned to maximize ion peak height while maintaining baseline linearity. Greatest performance was achieved by tuning the potentiometers to produce the voltages described in Table 2-3, where all potentials are referenced to the vacuum envelope, and a voltage of -1.174 volts is applied at the input of the scan controller.

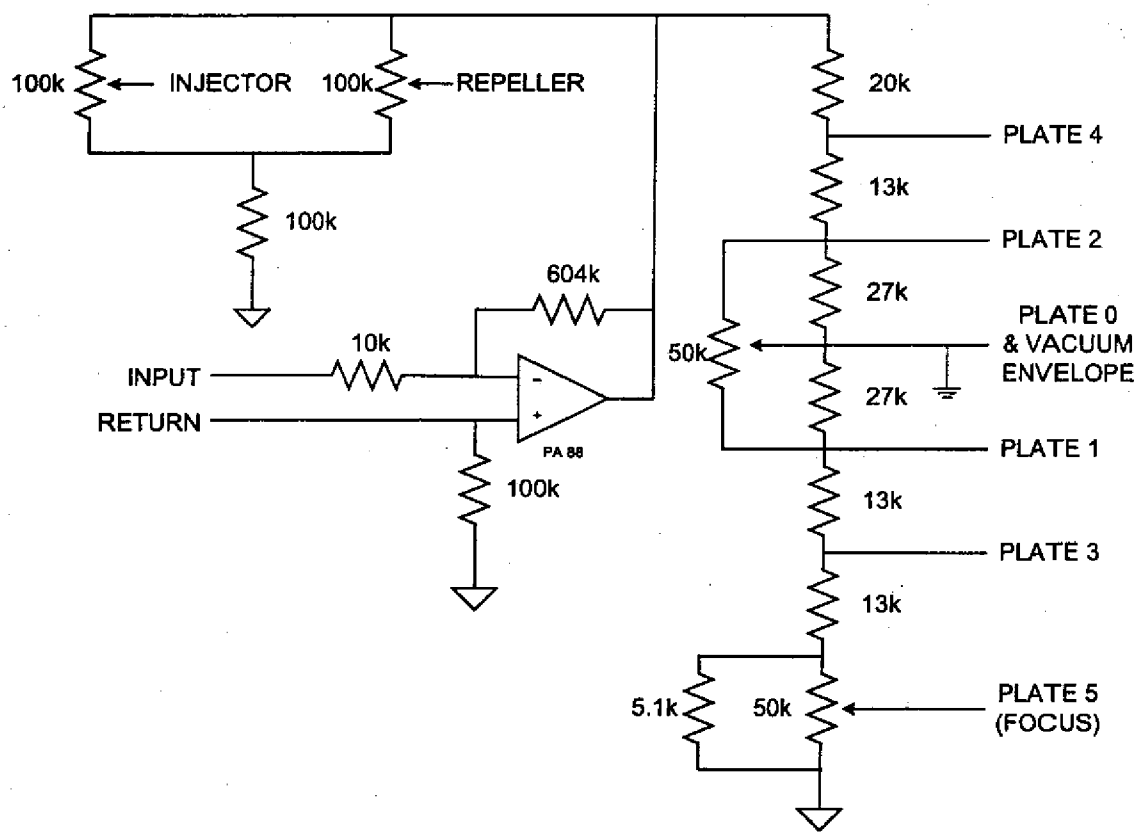

Figure 2-11: Scan controller detail

Cycloid E-field	Cycloid pin	Edge connect pin	Potential (volts)
Repeller	R	10	34.5
Injector	Q	9	24.36
Plate 0	E	6	0.0
Plate 1	N	5	-11.16
Plate 2	G	7	11.20
Plate 3	P	4	-22.12
Plate 4	T	8	22.09
Plate 5	M	3	-36.02

Table 2-3: Cycloid electric field potentials

2.3.5 Emission regulator

Ionization of sample analyte is accomplished by means of electron impact, wherein electricity is supplied to the filament from an electronic circuit, causing electrons to be ejected from the heated tungsten filament. This process accounts for the majority of the instrument's power consumption; therefore, to improve energy efficiency over that of a simple resistive element regulator, the NEREUS ionization circuit, developed by Hemond [38], relies upon a TL494 integrated circuit, operating as a square wave generator to drive two field effect power transistors, which are connected in a push pull arrangement. The current driven through these transistors is then rectified and sent to a DC-DC converter, where its voltage is decreased from 12 to approximately 2 volts and current increased to approximately 3 Amperes before acting upon the filament. By varying the duty cycle of this square wave instead of circuit resistance, losses are minimized. Regulation of the square wave duty cycle is maintained through a negative feedback loop that senses electron trap current and adjusts the duty cycle to match potentiometer specified current.

Electric current is delivered to the filament via two 12 gauge wires which are affixed to square pads on the circuit board. Typically, the emission regulator draws 9 watts of power while operating at 8 kHz. A Simpson micro ammeter that electrically connects the electron trap to the emission regulator's sensory circuitry, and is physically

mounted directly above the emission regulator, can be used to visually monitor trap current developed by the ionization chamber. Trap current is typically around 7 μA during instrument operation. Power and sensory lines (including trap current and on/off control logic) are input to the emission regulator trough a DB-25 connector. Size of the emission regulator was reduced to a NEREUS compatible footprint through the use of miniaturized components such as DC-DC converters and ceramic capacitors and the circuit being etched onto a double-sided board measuring 3.5" x 3.5". Care was taken in circuit board layout to place high noise components such as switching power transistors and converters into areas away from sensory components and to minimize trace lengths.

The emission regulator is switched on and off via software, using the computer's parallel port control bit-3 line to direct a bipolar transistor which drives a reed type relay switch connecting the TL494 on/off line to ground. In this way, the computer can turn off the emission regulator during periods of inactivity, decreasing power consumption from approximately 18 to 9 watts. This control circuit is integral to the DAQ circuitry and, due to its position above the ion pump housing and analyzer magnet, requires B-field shielding for satisfactory relay actuation.

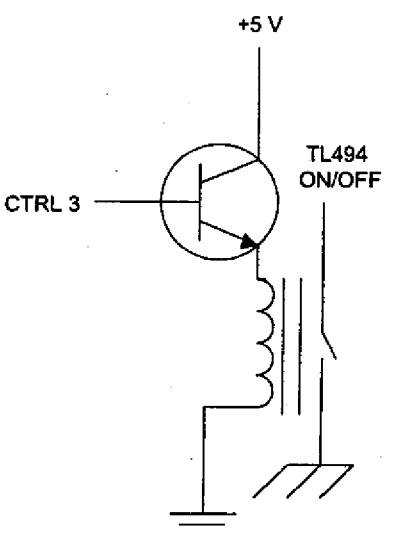

Figure 2-12: Software controlled emission regulator on/off relay

2.3.6 Electrometer

The extremely low ion currents generated by the Faraday cup requires that the electrometer produce a large gain while keeping noise at minimal levels. Given the 16 bit resolution and –5 to +5 volt input signal range of the DAQ's analog to digital converter, the electrometer should be able to amplify the smallest ion current of interest to at least 153 μ volts. However, the need for high gain requires the use of a feedback resistor valued greater than 10^9 ohms, which dominates all other electrometer voltage noise sources. Additionally, the response time of the electrometer is determined by the resistor-capacitor time constant of the feedback resistor and the stray capacitance across the resistor. This time constant determines the maximum bandwidth of the electrometer and, consequently, can be the limiting factor for overall instrument sampling speed (i.e. when multiple mass peaks are required in a spectral scan). Therefore, adequate instrument performance requires an optimization of the electrometer's amplification, noise tolerance, and bandwidth parameters.

Initially, an electrometer previously developed for the Hemond mass spectrometer (Hemond 1991) was tested for use on the NEREUS system. This circuit uses a circuit based on a Teledyne 1702 operational amplifier connected as a current-to-voltage converter, followed by a unity gain inverting buffer (Figure 2-13). The 1702 op-amp generates an extremely low bias current, which is achieved with a parametric input stage. The low noise characteristics of this electrometer permit quantization of ion current signals as small as 10^{-14} amps. However a $10^{11}\Omega$ feedback resistor and 2pF of capacitance, yield a response time of approximately one half second, making electrometer time response a major limiting factor because successive scans across the spectral range are required. For example, if 1,000 mass steps (including molecular ions and fragments) are needed to accurately represent mass peaks across a single spectrum, and measurement of ion current at each mass step requires 0.5 second, the time needed to complete the scan exceeds 8 minutes. Therefore, a new electrometer was developed that possesses the same low noise characteristics as the Hemond design, while increasing its effective bandwidth.

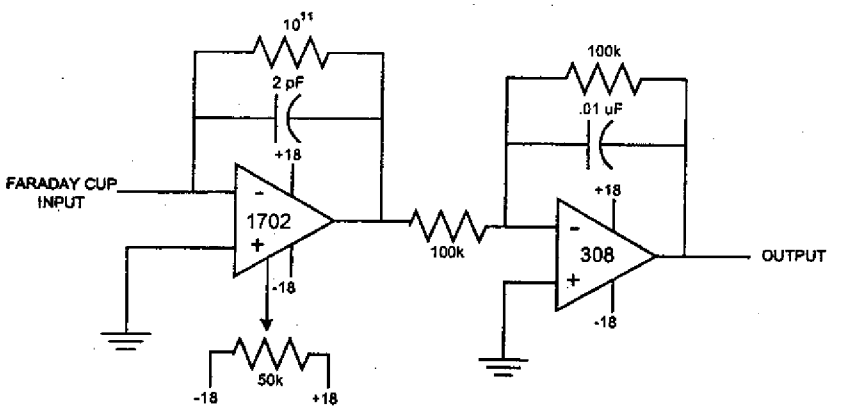

Figure 2-13: Teledyne parametric op-amp electrometer design by Hemond

For design purposes, minimum required signal amplification can be calculated assuming a 153 μvolt minimum DAQ detectable voltage (10 volts of dynamic range/16 bits). Given an assumed minimum detectable ion current of 10^{-14} amperes, overall electrometer gain must be at least 1.53×10^{10} (where 1 ampere = 1 volt/ampere). Based on this gain value, an appropriate feedback resistor can be calculated. Feedback resistor selection is limited because large value resistors are produced in only limited sizes. Presuming that the Johnson noise of the feedback resistor will be the dominant noise source, a noise value for the feedback resistor can be easily computed as a function of temperature (the NEREUS instrument package is not intended to operate in water bodies that exceed 300°K) and frequency; where i is current in amps, K is the Boltzmann constant of 1.38×10^{-23} Joules/ Kelvin, T is temperature in Kelvin, B is bandwidth in Hertz, and R is resistance in ohms.

$$e^2 = 4KTBR$$

Equation 2-1: Fundamental thermal noise of feedback resistor

Using Ohm's law to compute the output signal voltage for a given resistive value, the output signal (given a 10^{-14} Ampere input) can then be compared against its output thermal noise voltage to find a signal-to-noise ratio. For example, a 10^{10} Ω resistor produces a voltage signal of 100 μV, but generates Johnson noise of equal value (S/N=1)

when bandwidth is 60.4 Hz and temperature is 300 Kelvin; while a stray capacitance of 1pF in parallel with 10^{10} Ω yields a time constant of 100Hz. In this case the circuit would be frequency limited by the Johnson noise. Assuming that a signal-to-noise ratio of at least 1 is required for detection of the ion current, a maximum temperature of 300 Kelvin, a minimum ion current of 10^{-14} Amperes, and a stray capacitance of at least 2pF exists in parallel with the feedback resistor, a feedback resistor value with optimum signal-to-noise and frequency characteristics can be found. Figure 2-14 graphically illustrates how circuits with feedback resistor values of less than approximately 5 x10^9 are frequency limited by Johnson noise and circuits with feedback resistors greater than 1.5 x10^{10} and capacitance of at least 2 pF are frequency limited by their RC time constant.

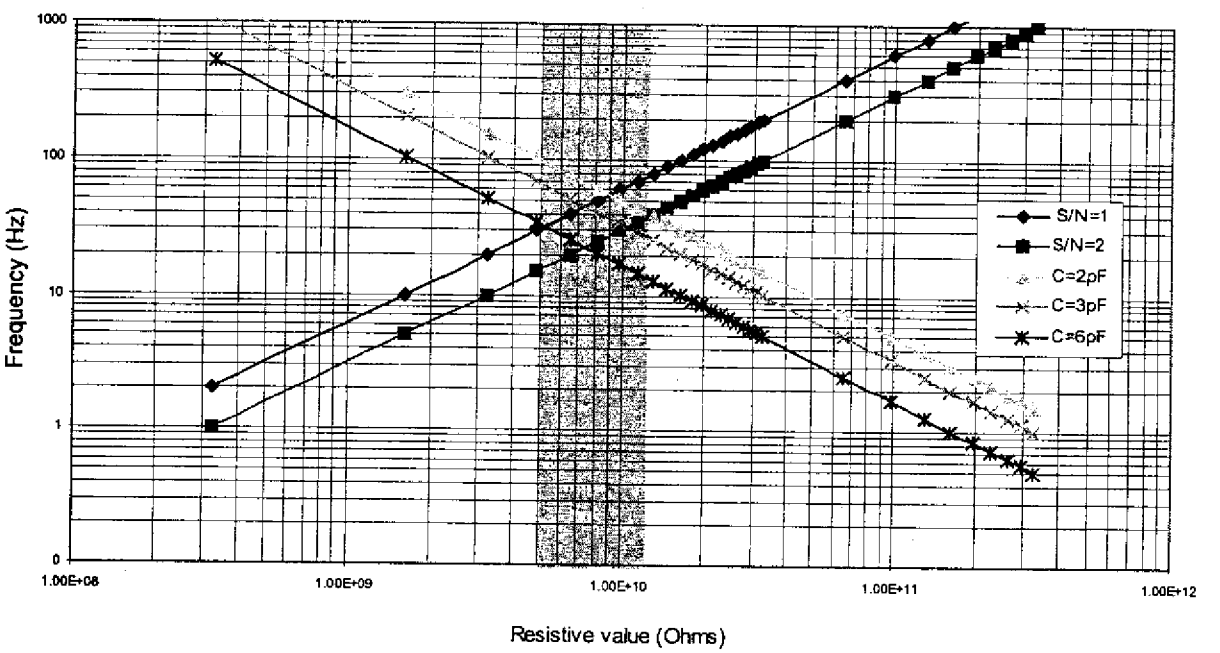

Figure 2-14: Optimal feedback resistor value as a function of RC time constant and S/N, assuming a minimum input signal of 10^{-14} Amperes, temperature of 300K, and Johnson noise dominating.

Having identified a feedback resistor of approximately 10^{10} Ω as optimal, a glass type 1.05 x10^{10} Ω Victoreen resistor was chosen, based on cost and availability. Then, using these calculations, the active components of the electrometer were selected. Beginning with the electrometer input, a National Semiconductor LMC6001 field effect operational amplifier was chosen for use as the first stage gain. The LMC 6001 was selected because of its low input current noise characteristics (0.13fA/$Hz^{1/2}$), and because its field-effect architecture minimizes input leakage. Like the previous electrometer design, the LMC6001 is arranged as an inverting amplifier, with its negative input connected to the Faraday cup lead. This arrangement amplifies the 10^{-14} amperes to –105 μV at the output of the LMC6001.

Previous calculations and experimentation [39] indicated that the NEREUS instrument requires a dynamic range of approximately 2000 to properly quantify dissolved chemicals of interest at common ambient environmental concentrations (i.e. from 10 parts per billion to 20 parts per million). Therefore, to provide adequate amplification to make full use of the 10 volt digital-to-analog converter range, the output of the LMC6001 is connected to the input of a second stage amplifier which amplifies the input with a gain of -50. This second stage employs a Linear Technology LTC1151 operational amplifier (configured as an inverting amplifier) that can convert and amplify a 200mV input to a 10 volt output. The LMC6001 advertises zero drift and an input offset of 5μV, minimizing baseline clipping and drift. Finally, the output is routed through a resistor capacitor series low pass filter with its –3dB roll-off centered at 150 Hz. The 150Hz value was chosen so that signal attenuation would be minimized in the frequency region of interest (≤50 Hz). A schematic of the circuit is shown in Figure 2-15.

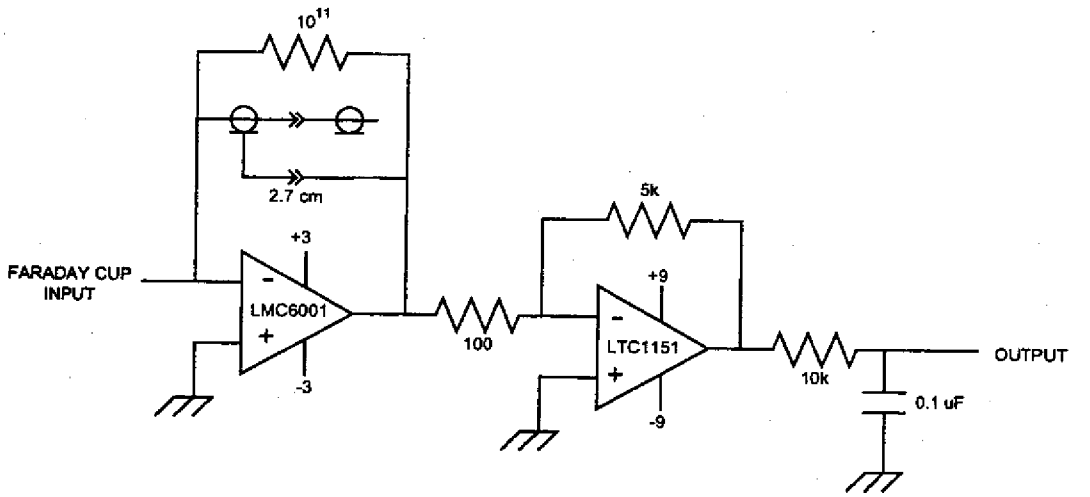

Figure 2-15: NEREUS electrometer circuit

An overall expected noise budget as a function of bandwidth was determined for the electrometer, using the noise figures for the feedback resistor, the various other resistors, and for the active components which are listed in the data sheets of the LMC6001 and LTC1151. Based on this noise budget, a minimum ion detectable current as a function of bandwidth can be calculated, assuming S/N=1 and T= 300°K (Figure 2-16).

To minimize size, the circuit was constructed on an etched single plane PC-board, using 1/8 watt resistors, DIP packages for the LTC1151 the LMC6001 (Figure 2-17). The Victoreen feedback resistor was connected to the input of the LMC6001 using an "air wiring" technique. This approach takes advantages of the insulative and low stray capacitive properties of air to minimize the effects of stray electronic noise, which although small, still permeates the etched board material.

A battery power supply consisting of two 9 volt alkaline batteries in series with a center tap, providing ±9 volts, in parallel with four center tapped 1.5 volt AA alkaline batteries providing ±3 volts to the LMC6001 supplies to the op-amps and voltage reference.

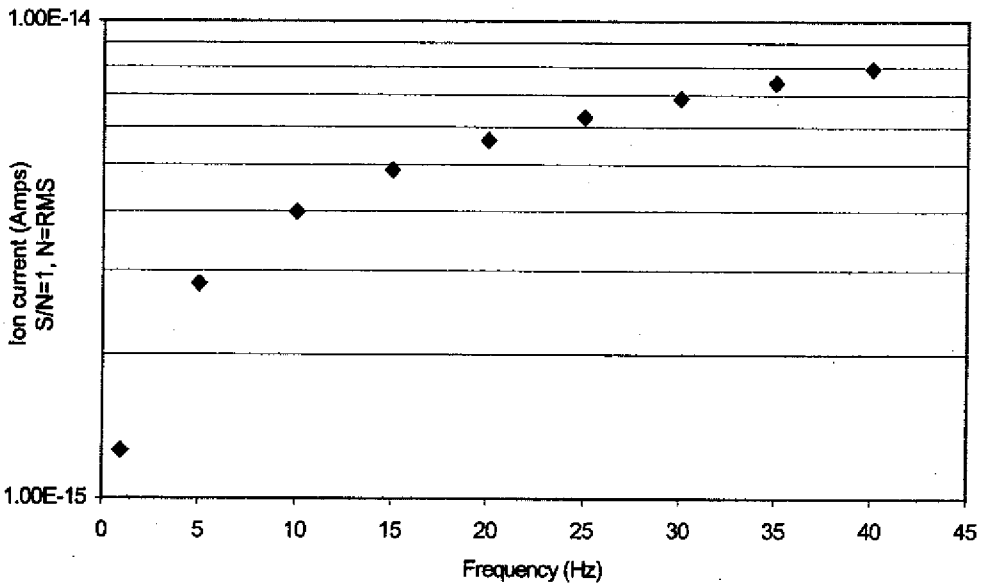

Figure 2-16: Theoretical electrometer sensitivity vs. sampling frequency (assuming circuit is not limited by feedback resistor RC time constant)

To match the –5 to +5 range of the DAQ, the 0 to 10 volt output of, the LTC1151 output was offset using an Analog Devices REF195 +5 [change] volt precision voltage reference that is connected to the output of the LTC1151 via second LTC1151 operating as a unity gain inverter. This voltage regulator addition, however, generated electronic interference in excess of the resolution gain attained by centering the output range about zero. Therefore, this offset circuit was re-designed using a high precision AD588BQ voltage reference that resides on the DAQ board, thus preventing voltage reference induced load fluctuations from significantly decreasing the electrometer's signal to noise ratio.

A 3.7 cm length of coaxial cable is used in parallel with the Victoreen resistor as a low value (~ 3 pF) capacitor. This length of cable is necessary to provide feedback

amplifier frequency compensation, thereby avoiding stability problems resulting in a rail-to-rail oscillation at 26Hz (higher harmonics also) on the electrometer's output. Through trial and error, a minimum capacitive value was found that prevented the oscillation. The exact cause of this instability is still unclear, but is most likely due to the extremely high gain of the Victoreen resistor in combination with stray effects near the LMC6001 leads. The resulting overall gain and response time of the electrometer suggest that the coaxial capacitor may also function as a resistive element to the extent that it decreases the feedback effective resitance (possibly a factor of 5 or more).

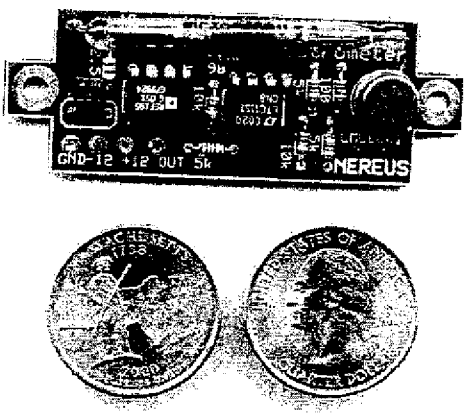

Figure 2-17: NEREUS electrometer

In addition to careful circuit design, several other steps were taken to minimize the effects of external noise sources. A battery pack, sourcing ±3 and ±9 volts to the electrometer was built to minimize 60Hz interference, which was encountered even when using high-quality regulated AC power supplies. A second line of defense against external noise was to place the electrometer in a Faraday cage and position it as close to the Faraday cup as possible. To accomplish this, the electrometer was mounted inside a small rectangular aluminum BUD box, and positioned so that the vacuum envelope feed-through actually penetrates the aluminum box, allowing the Faraday cup output to connect directly to the input of the electrometer's LMC6001 op-amp. Finally, the vacuum

envelope and electrometer box were connected to the battery pack's common lead, to make the electrometer resistant to damage from electrostatic discharge (Figure 2-18).

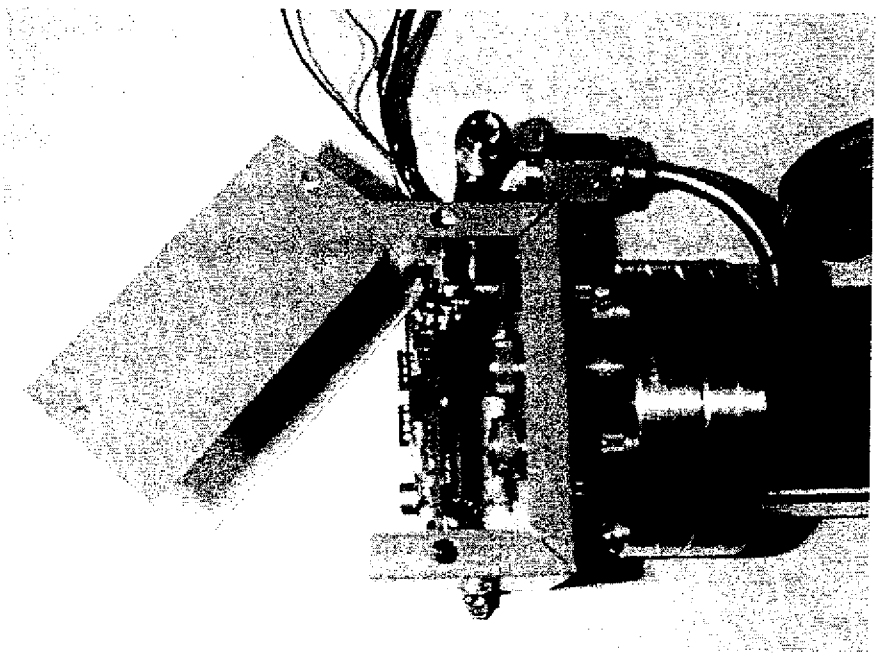

Figure 2-18: Electrometer shielding and mounting

A Hewlett Packard digital storage oscilloscope was used to collect data to analyze the response characteristics of this electrometer design. Analysis consisted of sampling a time series of approximately 32 seconds duration, at 1,000 samples per second, resulting in a 32,768 point data series. These data series were then saved to disk and converted to Matlab readable data files. The time series data sets then were transformed into frequency spectra. Once the frequency spectrum was obtained, this data was then analyzed for power spectral density. Based on time series data taken with the scope probe shorted to ground, the probe introduces approximately $1.19mV_{rms}$ of error to the measurement. To estimate the noise inherent to the electrometer circuit, its input was tied to ground. Two separate time series taken with the input grounded, indicated that the electrometer generates from $3.42mV_{rms}$ to $8.36mV_{rms}$ of noise. No significant correlation is evident between scope probe noise and electrometer noise. However, the electrometer appears to be particularly sensitive to low frequency mechanical vibrations. Initial spectral analysis

of the electrometer with its input connected to the Faraday cup revealed the 26Hz rail-to-rail oscillation (as well as higher harmonics). After the oscillatory response was attenuated with a properly trimmed coaxial cable (acting as a capacitive compensator), the electrometer in combination with the Faraday cup generated approximately $9.13mV_{rms}$ of noise (Figure 2-19). Based on cross correlation analysis, the oscillation problem appears to either have been eliminated, or its magnitude attenuated to somewhere below the noise floor of the electrometer (Figure 2-20). Close inspection of the power spectral analysis for the compensated electrometer reveals a 60Hz peak with a magnitude approximately an order of magnitude above baseline. This peak is likely to have been caused by external power lines and fluorescent lights in the laboratory room where the measurements were made. Other higher frequency peaks, between 400 and 500 Hz, are well in excess of the critical threshold of the output's low-pass filter, suggesting that these frequencies are likely to have been generated and/or experienced subsequent to the electrometer output.

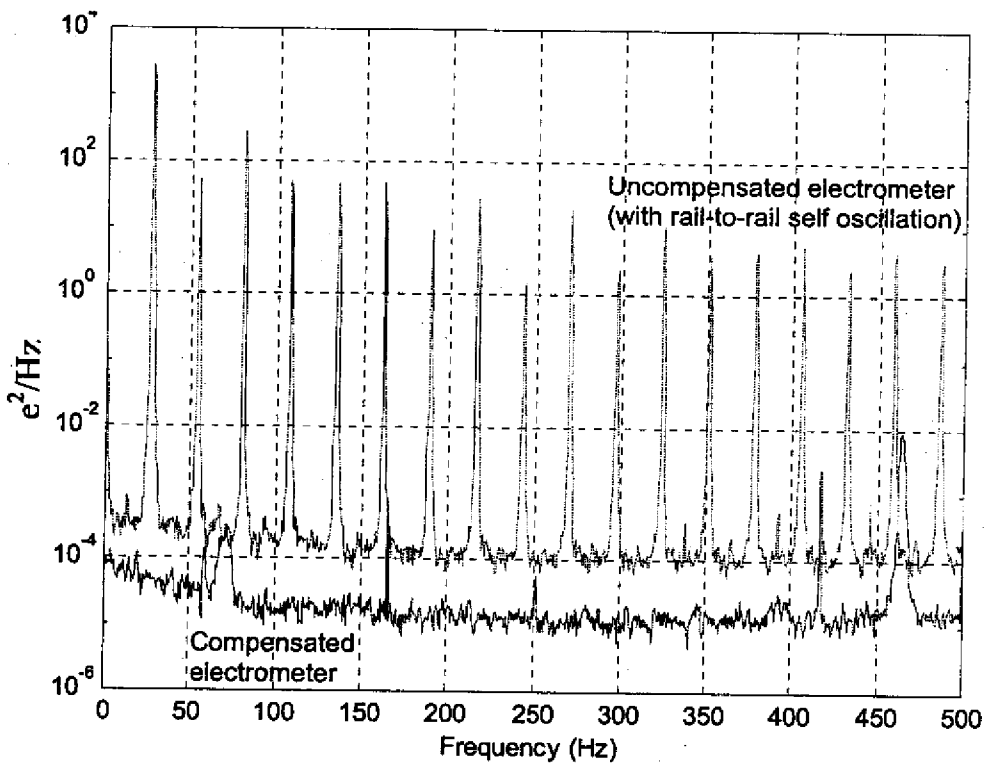

Figure 2-19: Power spectral density of electrometer with and without coaxial capacitive compensator

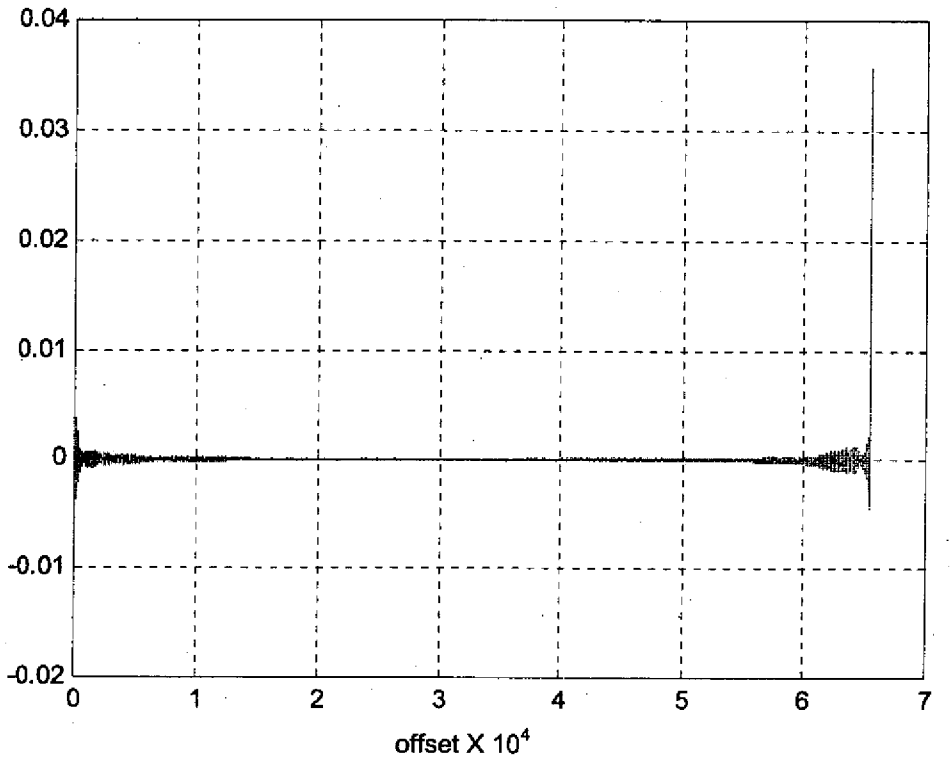

Figure 2-20: Time series cross correlation of electrometer noise data with and without capacitive compensation

The 9.13mV of measured electrometer noise is roughly twice the estimated value, thus elevating the minimum detectable ion current to 1.75 $x10^{-14}$ amps. Although a minimum detection limit of 2 $x10^{-14}$ amps and maximum sampling frequency of 25Hz (assuming 4pF of capacitance) is acceptable, post-processing techniques may allow further improvement. Detailed examination of the frequency spectra of the electrometer indicates that the noise measured at the output of the electrometer is generally "white", or distributed uniformly across the frequency spectrum. The randomness of this noise is exploited by employing signal averaging to reduce the magnitude of noise without attenuating the signal; thereby increasing the signal-to-noise ratio. Applying this technique to the electrometer data collected by the oscilloscope, we see a 90% error reduction when using 100X signal averaging, an 86% error reduction with 50X signal averaging, an 82% error reduction with 25X signal averaging, and a 59% error reduction with 5X signal averaging. These values appear to behave very nearly to that of $n^{1/2}/n$

statistics, corroborating the hypothesis of noise randomness. If a 10X signal averaging routine were to be implemented, a 68% noise reduction could be expected. The analog-to-digital converter of the DAQ system is capable of conversion rates in excess of 150,000 samples per second, allowing for many samples in quick succession. Consequently, if the electrometer bandwidth is 25 Hz, the DAQ can be made to do successive conversions, with a 1ms temporal spacing, after an initial time delay of 25ms (to allow electrometer output settling). This would have an overall effect of decreasing the bandwidth to less than 25Hz, but increasing the ion current sensitivity.

In comparison to the Teledyne electrometer, the NEREUS electrometer appears to be less affected by electromagnetic disturbances below 60 Hz (Figure 2-21). Given that the NEREUS electrometer is designed to be used only within a frequency band up to approximately 25 Hz, and incorporates a post-amplification low pass filter intended to attenuate frequencies above 50Hz, this electrometer in fact possesses lower noise characteristics than the Hemond design, yet requires a shorter response time. These performance advantages are most likely due to the two-stage amplification process and the extremely low bias current of the 6001 op-amp.

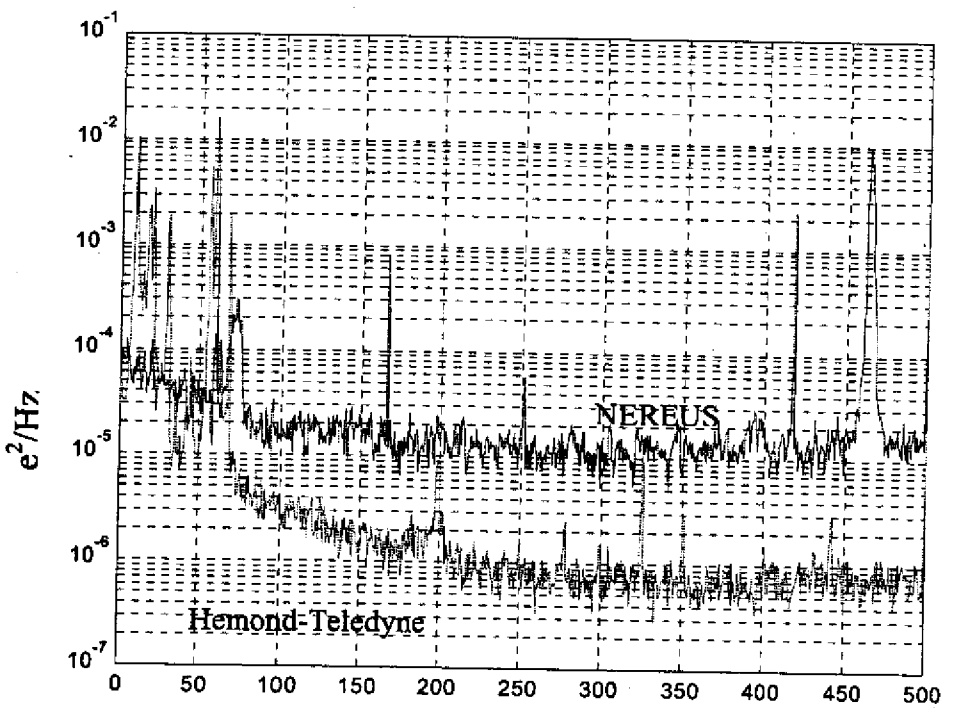

Figure 2-21: Power spectrum density comparison of NEREUS and Hemond-Teledyne electrometers.

2.4 Power system

NEREUS operates using a +12 Volt DC power supply. Electrical power can be supplied to the instrument either from its two internal 12 volt 7 ampere-hour sealed lead-acid batteries (connected in parallel) or via its external 9-pin Impulse cable (common return at pin 1 and +12 volts at pin 2). The cable uses a shared power bus with the batteries, permitting the internal batteries to be recharged when power is supplied to the instrument by way of the cable connection. The 12 volt power bus supplies power to 4 electrical component groups: the ion pump, scan controller, emission regulator, and digital circuitry. These components are connected to the +12 volt terminal by way of a fused main toggle switch that then branches to individually fused toggle switches for each of the four component groups. The five toggle switches are positioned immediately forward of the scan magnet on the frame's composite mounting plate, and electrical wires to the switches are routed through a wiring harness with a square 12 pin Amphenol connector. This connector can be detached to permit easier access to components housed within the lower hemisphere. Connector pin arrangement is detailed in Table 2-4.

Function	*Pin number*
Computer/DAQ	1, 5
Emission regulator	2, 6
Scan controller	3, 7
Ion pump	4, 8
Main	9, 10
No connect	11, 12

Table 2-4: Power system wiring harness connector

Fuse ratings and approximate current draw for individual component groups during operation are specified in Table 2-5. Return paths for each of the previously mentioned electronic components are individually routed to a short length of 12 gauge "common bus" wire which connects to the negative battery terminals and pin 2 of the Impulse cable.

Switch	Fuse rating (Amperes)	Current draw (Amperes)
Main	5	1.7
Embedded computer & DAQ	1	0.5
Emission regulator	2	0.7
Scan controller	2	0.2
Ion Pump	5	0.3

Table 2-5: Current requirements and fuse ratings of electronic circuits

The embedded computer and DAQ rely on a series of dedicated DC-DC converters and voltage regulators to supply necessary positive and negative voltages. A DC-DC converter (Power One model DFA6U12S5) transforms the battery's unregulated +12 volts into +5 volt regulated output of up to 6 watts; the embedded 386 computer and DAQ require typically require a total of 900mA during operation. A parallel second DC-DC converter (Power One model DFC10U24D12) uses the unregulated +12 volts to generate regulated ±12 volts at 24 watts. A voltage regulator (Film Microelectronics model FM905S7) is connected in series to the –12 volt output of this DC-DC converter to generate a regulated –5 volt source capable of sourcing up to 7.5 watts at peak. Both the ±12 volt converter and the –5 volt regulator are capable of generating power in excess of the digital circuitry's respective ±50mA and 20mA requirement, but were chosen based on their higher efficiency over other types of inverters and regulators (e.g. zenier diode, band gap, etc.). Outputs from these converters, the regulator, and a common return path are routed to the embedded computer and DAQ system on a braided five-wire power harness and connector that bifurcates into two 10 base-T Ethernet jacks mounted to the instrument frame's composite plate. Wiring at the Ethernet jacks is described in Table 2-6.

10 base-T Wire #	Color	Function
1	Orange & white	GND
2	Orange	+5 volts
3	Green & white	NC
4	Blue	+12 volts
5	Blue & white	-5 volts
6	Green	-12 volts
7	Brown & white	GND
8	Brown	+12 volts

Table 2-6: 10 base-T power connector wiring

Electrical power to the electrometer is supplied using a separate internal battery pack consisting of four 1.5 volt AA and two 9 volt alkaline primary batteries. This independent electrometer power supply was selected to minimize interference from switching loads generated by the other electronic components.

2.5 Component housings, frame, and mounting apparatus

The NEREUS prototype fits within a 17-inch glass Benthos pressure sphere. The upper hemisphere of the pressure sphere houses the analyzer and ancillary components including embedded computer, DAQ board, electrometer, emission regulator board, ion pump, magnet, and high voltage power supply. Initial design layout of the instrument [cite Camilli 2000] was prepared using Ray Dream CAD software to project component shapes within the allotted pressure sphere volume. Shape, size, and positioning of the instrument components were then adapted based on the Ray Dream renderings, enabling an approximately 50% decrease in instrument size beyond initial proposal estimates which called for the instrument to occupy an entire sphere volume.

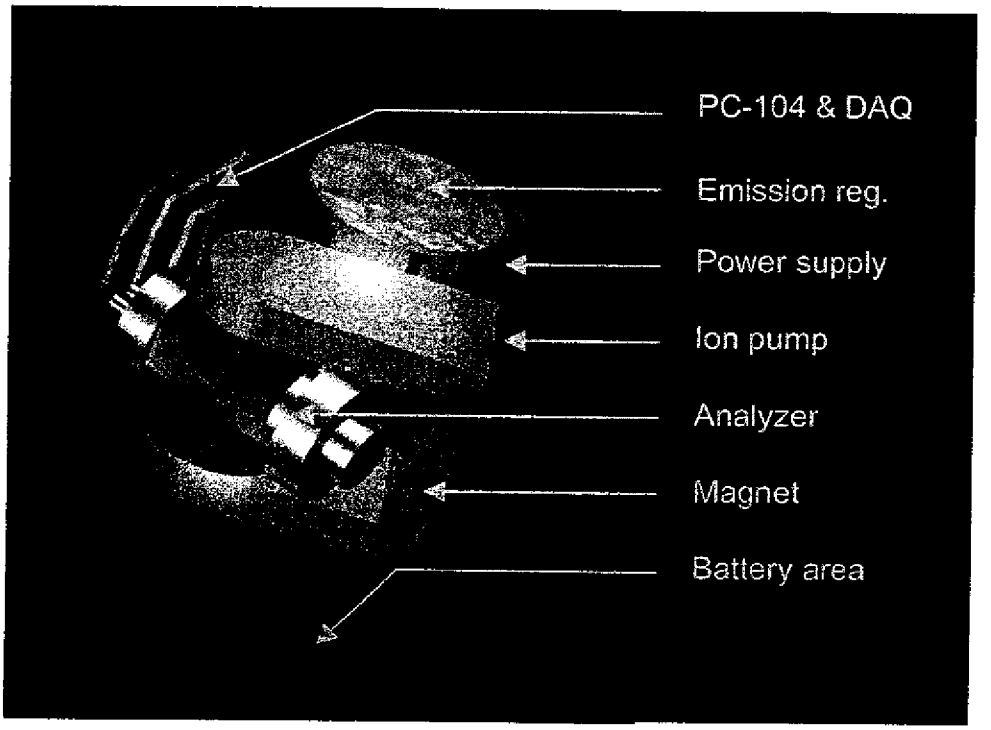

Figure 2-22: Layout of NEREUS components within pressure sphere

The volume made available through this additional miniaturization of the instrument has allowed for space within the lower hemisphere to reserved for placement of an internal battery pack, which can be used to power the instrument. This battery pack is composed of two 12 volt 7 Amp hour seal lead acid batteries and can easily be modified to accommodate other types batteries, including rechargeable secondary varieties such as lithium ion, nickel cadmium, and silver zinc, and non-rechargeable primary batteries, such as the alkaline D-cell packs commonly used to power *in-situ* oceanographic instruments.

2.5.1 Frame

NEREUS components are held in place using a composite frame. The composite material has the advantages of being lightweight, non-corroding, electrically nonconductive, and non-magnetic. The supporting frame uses an inverted quadripartite

geometry, similar in design to those seen in building and bridge vaults. This geometry is resistant to shock loads, permitting batteries to be housed in the lower hemisphere while securely holding the instrument components in the upper hemisphere. Frame surfaces are constructed from 6 oz. medium density 90° woven glass fiber impregnated with epoxy resin. The upper mounting ring utilizes an internal high-density styrene foam core, with eight radially embedded brass hard-points that are threaded to accept pan head hex bolts. These eight hard-points serve to fasten the instrument mounting plate to the frame. The frame, in turn, is fastened to the glass sphere via a composite disk that is bonded to the base. The frame is secured with stainless steel screws at six hard points in its base.

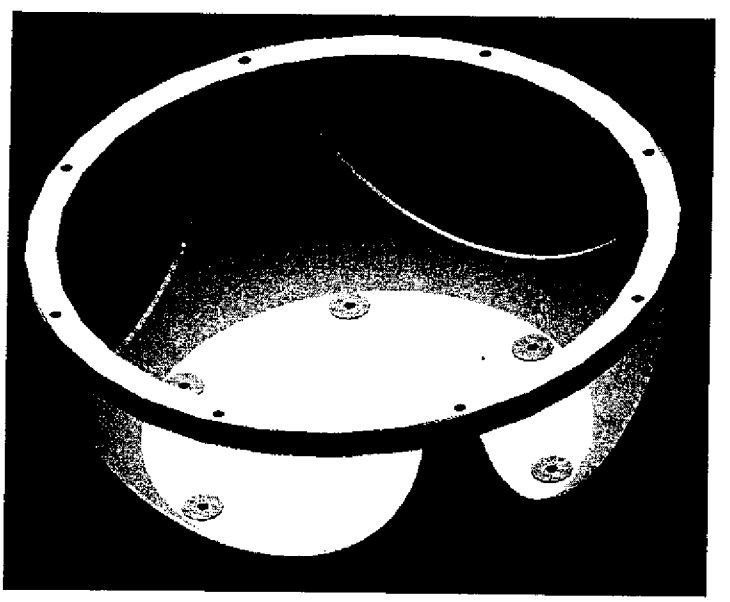

Figure 2-23: NEREUS instrument frame

2.5.2 Mounting plate

The composite plate is shaped with a series of recesses and openings to securely position the analyzer magnet, ion pump housing, vacuum system valves, and 10 base-T type power connector sockets. The ion pump, analyzer magnet, and vacuum envelope are zip tied in place to prevent dislodgment in case of roll over. Construction of the plate involved first vacuum forming 10 layers of epoxy impregnated 6 oz. medium density 90° woven glass fiber with weave pattern offset of 45° between adjacent layers. A rigid

polyurethane cast was then made of the analyzer magnet-vacuum system assembly, which, in turn, was used to produce a male mold. The male mold's perimeter was then traced onto the composite plate and the internal area then cut away from the plate. Next, the male mold was placed within the cutaway region and an additional 5 layers of similar epoxy impregnated glass fiber with 45° offset was hot vacuum formed onto the existing 10 layers. Hot vacuum forming was accomplished by placing the composite plate within a Reynolds oven roasting bag (commonly used to roast turkeys). The bag was then sealed and connected to a vacuum pump to evacuate gas voids from the composite while it cured within a drying oven set to 85° C. Finally an epoxy top and bottom coat was applied to the composite plate, and holes were drilled to accommodate the zip ties, thru-bolts, vacuum valves, and power connectors.

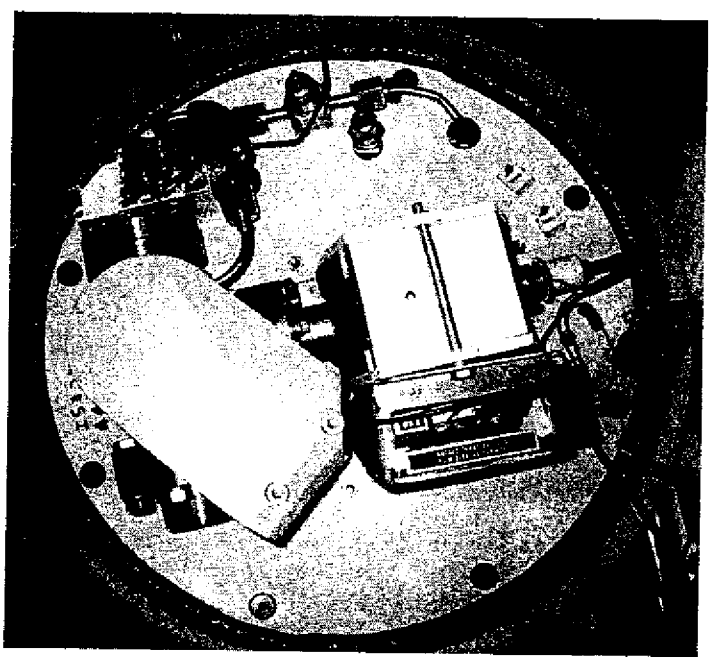

Figure 2-24: Mounting plate placement of analyzer, detector and ion pump assemblies

2.5.3 Instrument cover

To further secure the analyzer components and prevent electrical short circuiting of the ion pump's high voltage power supply, a specially shaped composite cover fits over the ion pump, power supply, analyzer magnet, vacuum envelope, and electrometer. This

cover is constructed of the same epoxy impregnated glass cloth as the composite plate, utilizing a thickness of 5 layers in most areas, and up to 12 layers in obvious high stress areas. Close fitting of the cover was achieved by sculpting a clay mold of the previously mentioned component assembly along with required hollow areas. After the mockup dried to a satisfactory hardness, it was then coated with Vaseline (serving as a mold release) and then the composite cloth was applied and hot vacuum formed using the previously mentioned process.

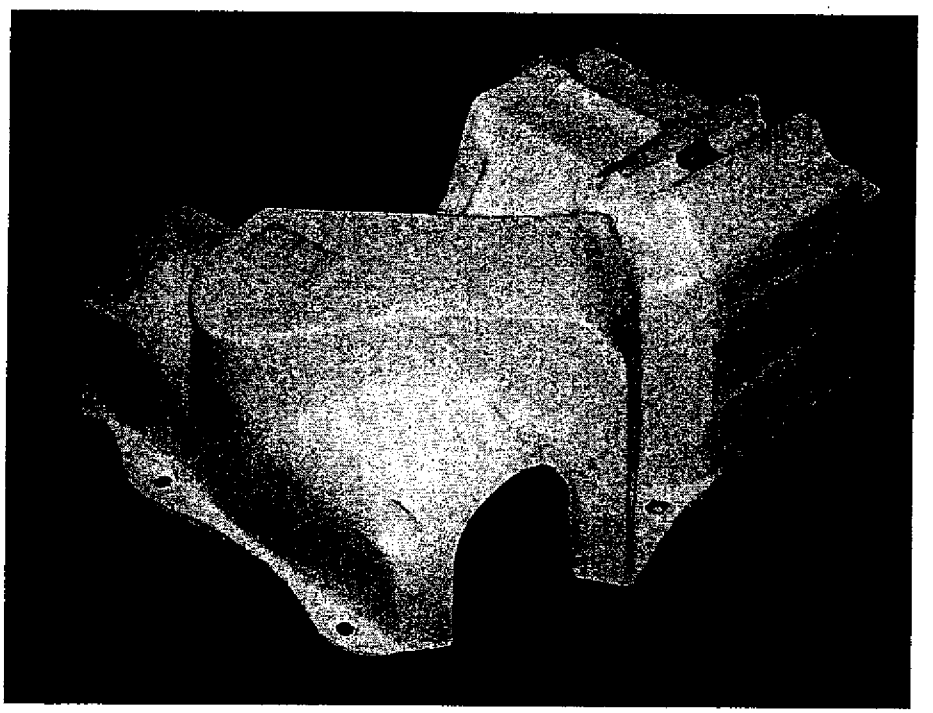

Figure 2-25: Composite instrument cover

2.5.4 Attachment disk

The frame is attached to the sphere via six bolts that are fastened into to a rigid semi-spherical support disk. This support disk is constructed of epoxy coated two-part polyurethane foam with internal copper mesh and stainless steel wire reinforcement connected to six threaded stainless steel hard-points. Polyurethane was chosen as foundation material because of its high strength to weight ratio and its casting ease.

Construction of the support disk required that the frame and internal surface of the lower pressure sphere be covered with a mold release. To minimize cost, common food storage plastic wrap was used. After the release was in place, the six stainless steel hard-points (constructed of a stainless steel nut welded to two stainless steel washers) were bolted to the frame. After securing the hard-points, 1 ½ inch width copper mesh was woven through the washers in a six-pointed star pattern, with overlapping mesh intersections. Internal points of the star with mesh overlapping between hard-point mounts were then tied to directly opposing mesh angles, using 16-gauge stainless steel wire. These mesh and wire reinforcement elements were then formed into a bowl shaped contour, similar to the internal surface of the pressure sphere. Once these steps were complete, the two part polyurethane foam was mixed in a 1 to 1 ratio, to an unexpanded volume equal to 1/10 of the volume between the bottom of the frame and the pressure sphere was poured into the sphere. The frame was then mounted to a square plywood sheet and placed concentrically within the lower pressure sphere, ensuring uniform sphere compression space and that the top of the frame traversed the sphere equator. Once adequately cured, the support disk was removed and painted with a thin layer of epoxy to provide additional strength and prevent catastrophic failure of the foam. The support disk is bonded to the glass pressure sphere with RTV silicone. RTV material was selected as the bonding agent because it provides good adhesion and is flexible, thereby allowing for sphere compression at depth and helping to absorb shock loads created by mechanical impacts.

2.5.5 Electronics housings

Electronics boards, including the emission regulator, scan controller, DAQ, and embedded computer are housed within small composite cases to prevent short circuiting, protect circuitry from water leaks, attenuate electromagnetic interference, and to organize placement of the boards within the pressure sphere. These housings are constructed of the same 6 oz. woven cloth used for fabrication of the instrument frame and cover.

These cases were constructed by applying epoxy resin impregnated glass cloth over polyurethane foam molds (sized to maintain adequate internal space for circuit boards and connectors). After attaining adequate wall thickness, surfaces of the emission regulator, scan controller, and DAQ were finished and then covered in metal foil to

minimize electromagnetic interference. To minimize adverse magnetic field permeation affects on an internal reed relay, the DAQ case also utilizes two .045" thickness mild steel plates in the area directly beneath the relay.

Housings are bolted together using stainless steel screws and nuts. Electronics housings containing the PC-104 computer, DAQ system, emission regulator, and scan controller are fastened to the external surface of the instrument cover using Velcro strips. Although unconventional, Velcro was chosen over other fasteners based on its light weight, magnetic inertness, and immunity to vibration.

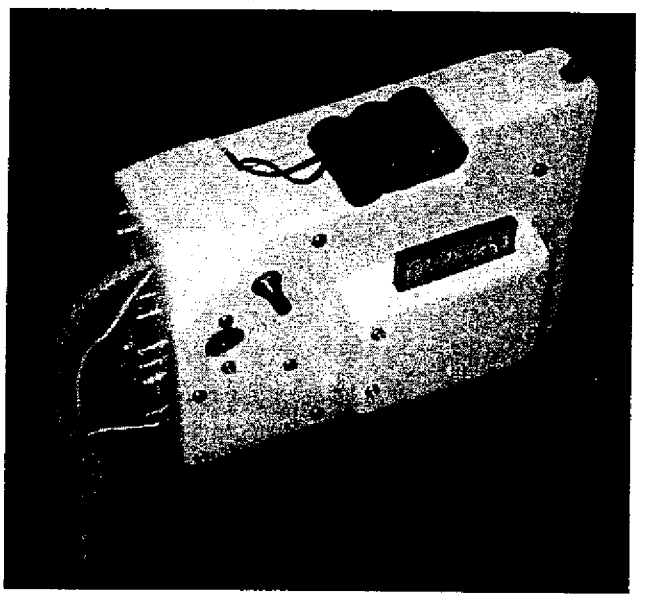

Figure 2-26: Embedded computer with memory card

2.5.6 Hardhat protector

A high-density polyethylene "hardhat" protector is used to protect the NEREUS instrument from impacts during transport and tethered deployment. The lower hemisphere of the hard hat has been modified by two separate circular holes that permit the inlet system to protrude and allow access to the sphere's vacuum port. A series of square cutouts have also been made to the upper hemisphere of the hardhat, which permit viewing of the ion pump and electron trap current gauges while the instrument is covered.

Approximate overall neutral buoyancy is achieved for the instrument and hardhat assembly through the use of a rigid polyurethane foam spider that has been cast into the ribs of the upper hemisphere hardhat, along with a second polyurethane foam disk that is attached to the top of the hardhat. The placements of these floatation pieces were chosen to maximize the separation between the system's centers of gravity and buoyancy, allowing the instrument to remain upright when deployed on a tether. The hardhat is fastened closed using four eyebolts. A ½" diameter rope harness is then threaded through the bolt eye holes and tied to the tether.

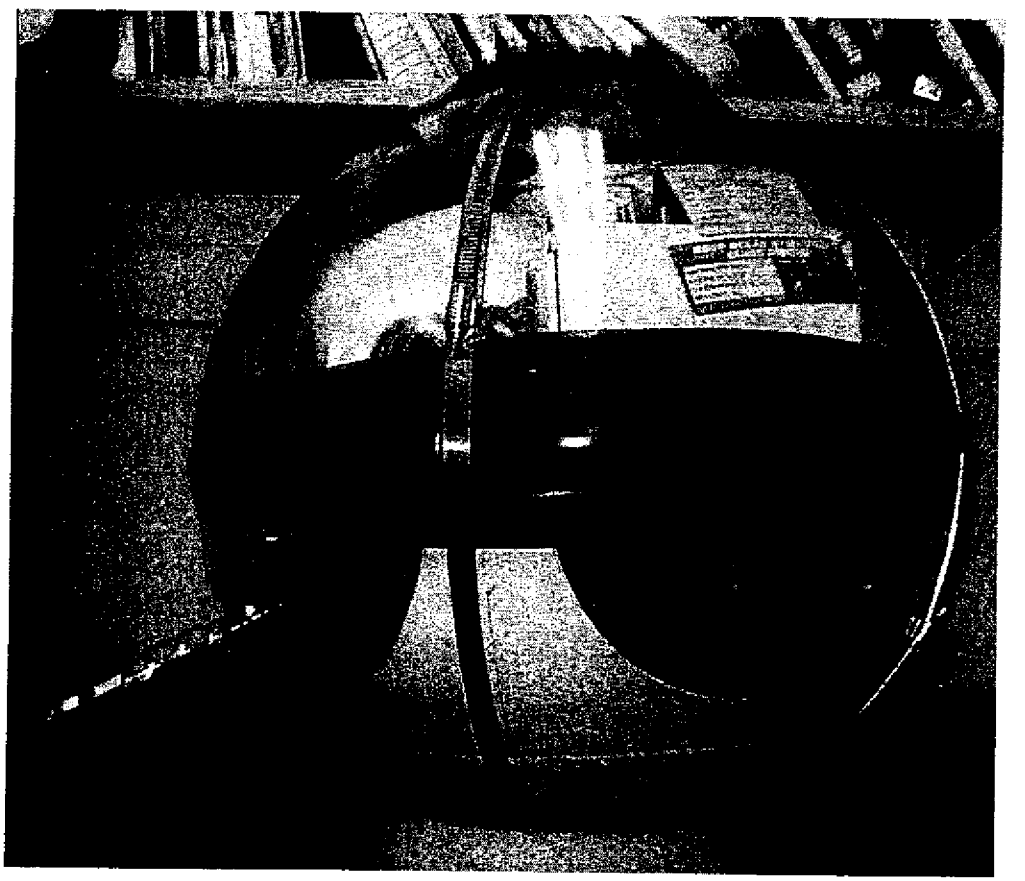

Figure 2-27: The NEREUS instrument, shown sealed within its pressure housing prior to deployment

2.6 Instrument startup and sphere sealing

Once the components of the NEREUS instrument have been properly wired and assembled, the startup process can be initialized. This involves:

1. Connect roughing pump to NEREUS vacuum system Quickflange.
2. Open NEREUS vacuum system valve for external pump down.
3. Vacuum pump system to 10^{-8} Torr.
4. If vacuum envelope operation pressure has not been maintained, then open vacuum envelope valve and continue pump down process.
5. After proper vacuum system pressure has been attained, turn on "main" and "ion pump" power switches.
6. If the ion pump current meter is stable and draws less than 200μA, then turn on "computer", "scan board" and "emission regulator" power switches.
7. Verify that the computer boots and that cycloid trap current meter displays between 5 and 10 μA.
8. Verify successful mass calibration using either an external computer connected via radio link, or monitor connected to the embedded computer's VGA output.
9. Verify that scan routines can be executed as directed from remote computer.
10. Close roughing pump valve and disconnect roughing pump
11. Verify that ion pump current remains stable.
12. Disconnect all external wires.

After the NEREUS instrument initialization has been successfully performed, the instrument can then be sealed through the following process:

1. Clean hemisphere mating surfaces with alcohol or similar solvent.
2. Carefully place upper hemisphere on lower hemisphere, taking care not to chip glass surfaces.
3. Rotate upper hemisphere so that alignment marks match on hemispheres
4. Remove vacuum port screw and evacuate to 0.8 ATM.
5. Quickly replace vacuum port screw and verify that the sphere holds vacuum.
6. Apply "monkey dung" as a continuous bead around the mating surfaces.

7. Firmly press and smooth monkey dung to glass surface.
8. Remove monkey dung backing tape.
9. Wrap wide plastic electrical type tape around the equatorial region three times, beginning slightly below the equator, then transitioning to slightly above the equator on the second turn, and completing the third wrap on the hemisphere.
10. Secure two metal band (hose type) clamps around the sphere. Position clamps in a longitudinal arrangement, intersecting each other to form an "X" at the top and bottom poles of the sphere.
11. Place sphere in Kemonaut AUV, or protective polyethylene hardhat.
12. Attach dummy plug to MIL-9 cable if external radio transceiver is not being used (e.g. during AUV deployments).

Chapter 3

SOFTWARE

Autonomous operation requires that the NEREUS instrument be able to perform all necessary functions via its embedded computer system. Minimum functionality includes powering instrument on and off at predetermined intervals, mass step calibration, accelerator potential control, emission regulator control, data collection and handling, systems diagnostics, and communications with auxiliary systems such as radio transceivers, remote viewing terminals, or vehicle navigation computers. To satisfy these operational needs as well as power and space limitations, NEREUS uses an embedded PC-104 computer possessing a 486 core module operating at 100MHZ with a standard MS-DOS 6.2 operating system. The NEREUS operational code is a compiled stand-alone executable file that automatically loads during the computer booting sequence. Data files and the executable are stored on a 128 MB flash disk configured as a fast IDE drive; data files are specified by their *.NDF (nereus data file) extension. Functionality of the instrument is enhanced through a supervisory control architecture that allows for human or machine input to direct NEREUS operation via one of its two serial ports.

3.1 Embedded Code

The embedded NEREUS software was written and compiled using Microsoft Quick Basic 4.5. This language was chosen based on the Hemond research group's computer language familiarity and its ability to be run both as interpreted and compiled code, a useful feature for development and debugging. Although Quick Basic is relatively limited in its functioning, subroutines were developed to overcome these shortcomings, including utilization of direct memory addressing for accessing parallel port registers, and iterative for-loop structures to introduce timing delays where precision to less than one second is required.

3.1.1 Embedded display and user interface

A display is of minimal value because the embedded computer system is intended for unmanned operation of the NEREUS instrument while it is sealed within its protective housing and submerged. Therefore, only a rudimentary display was developed, and is intended to function exclusively for computer file management and bench top troubleshooting. This display generates a text based VGA output and can be connected to a standard CRT monitor via a VGA jack located in the aft of the PC-104 housing. ASCII text is output to the display in a columnar format consisting of: mass scan voltage, apparent M/Z, ion signal and time.

The embedded computer accepts an AT type keyboard, which can be used to access the BIOS as well as files within the operating system. Pressing the F8 key during the booting sequence circumvents execution of the autoexec.bat and embedded code files, thereby permitting file access from a DOS prompt. Alteration to extended BIOS options is accomplished by pressing CTRL-ALT-ESC during the boot sequence, which causes a configurable POST screen to be displayed, whereupon various BIOS settings can be modified using the keyboard. Table 3-1 describes the proper extended BIOS settings for NEREUS' embedded computer. In addition to the flash disk, the core module's floppy interface can be connected to a floppy drive for data transfer when the upper pressure housing is removed.

Configuration Option	Setting
System POST	Express
Core Module extended BIOS	Enabled
Advanced Power Mgmt BIOS	Enabled
Serial Port 1	Enabled
Serial Port 2	Enabled
Parallel Port	SPP/BPP
Floppy Interface	Enabled
IDE Interface	Enabled
Mono/Color Jumper	Color
Onboard DIP Socket	Disabled
Local Bus Video Display	CRT&FP
Flat Panel Display Type	8
Video State	Enabled
Blank POST Test	Disabled
Serial Boot Loader	Disabled
Watchdog Timer	Enabled
Hot Key Setup	Enabled
SCSI BIOS service	Enabled
SCSI Initiator ID	7
SCSI Disk Retries	10
SCSI Disk 1	Id 0, Lun 0
SCSI Disk 2	Not Active
SCSI Disk 3	Not Active
SCSI Disk 4	Not Active
SCSI Disk 5	Not Active
SCSI Disk 6	Not Active
SCSI Disk 7	Not Active
1st Hard Disk	Auto
2nd Hard Disk	Not Active
3rd Hard Disk	Not Active
4th Hard Disk	Not Active
5th Hard Disk	Not Active
6th Hard Disk	Not Active
7th Hard Disk	Not Active
8th Hard Disk	Not Active
Console Output Device	Video
Console Input Device	Keyboard

Table 3-1: Embedded computer BIOS settings

3.1.2 Instrument Control

The embedded computer uses a bi-directional parallel port connection to the DAQ to maintain instrument control. The parallel port is accessed through direct memory addressing (DMA) to four registers: configuration, data, status and control, residing at hexadecimal memory addresses of 77A, 378, 379 and 37A respectively. The configuration register serves to specify data transfer mode; in the case of NEREUS, a value of 32 written to the 77A address sets the port to PS/2 data transfer mode. Bi-directional data exchange takes place via the data register using a signaling pattern previously described by Camilli [cite]. Under this regime data is transmitted across an 8-bit data bus using a "two pass" architecture in which binary output data is sent to the 16-bit digital-to-analog converter as an 8-bit high-byte packet followed by an 8-bit low-byte packet. Binary 2's compliment data is read as input from the 16-bit analog-to-digital converter in a similar fashion, wherein an 8-bit high-byte is read first, followed by an 8-bit low-byte. To synchronize the data transfer process and thereby avoid data packet collisions, the 8 data register bits are connected to a double-tiered bank of multiplexers on the DAQ. Bits 0,1 and 2 of the parallel port's control register operate the multiplexer gates, while bit 5 dictates directional control for the bi-directional data register and bit 3 actuates a transistor-driven reed relay functioning as an on/off logic switch for the emission regulator. Status register bits 3 through 7 are reserved to detect the logic states of various failsafe indicators. Bit assignments for the data, control and status registers are detailed in Table 3-2.

Register bit	Function	DB-25 pin
Data 0	Data in/out	2
Data 1	Data in/out	3
Data 2	Data in/out	4
Data 3	Data in/out	5
Data 4	Data in/out	6
Data 5	Data in/out	7
Data 6	Data in/out	8
Data 7	Data in/out	9
Status 3	Ion pump failure	15
Status 4	Emergency valve	13
Status 5	High pressure indicator	12
Status 6	Low Battery	10
Status 7	Unused	11
Control 0	Converter select	1
Control 1	Byte select	14
Control 2	AD569 chip select	16
Control 3	Emission regulator on/off	17
Control 5	Data input/output	NC

Table 3-2 Parallel port registers and functions

3.1.3 Calibration

Calibration of mass-to-charge (m/z) focus relative to the scan controller input potential generated by the DAQ is required to accurately scan for and identify ion peaks within the cycloid's spectral range. Initially a software application was developed that scanned three separate peaks and generated a linear slope-offset equation based on the three peak centers (Figure 3-1). This application required human operator input from a remote laptop computer linked by radio transceiver to select the calibration gases and to conclude the slope offset calculation. Extensive testing of this calibration system revealed that non-ideal effects, most likely a consequence of the scan controller's high gain

circuitry, causing the cycloid's electric field potentials to correspond non-linearly with scan controller input. Additional analyses indicated that this non-linearity did not affect the monotonicity of the relationship but did introduce a degree of distortion large enough to preclude accurate tuning of ion peaks with an m/z in excess of 30 AMU. Moreover, radio transmission interference occasionally would produce transmission errors that caused the embedded computer to generate cycloid plate voltages considerably different from their intended values. Although this error could be overcome either by redundant command transmission, or through post processing of signals for error correction, both methods could only be implemented with substantial time penalties. Therefore, an alternate system of calibration was developed.

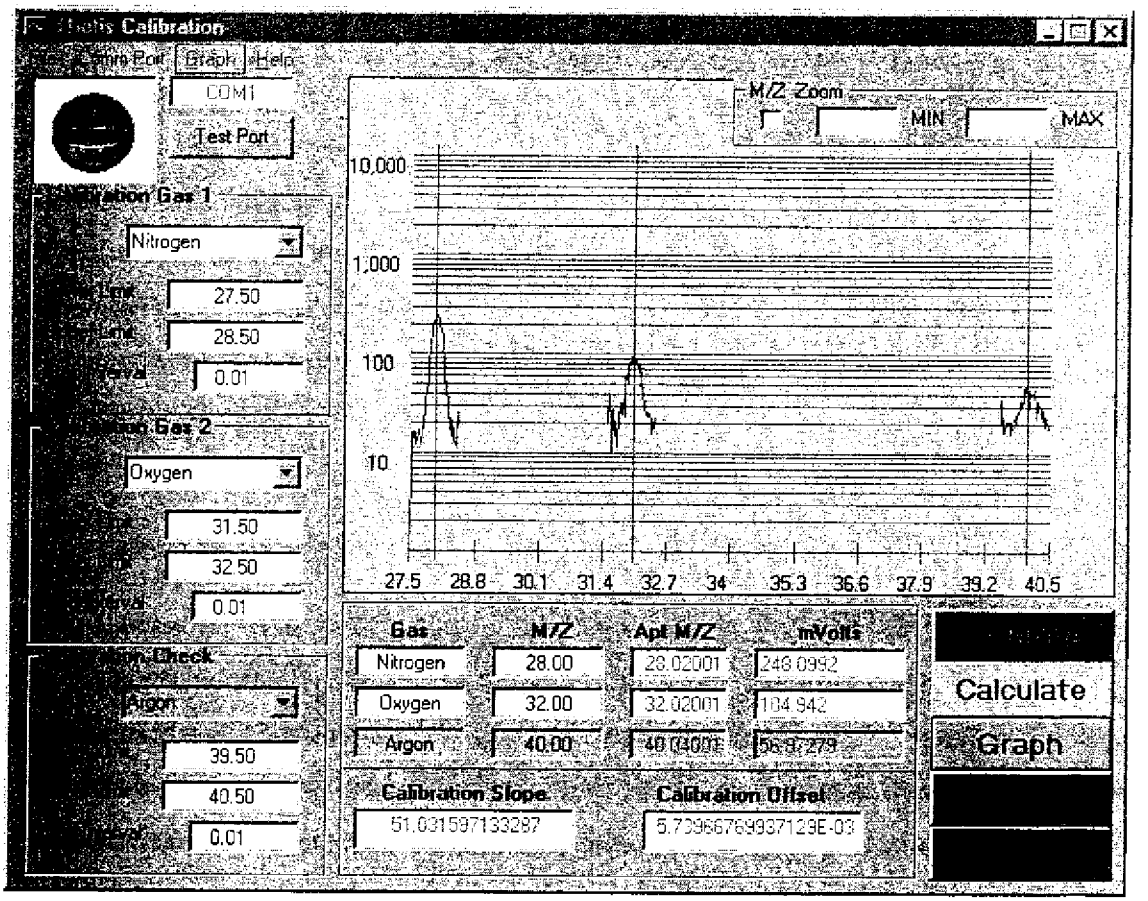

Figure 3-1: Remote calibration GUI for NEREUS instrument

To overcome the drawbacks of the first generation calibration system, all functions requiring communication with an external agent, human or computer, were eliminated in favor of a completely autonomous system. In addition, an algorithm was developed that iteratively compares the residuals of likely variable values to produce a least-squares-fit exponential equation. This second-generation calibration system also makes use of an error checking procedure, which was developed to verify that newly generated calibration variables are within acceptable error margins. Failing a successful calibration, the instrument undertakes a limited number of retries before discontinuing the process and reverting back to the most recent valid variables stored in memory.

Calibration is initiated at each computer boot-up and at hourly intervals thereafter. The calibration routine involves scanning for three peaks at mass-to-charge ratios of 16, 20 and 40. These peaks were selected based on their presumed universal expression under all marine environmental conditions, expecting that an oxygen peak at m/z =16 will persist either as an atomic fragment of water or as doubly charged molecular oxygen. Similarly, persistent peaks appear at m/z = 40 and 20 as a result of singly and doubly charged argon. Other peaks occurring at m/z = 17, 18 and 28 (water fragment, water and nitrogen) are also universally present, but can generate ion current intensities that exceed the full scale of the detector and in doing so obscure the peak's exact center. Signal saturation is problematic because precise center determination is crucial for generating the two calibration variables (i.e. slope coefficient and m/z exponent) with precisions resolved to at least four significant digits in order to maintain sufficient focus accuracy in the high m/z range of the spectrum. To ensure accuracy, the calibration curve's RMS error is verified to be less than 10 mV before the new variables are stored in memory. Once the calibration process is complete, the variables are used to generate appropriate scan controller input voltages by raising the desired m/z to the power of the exponent variable (n) and then multiplying the result with the slope variable (m), yielding the proper scan controller input voltage.

$$\text{Scan Voltage} = m(M/Z)^n$$

Equation 3-1: Mass calibration equation

The compiled code relies on a 24-hour clock using a dual precision floating point value for task scheduling. Therefore, to prevent the instrument from generating an error when the most recent calibration occurred before midnight and a calibration is scheduled for after midnight, a time checking algorithm was developed which accounts for this offset and adjusts scheduling accordingly.

3.1.4 Operational modes

A suite of embedded behaviors allows the NEREUS instrument to respond to input from various external agents and environmental conditions. These behaviors minimize the power and time required to gather relevant data at an appropriate resolution by controlling the sleep/wake state, type of scan undertaken, and amount of signal averaging that is performed. Execution times vary from seconds to tens of minutes, depending on the scan mode and signal averaging combination that is executed.

A total of six scan modes are available to the instrument, four of which are spectral sweeps ranging from either 12 to 48 or 12 to 150 with step intervals of 0.5 or 0.1 AMU. The remaining two scan modes make use of a peak jumping strategy, which allows the instrument to rapidly monitor 15 peaks by evaluating only the peaks regions and thereby omitting m/z spectral regions of minimal interest.

Gradient tracking, one of the peak jumping modes, permits the instrument to adjust the time interval between successive scans according to absolute value of amplitude changes in the m/z peaks that are being monitored. This behavior relies on an algorithm that compares the peak heights of the most recent scan with the corresponding peaks of the previous scan. If any of the peaks have changed amplitude by 100% or greater, the instrument immediately commences a new scan. If the maximum amplitude change is greater than 40% and less than 100%, the scan interval is decreased by a factor equal to the peak height change, multiplied by the scan interval. If the largest peak height change is between 30% and 40%, the scan interval remains unchanged. If the greatest peak height change is less than 30% and the scan interval is less than three minutes, the scan interval is increased by a quantity of seconds equal to 2 divided by the peak height change, up to a total delay interval of 3 minutes. When the delay interval is greater than 30 seconds, the instrument immediately cycles into a standby mode, using the computer

to turn off the emission regulator for a duration ten seconds less than the delay interval. The emission regulator is then powered up ten seconds before the standby interval ends to allow sufficient time for electron beam stabilization.

3.1.5 Signal Averaging

While in operation the instrument can assume seven different signal-averaging intervals, two of which involve variable signal averaging. The five fixed signal-averaging routines are 500, 1000, 2000, 5000 and 10000X, thereby decreasing statistical error to 4.5%, 3.2%, 2.2%, 1.4% and 1.0% respectively. The variable signal averaging conducts repeated sampling until the absolute value of the integrated electrometer voltage relative to baseline exceeds either 50 volts or 100 volts, and to avoid baseline clipping, relies on a baseline determination which is set equal to 75 mV less than the ion current sensed at m/z = 11.5 AMU. This dependency on the number of samples averaged to the integrated voltage causes the same relative magnitude of statistical error to be generated for each data point (i.e. signal to noise ratio); thus avoiding excessive sampling of large signals, or under sampling of smaller signals. To minimize the time required for calibration, a process requiring at least 300 data points, a limited 25X signal averaging routine is used (yielding a statistical error of 20%) because just relative maxima are needed.

The signal averaging process entails that the appropriate mass first be tuned, and then a 20-millisecond delay be instantiated to allow sufficient time for the electrometer output to stabilize. After this delay period has ended, the DAQ's analog-to-digital converter repeatedly samples the electrometer output in uninterrupted succession until the signal averaging parameters have been satisfied. Execution of each sample cycle requires approximately 30 microseconds, resulting in respective times of 35, 50, 80, 170 and 320 milliseconds for the 500, 1000, 2000, 5000 and 10000X signal averaging routines. Time requirements for the variable signal averaging regimes cannot be predicted with complete certainty in advance of their execution because sampling times are a function of the magnitude of the electrometer output voltage and various noise sources, causing higher electrometer output signals to require less sampling time and smaller signals to demand longer signal averaging. In addition to the signal averaging time requirements, further

time is allotted for data handling and response delays associated with capacitive coupling of the cycloid E-field plates.

3.1.6 Data handling

A measurement of electrometer current is made of M/Z=11.5 at the start of each scan. This value, which is expected to be representative of the sensor baseline voltage, is used to normalize the digital-to-analog converter signal to a baseline value. The converter, which is uses a +5 to –5 volt scale and 2s complement code to express electrometer voltage, electrometer noise generally causes the electrometer baseline value to fluctuate within a +70 to –70 mV range. Therefore, to minimize data character lengths and thereby save data storage space and speed data transfer, the electrometer voltage signal at M/Z = 11 is subtracted from the subsequent values. Finally, a value of 70 is added to the ion signal in order to prevent this normalized signal from dropping below zero.

3.1.7 Data storage

Once the requisite sampling and normalization has been fulfilled, the signal data is averaged to produce a single data point. The data point is then stored within a data file using an 8-character hh-mm-ss.ndf ASCII string time-stamp name. The contents of these data files are structured using comma-separated variable formatting. A file header is contained within the first four lines of each data file. The first row records the date of the scan using a month-day-year format followed by the descriptor "NEREUS embedded data", denoting that the file was created by the embedded computer. It is worthwhile noting that the BIOS of the initially used PC-104 386 core module was afflicted with the Y2K problem, making it necessary to describe all embedded system dates using a single decade offset (e.g. a date with the year 2002 is stored as 1992). The date problem was corrected by replacing the 386 core module with a 486 core module. Row two of the header provides descriptors for each of the four data columns and arranged in order of scan voltage, m/z, ion signal, and time. The scan voltage recorded in addition to the m/z and ion signal because the scan voltage can be used in conjunction with the m/z and ion signal data to retroactively identify scan controller faults. A time stamp is associated with each data point to allow the various spectra ion peaks to be temporally referenced with data from other sensors (e.g. 3-D position, conductivity, temperature, etc.). Rows three

and four of the header are left blank. Data values are stored beginning at row five and continuing on to the end of the file.

To minimize the probability of data loss, a new data file is created at the start of each scan, after saving and closing the currently open data file. In addition, data files are saved and closed when the instrument enters its sleep mode. While the instrument is in sleep mode, the embedded computer continuously polls the calibration timer to see if a recalibration is scheduled for immediate action. If a recalibration is required, the instrument awakens from its sleep mode to recalibrate and once the recalibration has ended, the instrument opens a new data file using the current time stamp for name, then conducts a single scan using its peak-jumping mode. After the scan is complete, data from this scan is then saved and the data file closed before the instrument resumes its sleep state. This process cycles continuously until the system is instructed to commence a scanning mission. To ensure that the instrument responds to an incoming command, a subroutine continuously polls the communication system to check if an input message has been received. Upon receiving a valid new mission scan command, the system reawakens from sleep mode the computer generates a new data file using the current time for naming and recommences the data collection process.

3.2 Supervisory control

In addition to autonomous operation, NEREUS is capable of receiving and acting upon mission updates from an external agent using the communications protocol described in the previous sections. This agent may be human or an external computer and inputs can be routed through either of the PC-104's two RS-232C serial ports. This system of supervisory control enables the external agent to subsumptively command [76] the embedded system to alter mission directives in real time by modifying the scan mode, signal averaging, or entering into a sleep mode.

The NEREUS instrument control system can be regarded as an augmented finite state machine in that it is a situated robotic sensor and its possible modes of operation are finite in number and are executed based on input signals collected by its data acquisition system and from external agents such as its radio transceiver or serial line input. Every degree of instrument freedom is not controlled by the embedded computer, causing the

control system to function as a non-holonomic system [77]; therefore, a robust communications system was developed to prevent the embedded control system from entering into an indeterminate state.

3.2.1 Communications protocol

To reduce instruction set length, thereby minimizing transmission time requirements and increasing the likelihood of successful message transmission, commands are sent to the embedded control system as an encoded two letter and one numeral ASCII string (Table 3-3). The string consists of a scan mode letter, followed by a signal average letter, then by a single digit number. Each letter uniquely specifies an option and a corresponding integer value. The purpose of the numeric third character is to prevent the instrument from entering into an indeterminate state as a result of an erroneous command. This encoded character is used to prevent the control system from entering a indeterminate state by providing a validation that the two alphabetic characters are accurate using an abbreviated version of a cyclical redundancy check, which is generated by multiplying the associated values of the two variables, followed by a modulo 7 division of the product (Figure 3-2 provides an example of a valid command message string). When a command is received by the embedded system, correct framing of the character positions is accomplished using a range of A through G for the first character, T through Z for the second position, and a value of 0 through 7 for the third position character. The most recently received command satisfying this criterion undergoes the previously described modulo 7 computation and the resulting value is then compared with the third position numeric character of the encoded command. If the values are identical, the message is determined valid and a confirmation response is sent to the remote system, followed by execution of the command.

Character	Function	Position	Value
A	12-48 AMU range, 0.1 AMU step	1st	1
B	12-48 AMU range, 0.5 AMU step	1st	2
C	12-150 AMU range, 0.1 AMU step	1st	3
D	12-150 AMU range, 0.5 AMU step	1st	4
E	Peak Jump	1st	5
F	Sleep	1st	6
G	Gradient Track	1st	7
T	Low count variable signal averaging	2nd	20
U	High count variable signal averaging	2nd	21
V	500 X signal averaging	2nd	22
W	1,000 X signal averaging	2nd	23
X	2,000 X signal averaging	2nd	24
Y	5,000 X signal averaging	2nd	25
Z	10,000 X signal averaging	2nd	26

Table 3-3 Command string functional elements and values

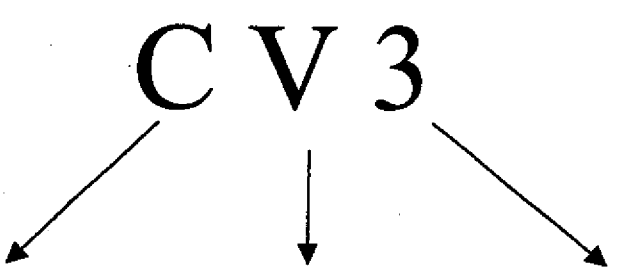

Figure 3-2: Valid command string example

Messages transmitted out from the embedded computer are ASCII strings of variable length and can be of two types: data, or text. Therefore, each message class uses a unique set of start and stop characters. Data messages are composed of a "$" character start bit, followed by a string representation of the comma separated scan controller input voltage, mass-to-charge ratio, and electrometer voltage data values, followed by a "&" stop character. Text messages make use of a "#" start character, followed by the text string message, and concluded with a "@" stop character. Data messages are sent to the external agent to enable real time data analysis and redundant data storage. To avoid transmission time associated delays, particularly when using the 9600 bit per second radio transceiver, only 0.5 m/z interval data is sent. Text messages inform the external agent of instrument condition states. These text messages include information regarding states of calibration, emission regulator, mission changing, sleep mode, and time until next scan sequence, and excessive peak height warnings.

3.3 Remote Graphical User interface

A remote graphical user interface (GUI) has been developed to enable a human user to monitor the instrument performance, modify instrument execution procedures and interpret chemical data in real time. This capability can significantly enhance the scientific discovery process by minimizing time delays common to iterative sampling and thereby reveal data relationships while still in the field [78, 79]. The GUI was written and compiled into an executable file using the Microsoft Visual Basic 6.0 language, and it is designed to operate with a 32 bit Windows based PC operating systems such as Microsoft Windows 95, 98, 2000 and XP. The software relies on a RS232 serial port to asynchronously communicate with the embedded NEREUS computer.

The GUI, named Thetis Spectral Viewer consists of two windows, a pop-up window that appears at startup time, and a main window. The pop-up window (Figure 3-3) provides the computer user with information about the software and presents two fields for the user to enter his or her login name and password. The login name and password were written into this software to prevent commands from being accidentally sent to the NEREUS instrument or unauthorized operation of the instrument. The pop-up window is

withdrawn and main window is presented once the user has successfully logged in. A series of communication startup procedures are initiated when the user logs in, including, identification of available serial ports, designation of port to be used and designation of bit transfer rate.

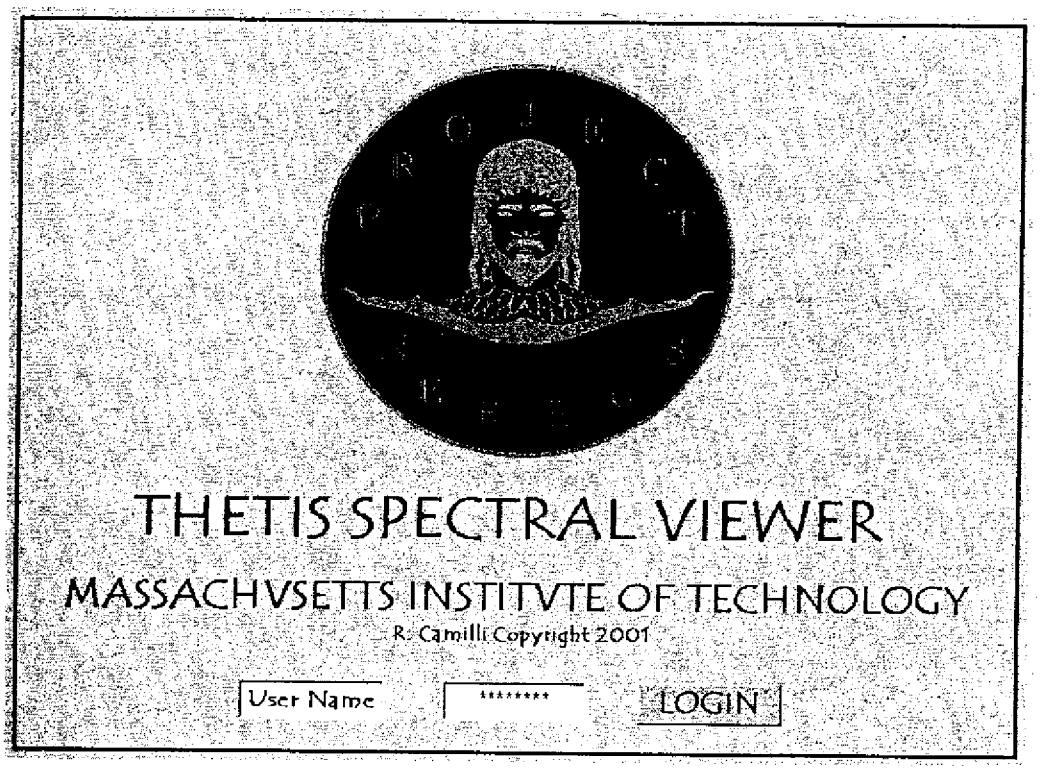

Figure 3-3: Thetis Spectral Viewer login window

3.3.1 Main window

The main window consists of several independently functioning graphical elements. Across the top of the window is a standard upper tool bar. Directly below this is a row of checkboxes to allow up to eight gas peaks to be simultaneously monitored and three communication command buttons. Below the checkboxes are two sets of radio buttons for selecting signal averaging and scan type, and to their right is a histogram. Below the histogram is a slider bar. To the left of the histogram and below the radio buttons is a spectrum display. At the bottom of the window is a status bar indicating communication

status, scan type, data state, and degree of magnification. To the right of this status bar is a set of checkboxes, which enable scrollable viewing of the histogram using the slider bars and viewing of the data in tabular format.

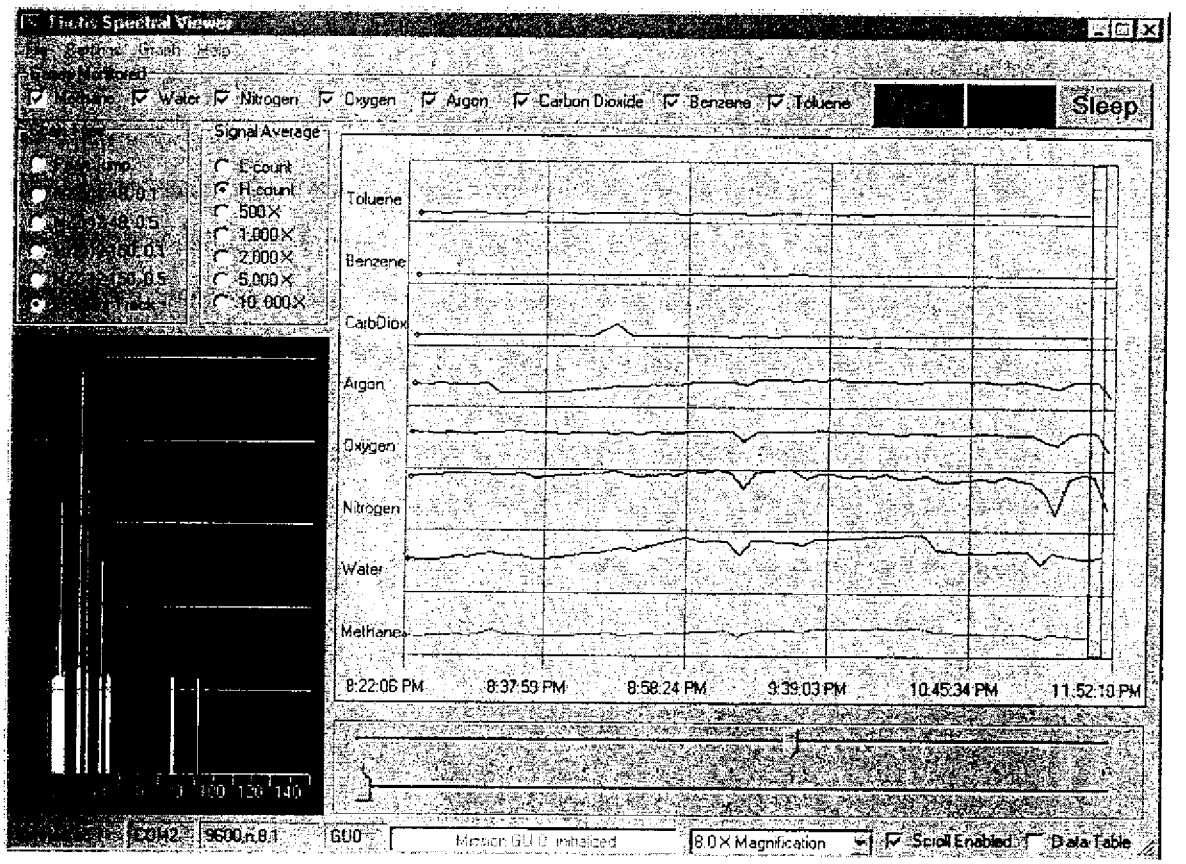

Figure 3-4: Thetis Spectral Viewer main window

3.3.2 Command initialization

Command initialization is carried out by selecting the degree of signal averaging and type of scan and then clicking the green Scan button in the upper right hand corner of the screen. This redundantly sends the appropriate 3 character ASCII command (refer to section 3.2.1) fifty times for output to the serial line. The status bar at the bottom of the GUI window is then updated to indicate if the serial port is open, which serial port it is,

the communication protocol (i.e. speed, parity, data bits, stop bits), followed by the command code.

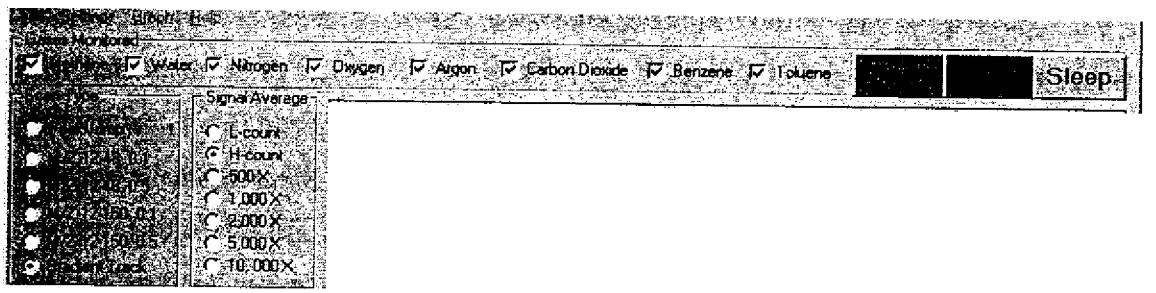

Figure 3-5:Thetis GUI command radio button fields and tool bar

The redundant send is used to temporally saturate the NEREUS radio receiver in order to overcome radio interference and allow the embedded computer to asynchronously receive and process the command string. The embedded computer then processes the command string on a FIFO basis and the last valid command code encountered is executed. If this latest command instruction differs from the previous command state of the embedded computer, the embedded computer replies to the remote computer with the confirmation string #Mission _ _ _ initialized@, where the blank spaces are the command code. This confirmation code is then parsed by the Thetis GUI and appears in the central text box within the status bar at the bottom of the window.

Figure 3-6: Thetis GUI status bar

3.3.3 Data parsing

Incoming data strings are processed from the serial port input register as soon as a single character is encountered. The input string is then sequentially parsed on a FIFO basis to identify header characters # or $. If either of these characters are encountered, the

subroutine collects all subsequent characters into an input string until it encounters a stop character of @ (if the header character was #) or & (if the header character was $). If the character is # and a matching @ character is found, then the string is considered to contain a valid text message and the string is trimmed of its start and stop characters before appearing in the central text box within the status bar at the bottom of the window. If a $ header character and matching & stop character is identified, then the internal character string is considered to be a NEREUS data string. If a second start character is encountered before a matching stop character, the input string characters are cleared and a new string is started. If the text message received from NEREUS is "Awaiting new mission", the GUI automatically replies by sending the latest command that was selected.

When a NEREUS data string is found, the data string undergoes a secondary parsing and confirmation process before being stored as valid data and being incorporated into the data display. This secondary parsing is executed by trimming the start and stop characters from the string and then dividing the string into 4 discrete strings (scan voltage, mass/charge, ion signal, time stamp) based on comma separators within the string. The 4 strings are then checked to confirm that each is within its respective valid range and that these strings are not identical to the previous data string received (*i.e.* redundant data). If all of these parameters are satisfied, the data strings are considered valid and stored in the data matrix.

3.3.4 Data visualization

The GUI visually presents the gathered data to the user in the forms of a histogram, a spectrum and an optional data table. The histogram, which is located on the right side of the window, describes peak data as a function of time, wherein the time domain is expressed along the X-axis and the ion signal intensity is conveyed along the Y-axis. The histogram field is divided evenly into a number of horizontal rows equaling the total number of gases selected in the "Gases Monitored" checkbox field and are labeled according to the gas ion being monitored in that particular row. Vertical scaling of each row is derived from the maximum peak height of all monitored ion peaks in the data range. Temporal scaling is determined by the tab positions on the slider bar when the "scroll enabled" checkbox is selected. If this checkbox is not selected, the histogram only

graphs the 100 most recent data points. Histogram graphing is accomplished by constructing individual arrays of M/Z data corresponding to the gas being monitored within the temporal domain specified by the slider bar tabs. The search process is computationally demanding, and therefore is automatically recommenced only after the serial input register has received 30 characters or if the slider bar tabs are moved or the "Gases Monitored" checkbox selections are modified.

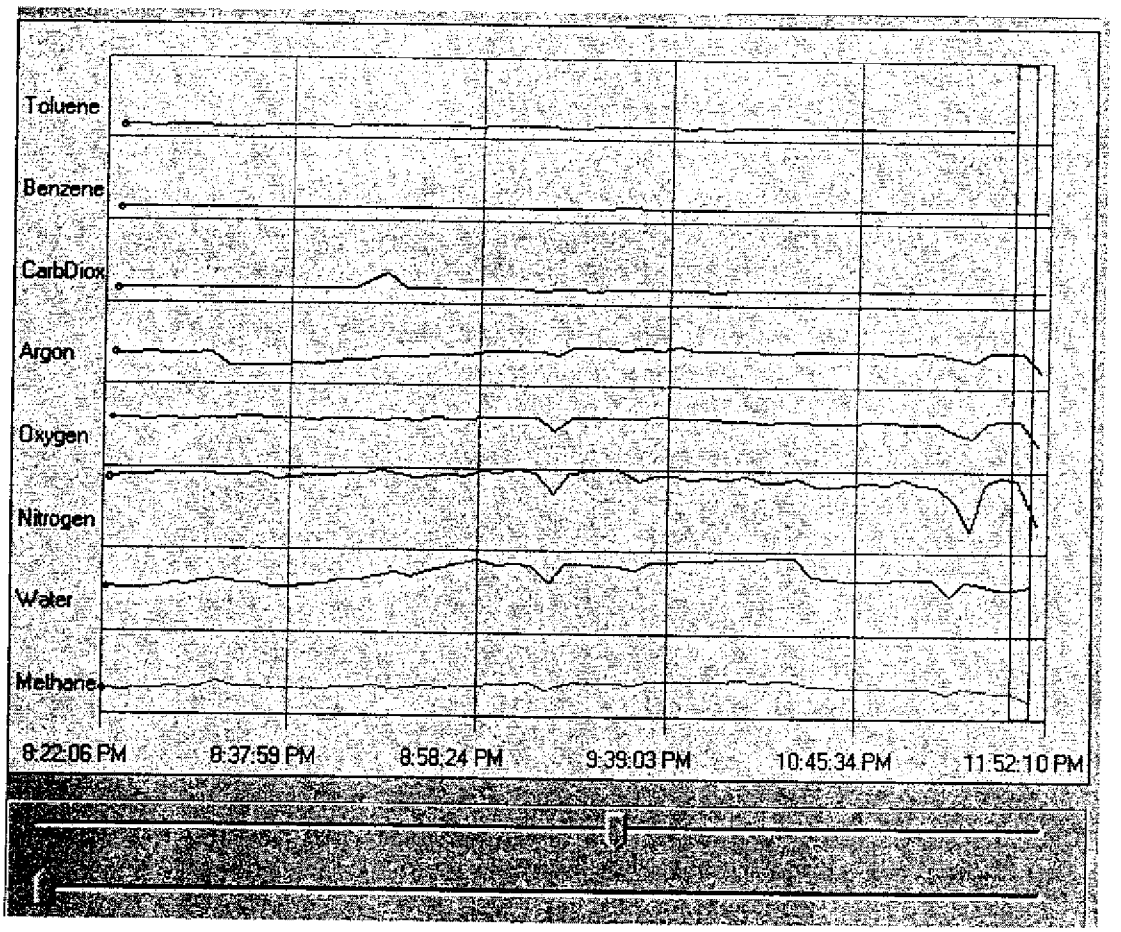

Figure 3-7: Thetis GUI histogram field with red temporal window and accompanying slider bar

The Spectrum appearing in the lower left of the window is the last complete spectrum within the time domain specified by the slider bar tabs. The red box outline appearing within the histogram field corresponds to the temporal domain of the spectrum. This time

domain window allows the user to place a particular spectrum within the contextual history of previous data. The spectrum makes use of an auto scaling function that scales the spectrum both vertically, as a function of the maximum electrometer signal observed within the spectrum range, and horizontally to the width of the display field.

Ion signal intensity in both the histogram and the spectrum can be re-scaled by selecting a magnification factor of 1 to 9 with the "magnification" combo box located in the status bar at the bottom of the window. This causes the spectrum to display the vertical fraction of data equal to the lower 1/n of the ion signal range. Meanwhile, the histogram displays the lower 1/n signal range fraction of the ions monitored, and the solid grey line is replaced by a dotted red line if a particular ion is off scale for that time period.

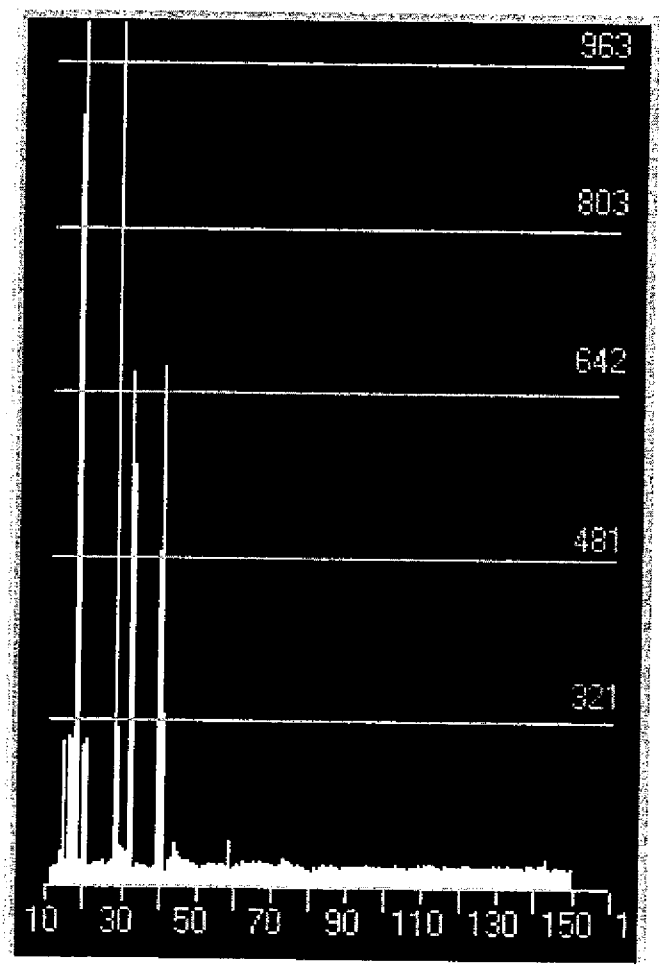

Figure 3-8:Thetis GUI spectrum field

In addition to the histogram and spectrum displays, an optional data table is available for viewing. This data table appears as an overlay of the histogram field and is selected using the checkbox on the right hand side of the status bar. The data table is continuously updated with new incoming data and is scrollable using the vertical scroll bar on its right.

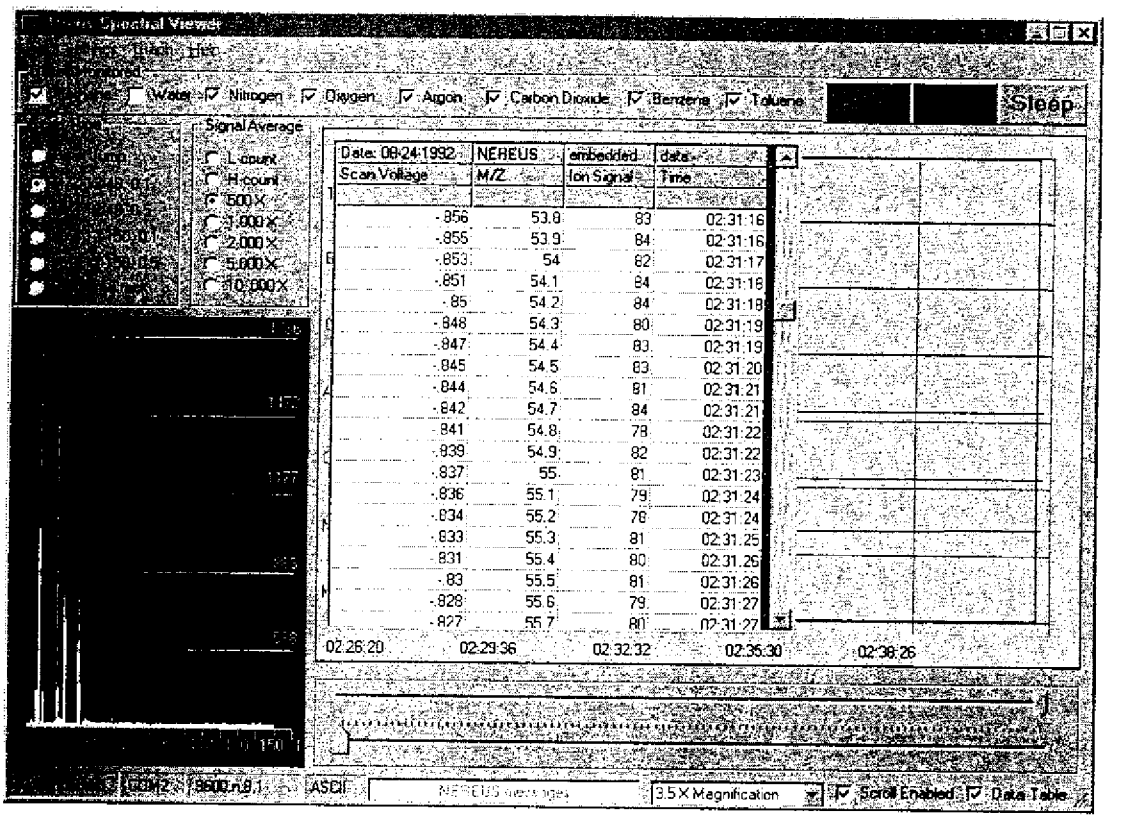

Figure 3-9: Thetis Spectral Viewer main window with data table visible

3.3.5 Data storage and retrieval

Data storage and retrieval is available directly from the software. These tasks are accomplished by selecting either the "Open" or "Save" commands within the "File" menu in the menu bar. When data transmitted from the NEREUS instrument to the GUI is saved, it is saved in a format identical to *.ndf files generated by the NEREUS embedded computer. File naming is left up to the user. The file header generated by the

GUI differs from the embedded computer in that its first line does not include the descriptor "NEREUS, embedded, data". The GUI is capable of opening all files with the *.ndf designation. Any currently open file is automatically closed when a new file is opened.

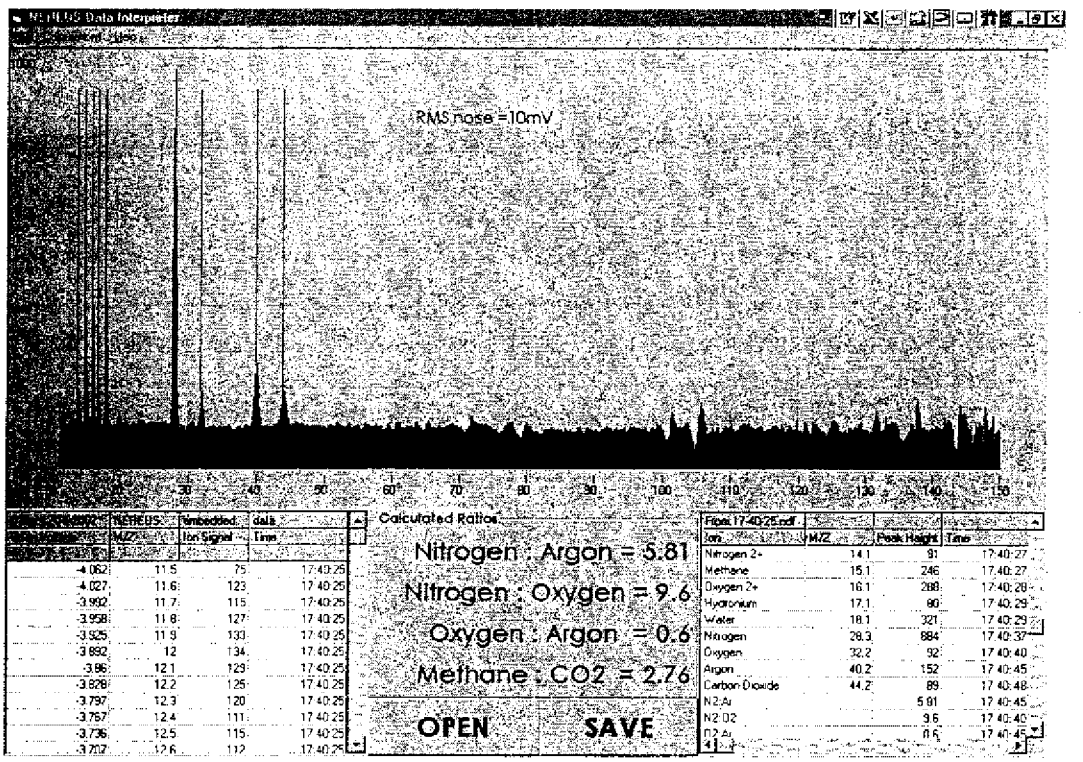

Figure 3-10: NEREUS Peak Interpreter GUI

3.4 Quantitative peak evaluation

As the NEREUS instrument has evolved, its data collection rates have significantly increased to the point of making unaided analysis and quantification by a human impractical. During three brief NEREUS instrument deployments in the Upper Mystic Lake and Boston Harbor over 400 discrete spectra were generated, with each spectra composed of 1385 data points. Therefore, to automate the process of quantifying ion peak heights and thereby significantly reduce the required time for analysis, an additional piece of software was developed. This program, named NEREUS Data Interpreter,

facilitates the assessment, compression and merging of NEREUS spectrum data. The software was specifically developed to identify and quantify ion peaks at M/Z = 14, 15, 16, 17, 18, 28, 32, 40, 44, 78 and 93, corresponding to nitrogen, methane, oxygen, water, argon, carbon dioxide, benzene, and toluene ions.

A simple peak apex detection algorithm [80] searches for major peaks within ±0.5 M/Z of these specified ranges by examining data points adjacent to $M/Z_{(n)}$ so that:

$$M/Z_{(n-3)} < M/Z_{(n-2)} < M/Z_{(n-1)} \leq M/Z_{(n)} \geq M/Z_{(n+1)} > M/Z_{(n+2)} > M/Z_{(n+3)}$$

Equation 3-2: Peak-finding algorithm

If a peak is identified, the program then calculates the baseline using three data points on either side of the peak apex. When the peak M/Z is less than 20, the upper and lower base line averages are calculated using data points in the M/Z regions from +0.3 to +0.5 M/Z, and -0.3 to -0.5 M/Z. If the peak M/Z is greater than 21, the upper and lower base line averages are calculated using data points further away to compensate for decreased M/Z resolution in the higher mass ranges, in the M/Z regions from +1.4 to +1.6 M/Z, and -1.4 to -1.6 M/Z. These upper and lower baseline values are then averaged create an ensemble baseline average and is subtracted from the peak apex to find the net peak height. RMS noise values are calculated independently for the upper and lower baselines and then combined to create a composite RMS baseline noise value. If the net peak height exceeds the composite RMS baseline noise value by at least a factor of 3, the peak is considered to be statistically distinct from the baseline noise and is recorded as an actual ion peak. The GUI presents the user with a display of the spectrum, along with red lines through each of the identified peaks. To the left and right below this spectrum display are two scrollable data tables containing the raw *.ndf data and the calculated peak height data, respectively. The calculated peak height data is organized in a columnar format consisting of: ion type label, apparent M/Z, ion peak height, time stamp. In addition, this data table also calculates ion peak height ratios when available of nitrogen-to-argon, nitrogen-to-oxygen, oxygen-to-argon and methane-to-carbon dioxide. These ratios are also displayed in large text in the area between the two data tables. Below the text

display of the calculated ratios are two command buttons, "OPEN" and "SAVE". The "OPEN" button allows the user to browse and select stored *.ndf files, and the "SAVE" command saves the calculated peak heights and ratios to a *.npi (NEREUS Peak Interpreted) file. If a new file name is not specified, the GUI will automatically save the *.npi file with the name of *.ndf file that was used to generate the peak height data. All *.npi files are stored in a columnar format of comma separated variables, similar to the *.ndf files and include a file header specifying the *.ndf file that was used to generate the data.

Chapter 4

AUTONOMOUS UNDERWATER VEHICLE DESIGN

The NEREUS instrument is designed to function aboard an Odyssey Class autonomous underwater vehicle, having been originally proposed as payload within an Sea Grant Odyssey II or Bluefin Robotics Odyssey III type vehicle. Both the Odyssey II and III are derived from the Odyssey I predecessor which was developed by the MIT Sea Grant AUV Laboratory and first underwent field trials off of New England in 1992. The Odyssey concept focuses on AUVs that are small enough to be easily deployed and are of low component cost. A key factor among these design parameters is the use of low-cost mass produced glass flotation spheres, which commonly function as floats to full ocean depth of 6,000 meters. These glass spheres house vehicle electronics, sensors and power systems in a dry one-atmosphere environment, permitting the use of a free flooding vehicle hull, thereby minimizing vehicle volume and displacement requirements. The Odyssey I vehicle design which made use of 3 glass pressure spheres and a free flooding fiberglass hull displaced 195 kg, with an overall length of 2.1 meters and maximum diameter of 0.59 meters [81].

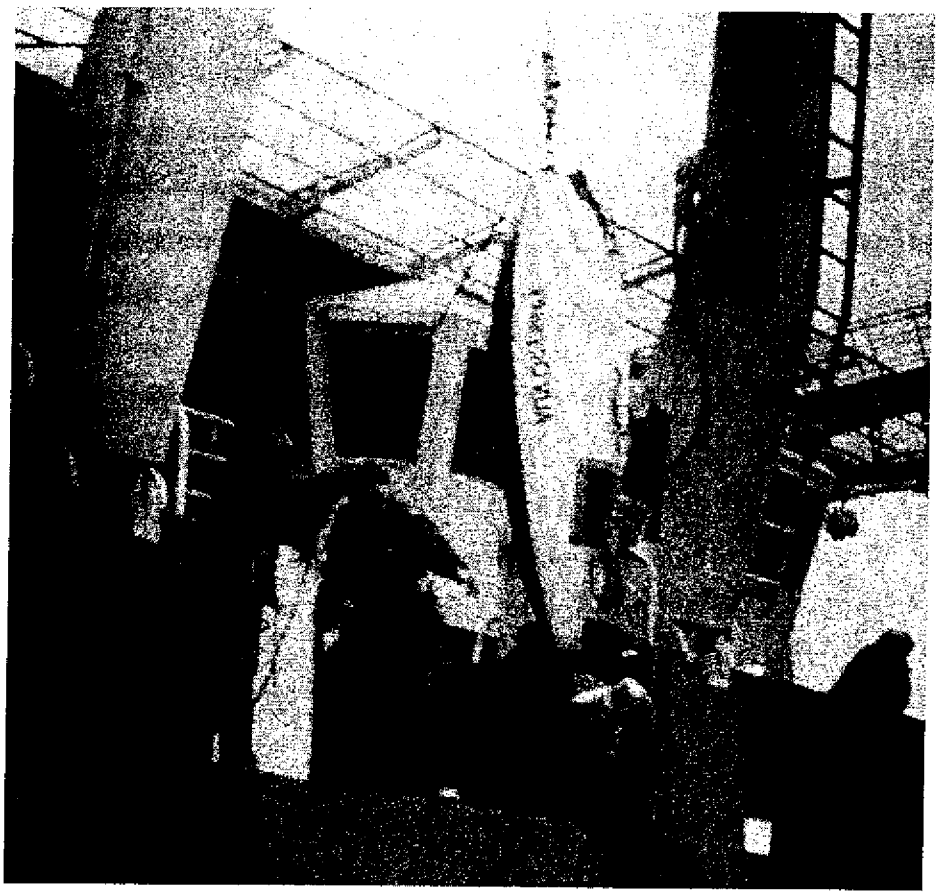

Figure 4-1: Odyssey I vehicle (courtesy of MIT Sea Grant)

4.1 Odyssey II design overview

In 1994 the Odyssey II generation began deployments in the Beaufort Sea to explore mechanics of Arctic sea ice. Like the Odyssey I, this second generation does not require any special handling equipment for launch and recovery, and to function at full ocean depth using spherical glass instrument housings. Unlike the highly experimental Odyssey I, the Odyssey II is a smaller displacement vehicle, which utilizes a molded double hull design composed of high-density polyethylene, allowing for inexpensive mass production as well as increased impact resistance [17]. Other significant differences are decreased vehicle displacement, the core vehicle displacing approximately 120 kg and an increased emphasis on modularity, permitting the Odyssey II vehicle reconfiguration according to mission requirements such as substitution of sensor payloads and rapid updating mission

profile libraries stored in the vehicles navigation computer. These design elements assist in optimization for simultaneous use of multiple vehicles, leading to an overall increase in synoptic coverage efficiency, energy management and robustness to component failure [82]. Over the past decade, this design philosophy has proven both functional and robust, resulting in several hundred successful dives and the Odyssey IIb, IIc and IId subclasses. These subclasses, which were developed to satisfy specific mission goals, retain the same hull design and external dimensions of the Odyssey II, at an overall length of 2.2 meters and 0.58 meters diameter. The first of these adaptations, the Odyssey IIb configuration, was equipped with updated navigation control systems that relied upon a simplified distributed intelligence working across RS232 serial communication lines coupled to onboard sensors and actuators. The IIb design was first deployed in a month-long experiment in June of 1996 to study the dynamics of frontal mixing in the Haro Strait near Vancouver Island, in which five vehicles were arrayed with various water quality sensors, side-scan sonar, and acoustic Doppler current profilers [83]. Following the successful Haro Strait experiments, the IIb design was augmented with various types of cameras and deployed in numerous expeditions. Among others, missions to New Zealand in search of giant squid in the Kaikoura Trench and to the Labrador Sea to study thermohaline cycling of ocean waters [13]. In the first half of 2000 two Odyssey IIb vehicles, named Xanthos and Borealis, were again updated with new navigation control and sensor systems and dubbed IIc. Navigation control updates included replacing the onboard Motorola 68040 based computer with a new PC-104 based main vehicle computer (MVC), a high precision long-baseline navigation system using Kalman filtering, a fluxgate inertial navigation sensor system, GPS synchronized microsecond timing, and acoustic telemetry . During the Generic Oceanographic Array Technology experiment (GOATS 2000) the Xanthos IIc vehicle was equipped with an 8-element sonar array mounted in a "swordfish" configuration on the vehicle's nose, along with a Roxann bottom classification echo sounder, while the Borealis IIc vehicle carried a sub-bottom profiler [84]. Collectively, these modifications sought to permit closed loop navigation control and multi-vehicle operations in which the AUVs worked together to achieve a common survey mission to transect a pre-specified area and measure the

acoustic field produced by the insonified targets and accurately navigate by acoustic means [84].

Following these experiments, the Borialis vehicle was cannibalized for spare parts and the remaining Xanthos vehicle was reconfigured by the AUV Laboratory in June of 2001 for Archaeological video survey work in the Mediterranean Sea [85]. This new survey configuration came to be known as the Odyssey IId, and contained all of the core vehicle components included in the IIc configuration as well as a ROS Navigator Video camera positioned just forward of the vehicle thruster along with a downward looking illumination source in the nose of the vehicle (cite SG website). The Odyssey IId Xanthos was updated again by MIT Sea Grant in 2002 with a WHOI micro modem, an alkaline primary battery replacing the silver-zinc secondary battery power supply, and installation of a navigation software named Mission Oriented Operating System (MOOS) [86, 87].

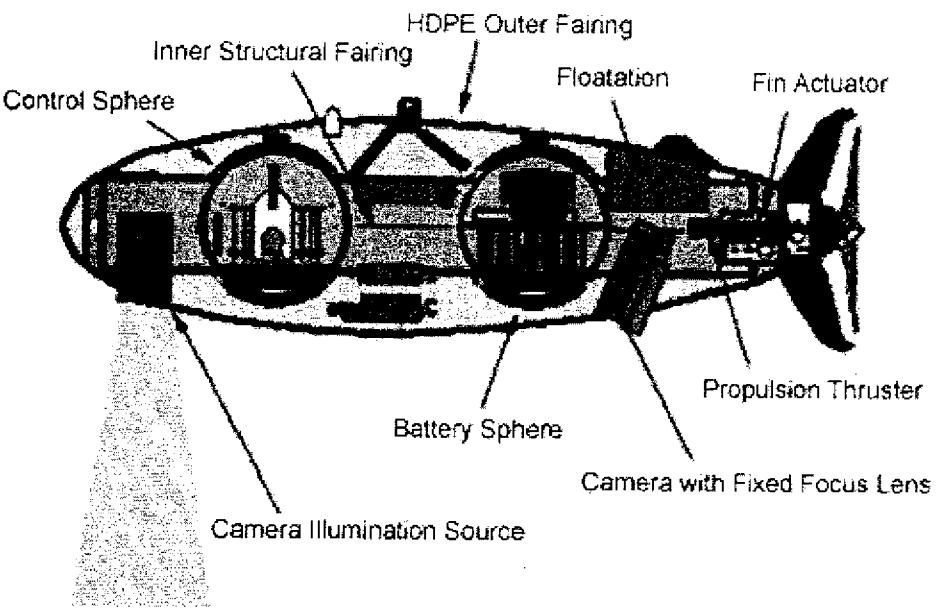

Figure 4-2: Odyssey IId Xanthos AUV

4.2 Odyssey III design

The Odyssey III, which was developed by Bluefin Robotics, an MIT startup company, is based on the Odyssey II design. In 2001 the MIT Sea Grant AUV Laboratory acquired an Odyssey III vehicle, named Caribou, from Bluefin Robotics for sonar survey research. Like the previous Odyssey designs, it uses internal glass pressure spheres to house electronics and instrumentation, and a free-flooding outer hull. In 2002 the Caribou control system was adapted by MIT Sea Grant to use the MOOS architecture [87]. Unlike the Odyssey I and II, the Odyssey III uses a modular hull, designed to accommodate various sonar, camera, and oceanographic systems in modular center payload sections and relies on a single vectored thruster, rather than a combination of fixed axis propeller with elevator and rudder fins. In addition to these differences, the Odyssey III power supply is a lithium polymer battery housed in a cube-shaped pressure compensated epoxy-resin case instead of a glass pressure sphere. The Caribou is significantly larger than previous Odyssey Generations, displacing approximately 400 kg, with a length of 2.6 to 3.4 meters (with and without central payload module, respectively).

Figure 4-3: MIT Sea Grant Odyssey III Caribou AUV

4.3 Kemonaut development

In August of 2002, after having undergone successful limnologic and marine trials, the NEREUS instrument was ready for integration into an Odyssey class AUV. At this time MIT Sea Grant's single remaining Odyssey II Xanthos vehicle used both of its internal pressure spheres to house vehicle power, control, and communication systems, making it physically impossible to accommodate the NEREUS instrument without

consolidation of the components into a single sphere. The process of Xanthos sphere consolidation was estimated to take several months, at a cost of several thousand dollars, and was not entirely clear to work satisfactorily. On the other hand, NEREUS deployment aboard MIT Sea Grant's Caribou vehicle was also impractical due to an insufficient understanding of vehicle dynamics using a center payload section with the vectored thruster and MOOS architecture, and because a center payload section was unavailable for NEREUS. Purchase of a payload section from Bluefin Robotics was estimated to cost several tens of thousands of dollars, with an estimated completion time of a few months, again making deployment aboard the Caribou vehicle out of the question.

After lengthy analysis it was decided that a new type of Odyssey vehicle could be built specifically for NEREUS missions at an economic and time cost lower than that of the Caribou center section or the Xanthos reconfiguration. Design of this new vehicle, named Kemonaut, began in late October 2002 with the goal of producing an operational vehicle before winter weather delayed NEREUS deployment until the following spring. To speed the development process, it was determined that the Kemonaut design should use an external hull, tail cone, control and power system spheres identical to the Odyssey IId [84]. However, because the Kemonaut vehicle required space for three glass pressure spheres (two for standard Odyssey IId power and control and one for the NEREUS instrument) while retaining the same external dimensions of an Odyssey II hull, a number of new design factors had to be addressed, including:

- increased vehicle displacement
- decreased hull stiffness
- decreased volume for core vehicle components
- decreased volume for floatation foam
- unknown vehicle center of buoyancy, center of mass, and dynamics
- unknown navigation and communication system interference from the NEREUS instrument

To further speed the design process, Kemonaut design plans were developed on a computer using Solid Works CAD software, allowing analysis work to be undertaken

before vehicle components were built and thereby minimizing the excessive time and economic costs of iterative physical fabrication and construction cycles.

4.3.1 Design and construction

The design process began by first obtaining an Odyssey II outer hull fairing From MIT Sea Grant's AUV Laboratory. The fairing's diameter was then measured at 30 centimeter transect intervals along its longitudinal axis. These dimensions were then used to loft a computer model of the external hull shape, which served as relative boundary volume for vehicle components. Three 17" diameter spheres were then described within this internal volume, yielding a residual volume for all other vehicle components. To further increase clearance between the 3 spheres, as well as overall vehicle stability (lowering the vehicle center of mass) the glass pressure spheres were asymmetrically positioned relative to the vehicle centerline (Figure 4-4). In this arrangement the heaviest sphere containing the vehicle battery supply was located in the lower central position, the NEREUS sphere was located in the forward position, and the vehicle control sphere was positioned in the aft. This arrangement provided several benefits, including:

- Additional volume in the upper section of the hull is made available for floatation foam, further improving stability characteristics.
- Spacing between the vehicle's navigation and communication systems and the NEREUS instrument is increased, thereby minimizing electro-magnetic interference between vehicle and NEREUS systems.
- Distance between the two vehicle spheres and the tail cone is minimized, thereby minimizing required cable length.
- NEREUS sampling occurs before water is perturbed by the vehicle's motion.

Despite the advantages of this arrangement, the layout revealed that large sections of the Odyssey II structural inner fairing would need to be removed in order to accommodate the third NEREUS sphere, dramatically compromising the strength of the inner hull. Furthermore, the additional 48 kg NEREUS sphere would require greater hull strength than a standard twin sphere Odyssey II layout.

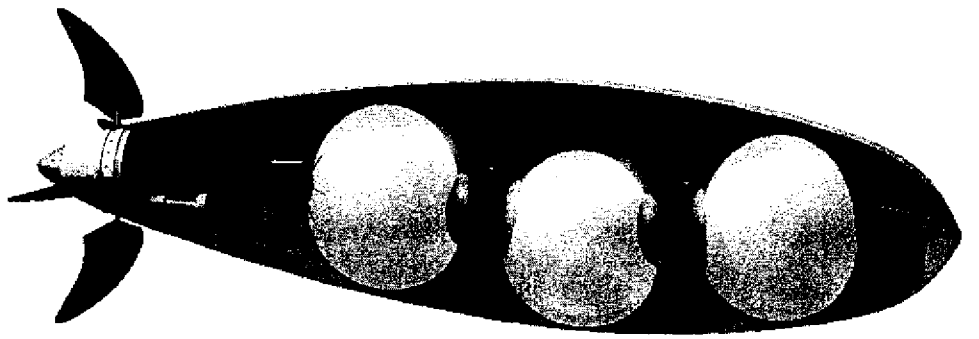

Figure 4-4:Glass pressure sphere placement within the Kemonaut AUV

To prevent hogging or more severe structural failure leading to possible pressure sphere damage during launch and recovery, an additional hull girder was essential for improved hull rigidity. However, the third sphere and an additional girder significantly reduce available volume for floatation foam, meanwhile requiring supplementary buoyancy to offset the increased displacement produced by these new components.

Similar strength and mass constraints had previously been confronted during development of the NEREUS instrument, leading to the use of composite laminates and foams in its structural elements. These materials functioned well in that they: reduced component weight by approximately 80%, endured high shock loads without failure during instrument deployments. In addition, these materials are electrically and magnetically non-conductive (a consideration when using fluxgate sensors), are generally immune to corrosive sea water, and can be fabricated into complex shapes relatively quickly and at low cost. Based on the positive results met by the composite NEREUS components, a computer design of a composite longitudinal girder was developed to fulfill the structural requirements of the Kemonaut vehicle. The contours of this surfboard-shaped component allow it to occupy the normally empty four-inch gap, running the length of the hull, between the upper and lower Odyssey II inner fairings. To further reduce the vehicle's floatation foam requirement, this girder design utilizes marine structural foam (ρ = 288 kg/m^3) sheathed in a carbon fiber cloth (ρ = 1,570 kg/m^3). The structural foam itself possesses flexural strength (rise parallel to beam thickness) of 4.8 MPa, while the autoclave cured carbon material possesses a tensile strength of 448 MPa. Because the NEREUS instrument is intended to operate to depths of

approximately 100 m, the structural foam was chosen as a compromise between the high buoyancy but depth limited low-density foams and the enormous depth capability of less buoyant syntactic foam. The carbon fiber is an autoclave cured bi-directional (0°/90°) 33 msi 2x2 twill, layered to 1.5 mm thickness, which is impregnated with an epoxy binding matrix, providing a measure of armor plating for the foam as well as a large proportion of the girder's rigidity.

Construction entailed creation of a plywood template to pattern the contours onto the carbon cloth and structural foam. These materials were then cut to shape using a high-speed spiral saw. After trimming, the upper and lower carbon fiber sections were bonded to the central foam section and vacuum cured using a small rotary pump and simple vacuum bag constructed of trash bin liners. Autoclave curing of the carbon/foam structure was not attempted, as it would have been deleterious to the strength of the foam. External sides of the foam piece were also sheathed in carbon cloth, but were bonded using an epoxy containing glass microfibers to decrease brittleness and thereby minimize the likelihood of delamination. Curing was accomplished using the previously mentioned vacuum bag technique. Cutouts for vehicle components were then made to the girder after curing was completed. The resulting composite structure has a mass of approximately 9 kg and is calculated to withstand depths to 300 meters without significant compression taking place and, due to the density of the foam, provides approximately 16kg of floatation.

After fabricating the girder, the lower inner hull fairing was modified to accept the third NEREUS sphere by excising two sphere cradles from a surplus Odyssey II inner hull and repositioning these further apart within a second Oddysey II inner hull that was trimmed to accept the transferred cradles. The third, central, sphere cradle was constructed of a non-ribbed polyethylene Benthos "hardhat". Accurate positioning of the sphere cradles was necessary because of the limited clearance between the spheres. Therefore, to insure proper spacing, glass hemispheres were placed in the cradles and aligned using the composite girder before the sphere cradles were riveted into place with stainless steel pop rivets.

A double-point lifting harness was designed instead of the single-point system that Odyssey II vehicles use for multiple reasons. First, adequate clearance was not available

for a single central lift point because of the location of the center sphere. Second, two relatively wide-spaced lift points would cause the vehicle's center of mass to reside between the two points, allowing the vehicle to be lifted without the vehicle experiencing the uncontrolled seesawing common to the single-point harness. Third, by distributing the loading between two attachment points, failure was less likely to occur. After finalizing a computer design, the lift frame was fabricated of 1/8"x 1" cross section annealed #316 stainless steel bar stock and 1" diameter stainless steel eyebolts.

Placements of those components residing outside of the spheres were decided based on orientation requirements for proper operation and computer generated clearance estimates. As such, the sonar altimeter was positioned vertically between the forward and middle sphere on the vehicle's starboard side and a cutaway was made in the underside of the lower hull to expose the altimeter's acoustic head. To help equalize weight distribution, placement of the depth sensor mirrored the sonar altimeter along the central axis, residing on the portside between the forward and middle sphere. Careful consideration led to vertical placement of the GPS Intelligent Buoy (GIB) transponder in the nose of the vehicle, permitting the transponder head to sit proud of the hull for clearer signal transmission. The battery housing supplying power to the strobe beacon was placed immediately forward and starboard of the tail cone assembly in another attempt to aid balance by offsetting the asymmetric girder cutaway required for the tail cone assembly. The strobe light beacon, GPS antenna, and radio antenna were mounted immediately aft of the lift harness' rear eyebolt on top of a 3.5 inch diameter cylindrical long-base-line (LBL) transducer that had been permanently affixed to the upper hemisphere of the Xanthos control sphere.

A modular three-piece floatation system was designed to mount within the upper half of the vehicle between the middle sphere and outer hull to increase vehicle payload carrying capacity and further improve stability. Six pieces of 3 ½" thickness pressure resistant marine foam (identical to material used in the composite girder) were cut to track the hull shape using dimensions derived from clearance estimates between the outer hull fairing, lift harness, and pressure spheres. The four forward-most pieces were then bonded together and coated with an epoxy to improve durability, whereas the remaining two foam pieces were coated with epoxy and cured separately. The large 4-piece section

provides approximately 15 kg of buoyancy with an additional 2 kg of buoyancy available through the inclusion of each of the small single sections, thereby permitting buoyancy adjustment according to vehicle-payload configuration. This modular system, when combined with the composite girder, provides between 31 and 35 kg of gross vehicle buoyancy when deployed in freshwater.

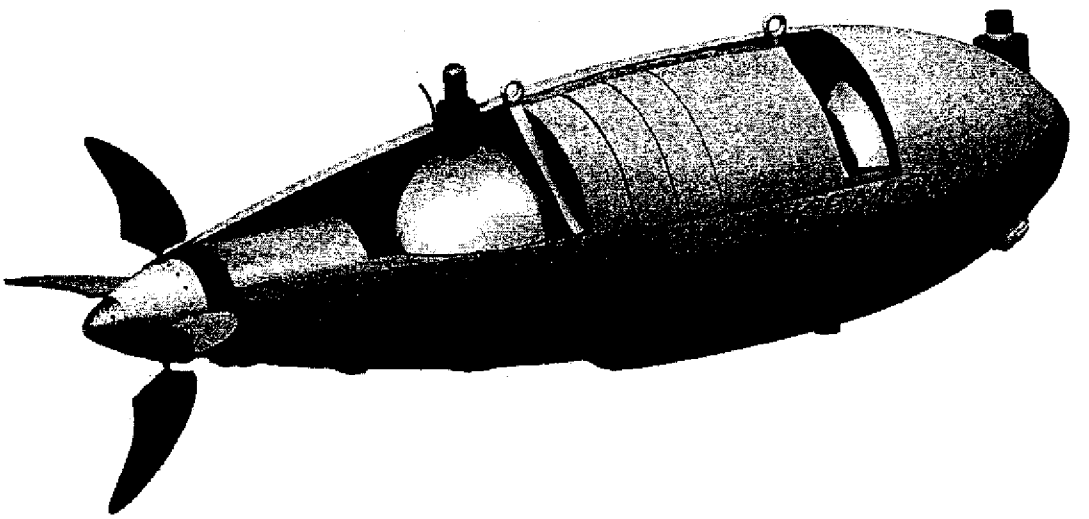

Figure 4-5: Cut-away view of Kemonaut, exposing upper floatation foam and lift harness

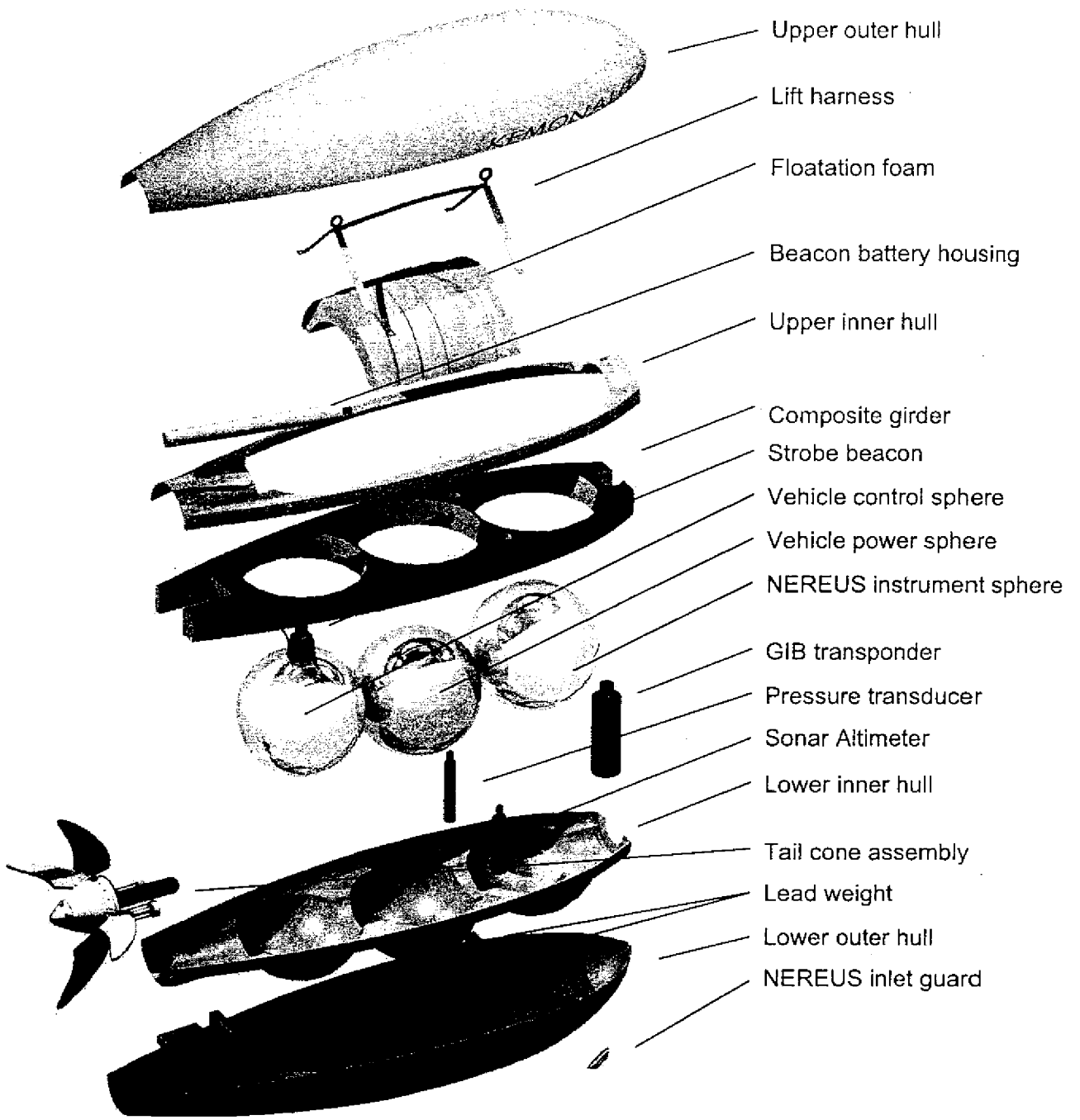

Figure 4-6: Exploded diagram of Kemonaut vehicle components

4.3.2 Control and navigation

Vehicle control was made possible using the Odyssey IId Xanthos tail cone assembly and control sphere. Both components are powered using the central battery sphere which houses a battery pack capable of generating 800 watt-hours of energy. The tail cone assembly includes a propulsion unit powered by a 100 watt Pittman ELCOM series 5100 brushless thruster enclosed within a cylindrical metal Benthos pressure housing in concert with an elevator and rudder subassembly composed of two oil compensated Pittman 3100 actuators individually directed by JR Kerr motor controllers using Hall effect feedback sensors [88].

Navigation is carried out through a simple open-loop system, using a global positioning system and CrossBow AHRS (altitude, heading and reference system composed of a 3-axis accelerometer and magnetometer) contained within the control sphere, along with a Data Sonics PSA-916 sonar altimeter and Paroscientific Digiquartz pressure sensor[88]. Data from these sensors are supplied to the main vehicle computer (MVC), a 300 MHz PC-104 stack, which uses MIT Sea Grant's Mission Oriented Operating System (MOOS) and is located within the aft control sphere. A FreeWave spread spectrum radio modem housed in the aft sphere supplies communication between the MVC and base station. This basic configuration allows the vehicle to obtain position fixes and mission updates by way of the radio transmitter and onboard GPS when the vehicle is surfaced. While submerged, the MVC executes mission directives using dead reckoning estimates via the AHRS, altimeter and pressure transducer. The MVC automatically logs time stamped MOOS data during both surface and submerged operation, permitting post-mission analysis of vehicle operations and time synchronized integration of vehicle track log data with NEREUS chemical data.

4.3.3 Assembly

After fabrication was complete, the new 3-sphere inner structural hull was fastened to the outer hull using stainless steel screws. The tail cone assembly was then fitted to the external hull, using a laser to align the thruster axis with the vehicle centerline, and held in place with radially bored stainless steel screws. Next the sonar altimeter and pressure transducer were mounted in the lower hull with hose clamps banding their housings to

stainless steel L-brackets that are in turn bolted to the inner hull. Desiccant packs were added to the pressure spheres before sealing to prevent temperature-induced condensation on internal electronic surfaces, then evacuated to approximately 0.8 atmospheres and placed within their appropriate inner hull cradles. A small hull cutaway was made in starboard bow to accommodate the NEREUS instrument's sampling inlet and a low-cost engine coolant water intake guard was then bolted in place over the cutaway to act as a guard for the sampling inlet. Electrical wiring residing outside of the pressure spheres was connected using waterproof wet pluggable MIL-9 and coaxial cables. The composite girder was then positioned on top of the lower inner hull, followed by the upper inner hull, floatation foam and lift harness, in respective order. These components were then secured in place by eight stainless steel bolts, placed vertically along the perimeter, with the four central bolts attaching to the lift harness legs for load transfer, buttressed by two pairs of bolts fore and aft to prevent hull separation. The top outer hull was positioned and secured along its edge using Zeus fasteners once all components were in place. Finally, several small holes were drilled in the hull underbelly to permit adequate water drainage during vehicle recovery.

Figure 4-7: Positioning of the NEREUS instrument within the Kemonaut forward payload bay

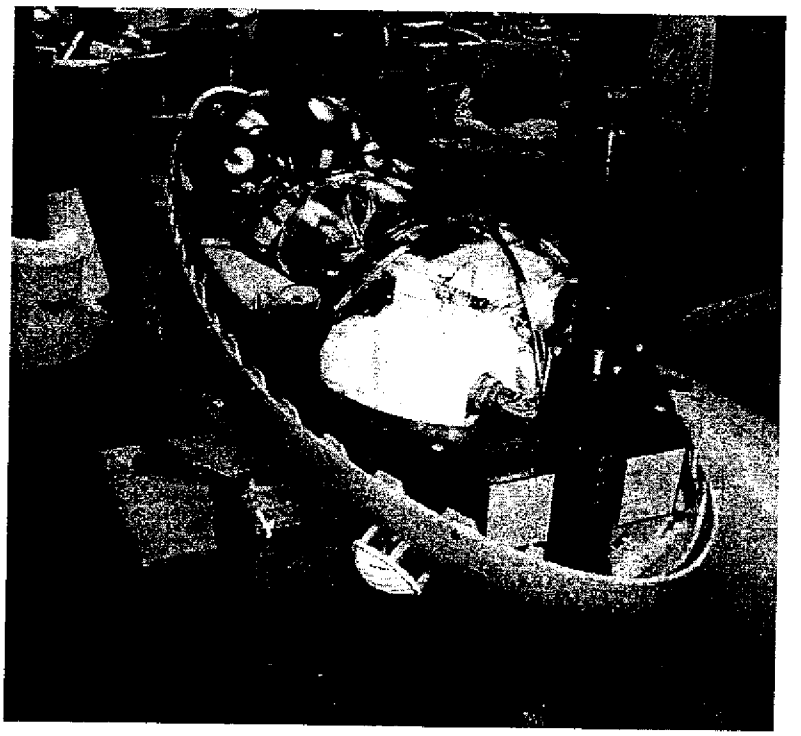

Figure 4-8: Partially assembled Kemonaut, showing the NEREUS instrument and composite girder

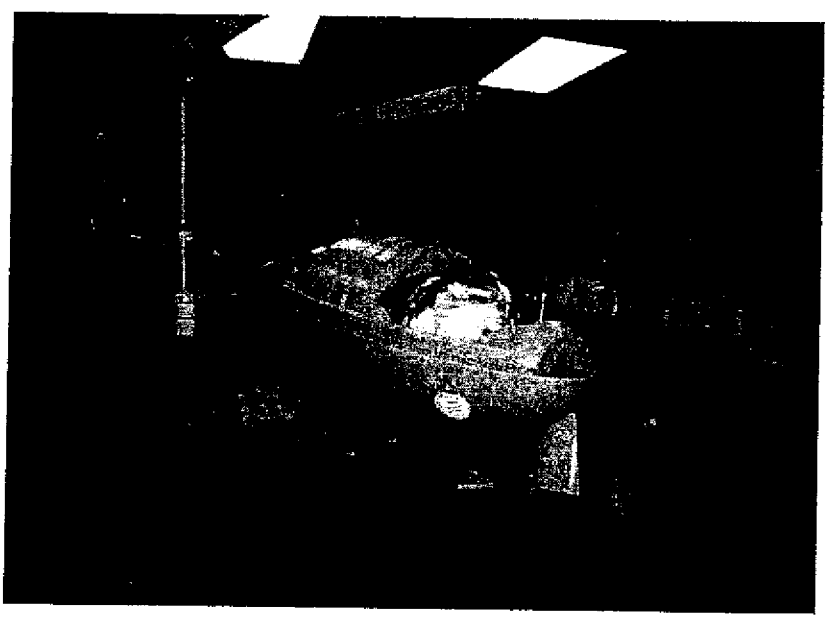

Figure 4-9: Structural integrity test of fully laden Kemonaut vehicle

4.3.4 Stability and ballasting

Prediction of Kemonaut's displacement and ballasting requirements were made prior to construction using computer-generated models of the assembled vehicle. The overall vehicle was calculated to have a mass of nearly 185 kg and displace some 0.196 m^3 volume, thus yielding a net buoyancy of about 15 kg in freshwater by assigning appropriate material density characteristics to individual Kemonaut components. Modeling and calculations also indicated that proper trim could be achieved by placing 10 kg of lead weight in the aft portion of inner hull immediately in front of the tail cone assembly, along with approximately 4 kg of lead below the forward sphere. Thus, producing a net 1 kg positive buoyancy in freshwater with a center of mass located approximately 6 cm below the center of buoyancy.

Initial ballasting was carried out on December 10, 2002 in the Upper Mystic Lake after the vehicle had been assembled. At this time the lake surface had frozen to a thickness of several centimeters, requiring that a hole be made in the ice for ballasting. Using the Mystic Boat Club's facilities, the vehicle was lowered by electric hoist into the water to observe static buoyancy. Lead weight was then added iteratively until the vehicle established approximately 1 kg positive buoyancy and relatively neutral trim. A total of 15.4 kg of lead weight was added to the vehicle, with 8.8 kg (two 10 lb lead dive weights) placed immediately forward of the tail cone, 4.4 kg (one 10 lb dive weight) between the forward and middle inner hull cradles, and two 0.9kg (2 lb dive weights) on the port and starboard beam each. Based on this ballasting, the vehicle was calculated to need between 3.6 and 5.4 kg of additional ballast weigh for marine deployment.

Kemonaut was ballast tested prior to marine deployment in Boston Harbor from a two-ton electric hoist. Based on results from earlier freshwater ballasting, an additional 3.8 kg of weight was pre-fitted to the vehicle while undergoing assembly in the lab. This additional weight was distributed in two equally weighted 1.8 kg bags of lead shot. The first bag was zip-tie wrapped to the 10 lb dive weight in the nose of the vehicle, and the second weight was wired tightly to the external aft surface of the vehicle, directly below the two 10 lb dive weights, using 4 corrosive links. These corrosive links cause the ballast weight to be jettisoned after a period of 12 hours, thereby improving the prospects of successful recovery in the event of a vehicle system failure. Although theoretically

buoyant for seawater, the vehicle proved to be correctly ballasted without any additional weight. Salinity tests confirmed the harbor water to be slightly brackish at 26-28 parts per thousand, thus helping to account for the density disparity. A small ~300 cc piece of floatation foam was added inside the bow of the vehicle to achieve neutral trim.

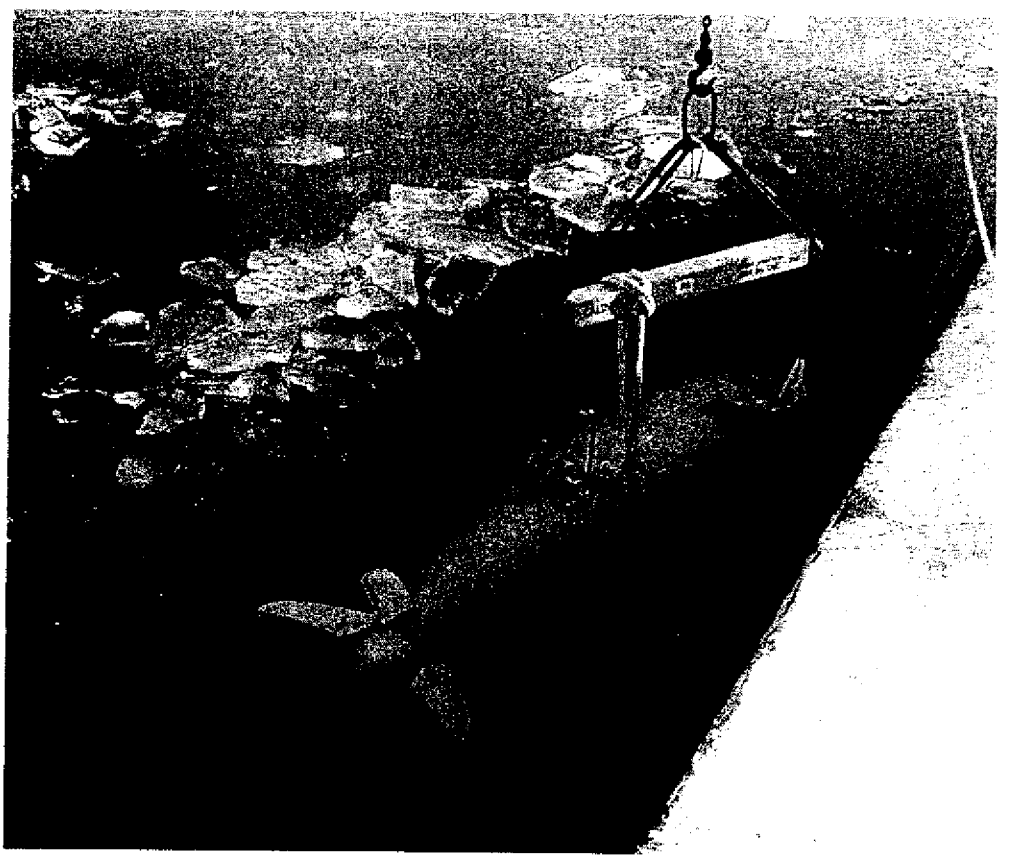

Figure 4-10: Kemonaut ballasting in Upper Mystic Lake

Chapter 5

NEREUS BENCH TESTING

Testing of the NEREUS instrument commenced following fabrication and assembly of the instrument frame, emission regulator, scan controller, analyzer magnet, vacuum envelope, cycloid and ion pump components. The electrometer and computer operated scan controller and data acquisition system were omitted during initial testing, in favor of a simple 10-turn potentiometer controller and commercially available Keithley electrometer (Figure 5-1). Although these two components are comparatively cumbersome, in that they are large and require hand tuning, they permit straightforward assessment of the NEREUS cycloid and ion system elements. The NEREUS instrument recorded its first spectrum on January 8, 2002, using the previously mentioned Keithley electrometer to measure ion current and manually operated potentiometer to scan across the instrument's M/Z range. The initial spectrum, which took approximately 5 hours to manually scan, clearly indicated the presence of water, nitrogen, oxygen and argon peaks (Figure 5-2); thereby demonstrating operation of the various fabricated NEREUS components and overall system design.

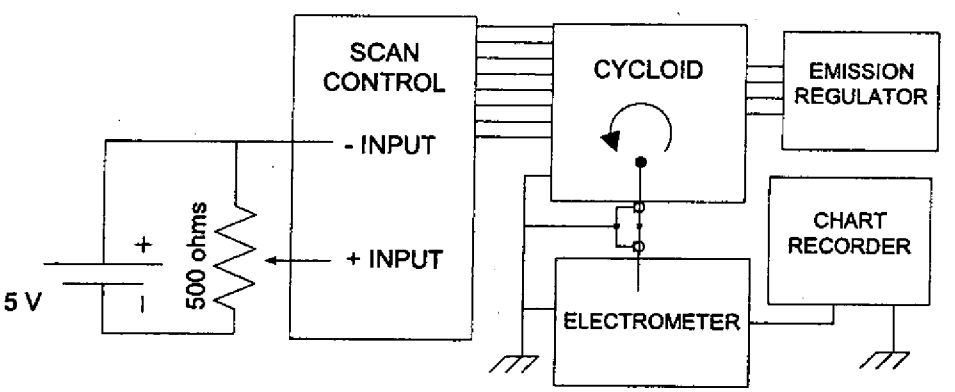

Figure 5-1: NEREUS setup using Keithley electrometer and 10-turn potentiometer

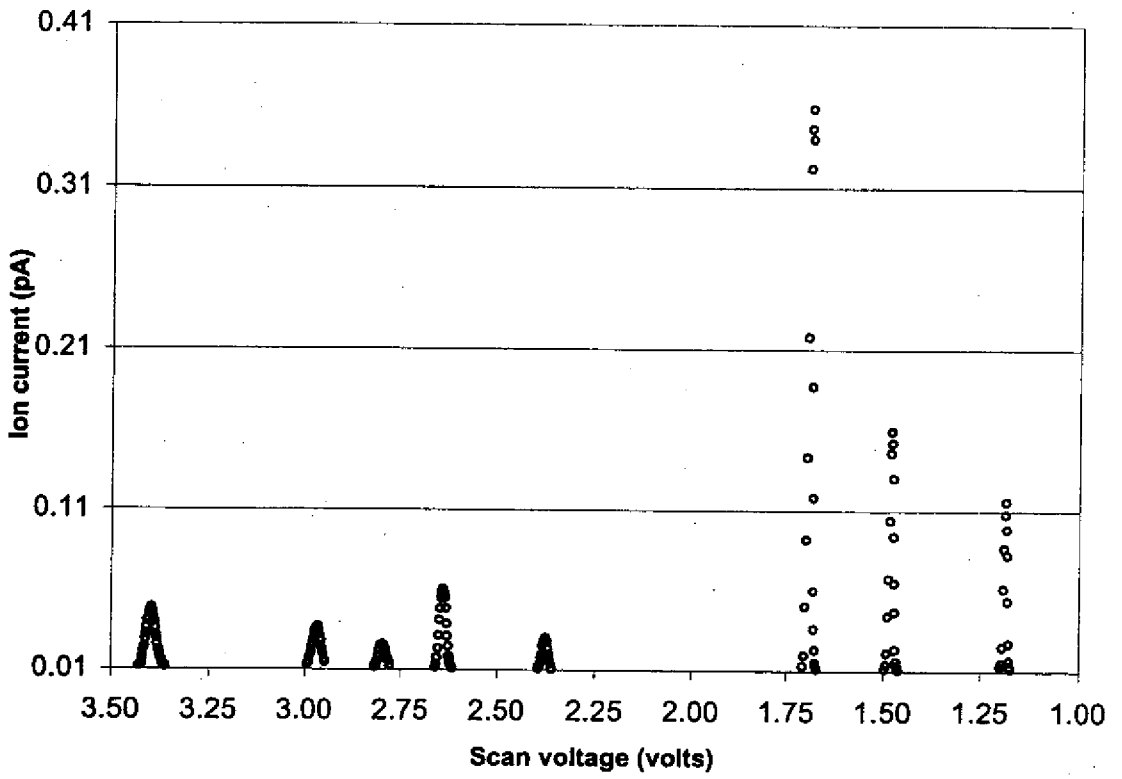

Figure 5-2: First NEREUS scan completed on January 8, 2002, showing ambient air spectrum containing water, nitrogen, oxygen, and argon peaks.

Scans were carried out by varying the potentiometer output from –3.5 to 0 volts, developing cycloid plate electrical field potentials to focus ion beams ranging from 12 to 150 M/Z. (Table 5-1) Repeated scanning revealed that capacitive coupling of the Faraday cup caused cycloid plate voltage tuning to produce a baseline transient in the ion signal output. The 180° Faraday cup detector, which extends to the conflat flange pick-ups in parallel to the cycloid Faraday cup, was shorted to the vacuum envelope, effectively creating ground plane shield to decrease this response delay. Following this modification, the Keithley electrometer was also replaced with an electrometer and shield designed specifically for the NEREUS instrument (see section 2.3.6). This Faraday cup and electrometer assembly greatly reduced the required scan time as well as noise, while generating adequate amplification to permit signal output to be routed to a paper chart recorder (Figure 5-3). Chart recordings indicated that the electrometer, which used a 10^{10}

Ω feedback resistor, yielded approximately 35 mV of noise while generating maximum peak heights in the range of 100-200 mV, suggesting that the electrometer's coaxial compensator attenuated its overall gain by approximately a factor of 10. Therefore, to more closely match the ±5V dynamic range of the data acquisition system and to improve signal-to-noise characteristics, the 10^{10} Ω feedback resistor was replaced with a 10^{11} Ω feedback resistor. This modification generated an amplification increase of approximately 10X, while slightly improving overall signal-to-noise characteristics and maintaining an electrometer response time of less than 30 ms.

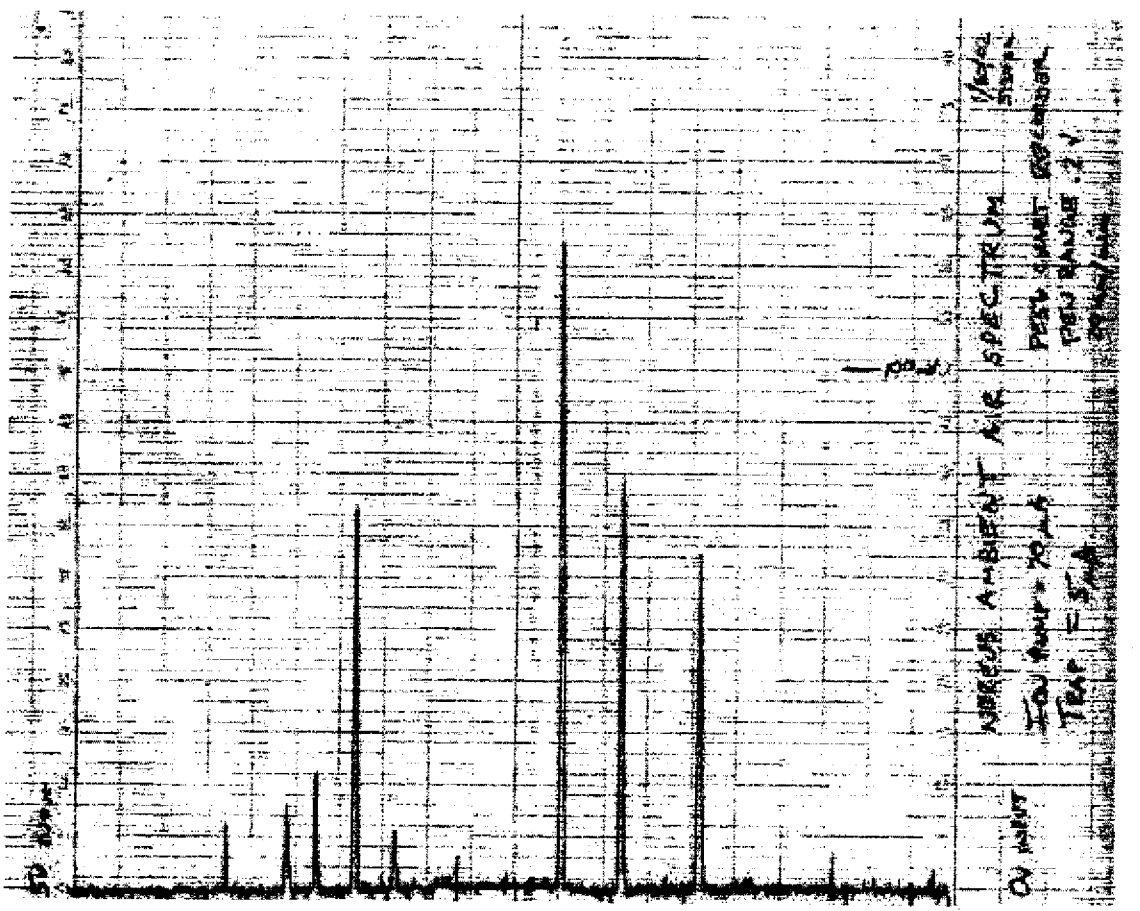

Figure 5-3: NEREUS ambient air spectrum using on board electrometer with 10^{10} Ω feedback resistor

M/z	scan V	m/z	scan V	m/z	scan V	m/z	scan V	m/z	scan V	m/z	scan V
1	47.042	26	1.844	51	0.944	76	0.635	101	0.479	126	0.384
2	23.617	27	1.777	52	0.926	77	0.627	102	0.474	127	0.381
3	15.783	28	1.713	53	0.909	78	0.619	103	0.469	128	0.378
4	11.857	29	1.655	54	0.892	79	0.611	104	0.465	129	0.375
5	9.498	30	1.600	55	0.876	80	0.603	105	0.460	130	0.372
6	7.924	31	1.549	56	0.860	81	0.596	106	0.456	131	0.370
7	6.798	32	1.500	57	0.845	82	0.589	107	0.452	132	0.367
8	5.953	33	1.455	58	0.831	83	0.582	108	0.448	133	0.364
9	5.295	34	1.413	59	0.817	84	0.575	109	0.444	134	0.361
10	4.769	35	1.373	60	0.803	85	0.568	110	0.440	135	0.359
11	4.337	36	1.335	61	0.790	86	0.562	111	0.436	136	0.356
12	3.978	37	1.299	62	0.777	87	0.555	112	0.432	137	0.353
13	3.674	38	1.265	63	0.765	88	0.549	113	0.428	138	0.351
14	3.413	39	1.233	64	0.753	89	0.543	114	0.424	139	0.348
15	3.187	40	1.202	65	0.742	90	0.537	115	0.421	140	0.346
16	2.989	41	1.173	66	0.731	91	0.531	116	0.417	141	0.344
17	2.814	42	1.145	67	0.720	92	0.525	117	0.414	142	0.341
18	2.658	43	1.119	68	0.709	93	0.520	118	0.410	143	0.339
19	2.519	44	1.093	69	0.699	94	0.514	119	0.407	144	0.336
20	2.394	45	1.069	70	0.689	95	0.509	120	0.403	145	0.334
21	2.281	46	1.046	71	0.679	96	0.503	121	0.400	146	0.332
22	2.178	47	1.024	72	0.670	97	0.498	122	0.397	147	0.330
23	2.083	48	1.003	73	0.661	98	0.493	123	0.393	148	0.327
24	1.997	49	0.982	74	0.652	99	0.488	124	0.390	149	0.325
25	1.918	50	0.963	75	0.643	100	0.483	125	0.387	150	0.323

Table 5-1: Approximate scan input potentials (negative voltage) required to focus a given M/Z. Cycloidal scanning below M/Z=11 is not possible because of physical ion focus limitations but out-of-range scan voltages have been included to illustrate the non-linear relationship between M/Z focus and scan voltage.

5.1 Dissolved gas gradient sampling

After successfully demonstrating the ability to generate spectra from air and water samples, a laboratory-synthesized gradient was created to test the instrument's capability to accurately quantify dissolved gas concentrations. This simulated spatial gradient was created by serially diluting an anoxic water sample previously collected in a BOD bottle from the bottom of Mishewam Lake (located in the Aberjona River watershed, north of Boston, Ma.). Analysis was performed by first exposing the membrane inlet to the undiluted anoxic sample, followed by six serial dilutions with aerated mini-Q filtered

water to yield progressively decreasing anoxic water mixtures of: 96%, 84%, 68%, 41%, 24%, 10% and 2%. The resulting data clearly show simultaneous measurement of multiple gas species at useful and representative environmental concentrations (Figure 5-4). The comparatively linear relationship of gas concentration to mixing ratio and correspondence of slope trends at ion peaks of M/Z = 15, 32, and 44 with expected tendencies of methane, oxygen, and carbon dioxide suggest that the NEREUS instrument sensitivity is stable and ion current increases monotonically and fairly linearly with respect to concentration. Although actual gas concentration was not established through independent gas analyses or measurement with known gas standards, the simulated surface water was near atmospheric equilibrium, allowing for estimation of dissolved nitrogen, oxygen, argon, and carbon dioxide concentrations at the various mixing ratios.

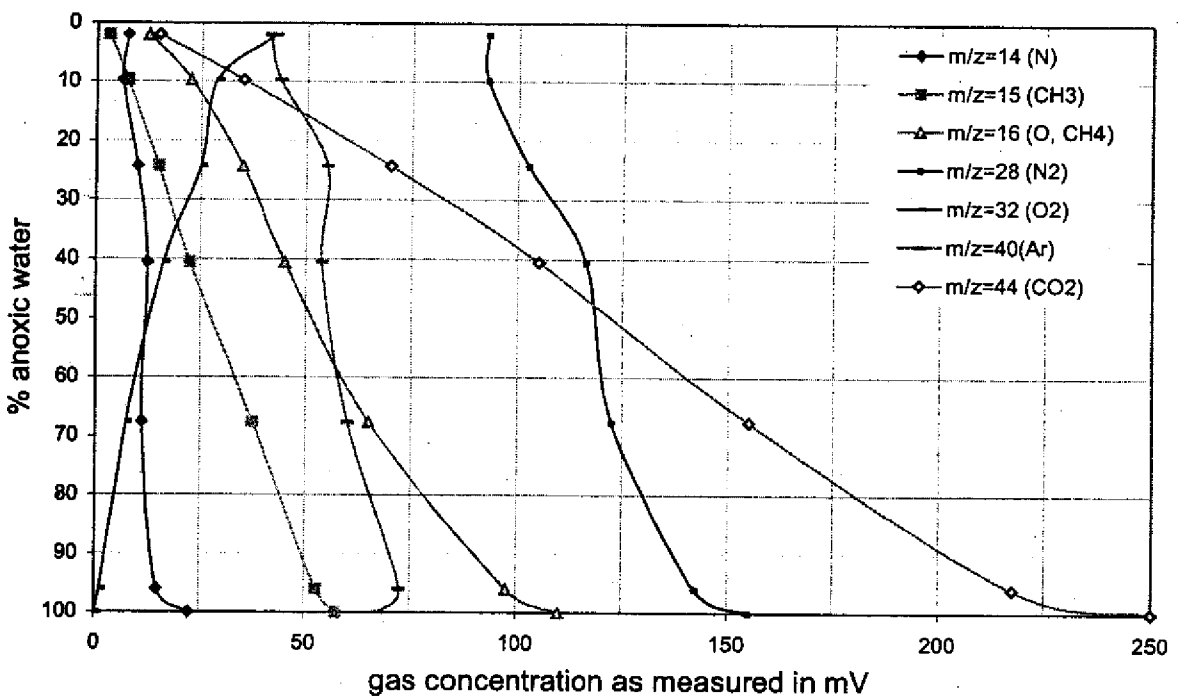

Figure 5-4: Measurements of dissolved gases in a synthesized gradient using Mishawum Lake water.

5.2 Computerized operation and noise analysis

Following testing using the chart recorder and potentiometer, the data acquisition system and computer were integrated into the instrument. The digital-to-analog converter connection to the scan controller required an intermediate isolation amplifier to permit the cycloid's center electric field plate to maintain a "floating" ground potential. Based on electrometer performance calculations and results from manually executed scan rate tests, the embedded computer's execution code was adjusted to employ a 30 ms wait period to ensure adequate time for the electrometer stabilization. Digital ground return paths of the embedded PC-104 computer and DAQ circuitry were isolated from analog electronic ground paths to prevent high speed switching pulses from affecting analog circuit stability, particularly analog-to-digital conversion. Finally, seven differing signal-averaging routines were included as a part of the computerized data collection system in an effort to increase spectrum signal-to-noise ratio.

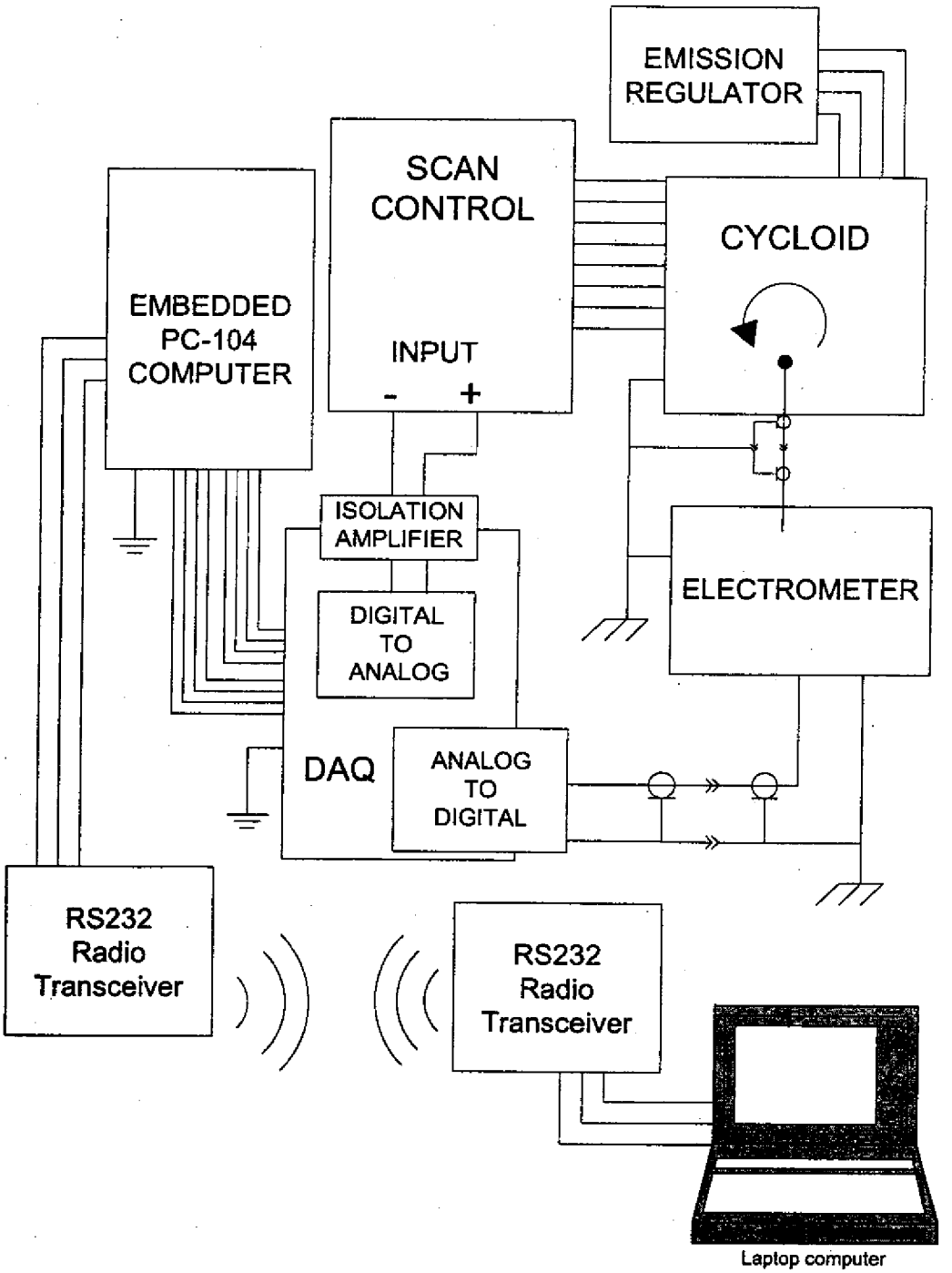

Figure 5-5: Conceptual diagram of NEREUS control and data acquisition design

Spectra generated by this computerized control and data collection system exhibited several characteristic improvements over manually generated data, including: flatter baseline, substantially higher signal-to-noise ratio, better peak shape resolution in higher m/z ranges, and the ability to rapidly tune to a precise m/z value (Figure 5-6).

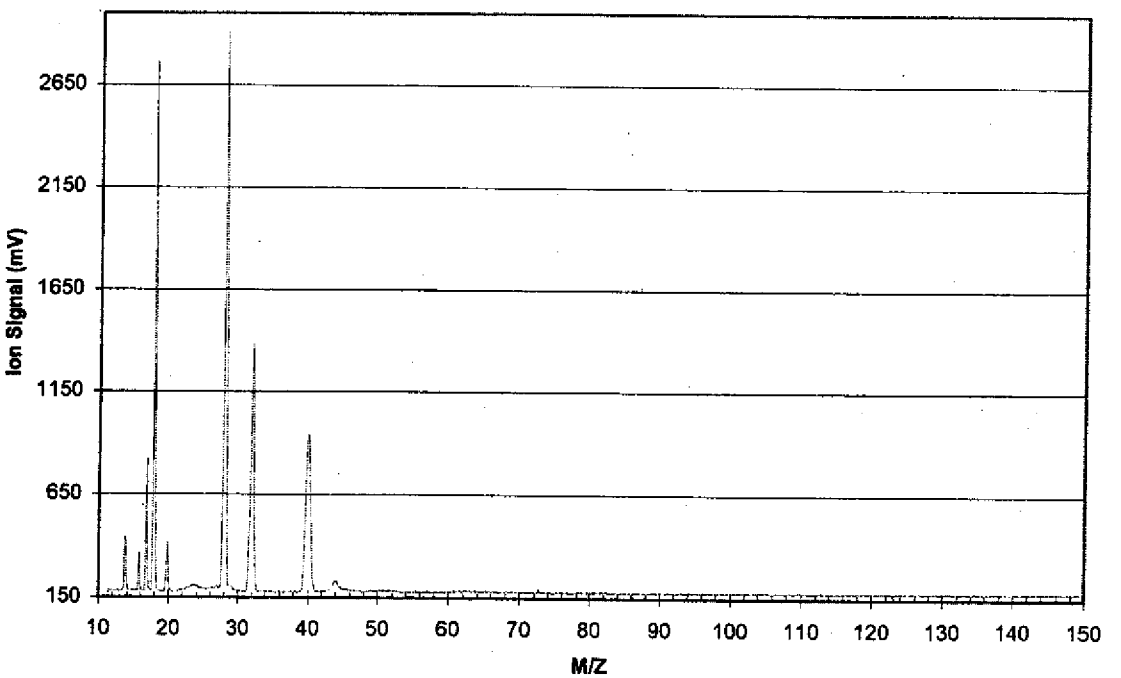

Figure 5-6: Ambient air spectrum, performed using computer control and data acquisition at mass step interval = 0.1 M/Z. This spectrum reveals the presence of nitrogen, oxygen, argon, water vapor, and carbon dioxide.

The signal averaging techniques used by the embedded computer can be broadly grouped into two categories: fixed and variable number signal averaging. Fixed number signal averaging is capable of reducing RMS noise by as much as a factor of 20, but this comes at the expense of instrument speed. The tradeoff of speed versus time requirement is illustrated in Figure 5-8 wherein a 10X increase in sample population generally results in a 3X decrease in RMS noise; closely following the electrometer model predictions for noise. Variable signal averaging was developed in an attempt to decrease instrument sampling time requirements by varying the number of sampling cycles according to integrated signal, thereby generating uniform signal-to-noise ratio throughout the entire scan range and avoiding over-sampling (see section 3.1.5).

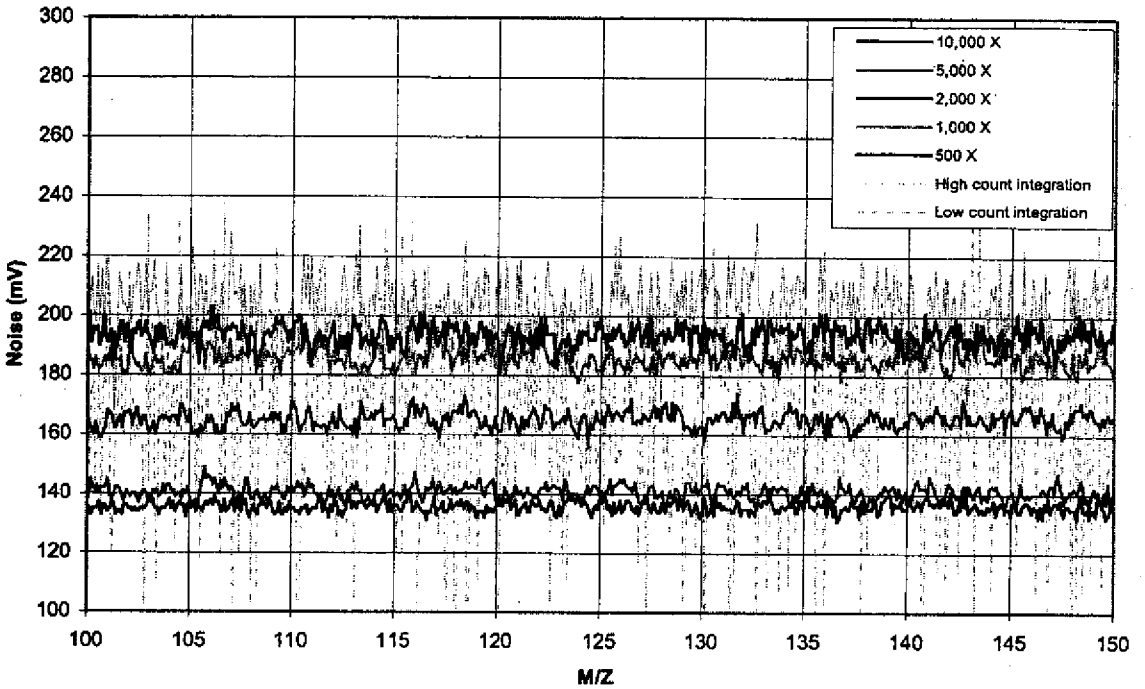

Figure 5-7: Comparison of typical noise characteristics of the NEREUS instrument when operated using differing signal averaging regimes

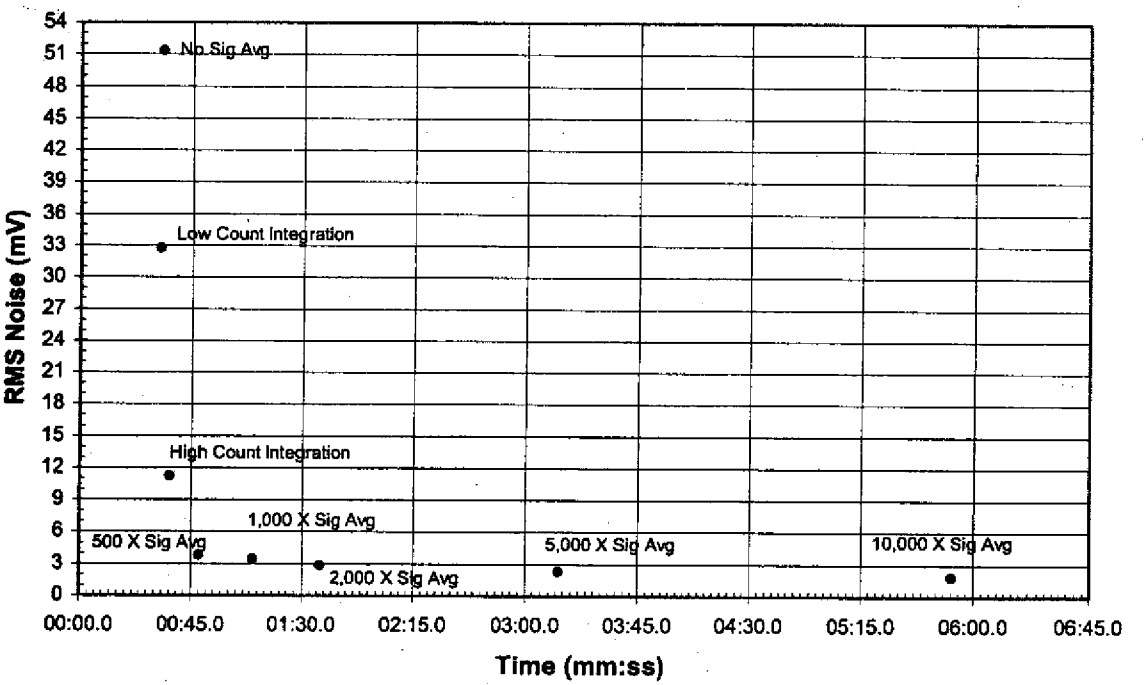

Figure 5-8: RMS noise versus time required for completion of a high resolution, 1385 data point, scan using a 100MHz embedded computer.

These various signal averaging routines enable the NEREUS instrument to exchange scan speed for appropriate levels of accuracy. Based on the results shown in Figure 5-8, a 500X signal averaging routine (residing in the knee of the S/N vs. time curve) appears to be most suitable for quick, moderate resolution, spectrum examinations in that it efficiently minimizes both the required instrument scan time and signal noise. The variable signal averaging routines are most likely to be advantageous in situations where extremely high scanning speed is needed, whereas high count signal averaging can be useful for high-precision analyses such as $^{14}N/^{15}N$, $^{16}O/^{18}O$ isotopic determinations (Figure 5-9).

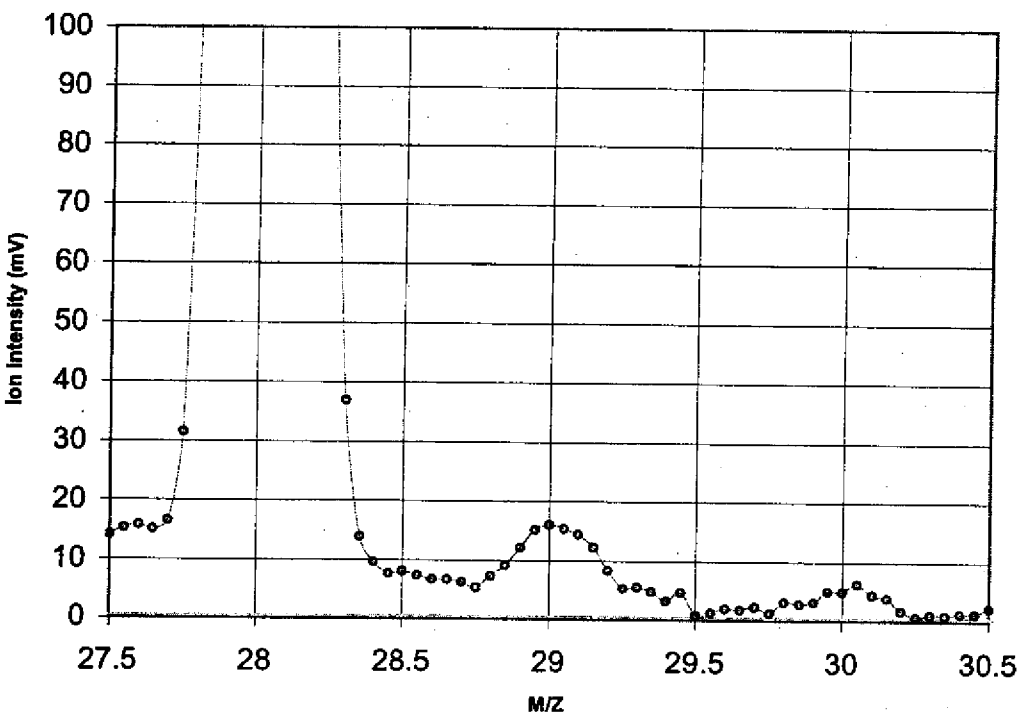

Figure 5-9: A high-resolution spectrum of ambient air, taken using 10,000X signal averaging, detailing nitrogen gas at M/Z = 28 and an apparent ^{14}N-^{15}N isotopic peak at M/Z=29.

5.3 Instrument sensitivity

Based on earlier calculations[39], the analyzer requires a minimum gas influx rate of approximately of approximately 10^{10} gas molecules per second, to generate a detectable

Faraday cup signal of 10^{-14} Amperes. Using this estimate, along with Henrys law constants for various gases, membrane geometry, and permeability constants of these gases across the polyethylene membrane, minimum NEREUS detection limits of individual gas species were projected to range in the tens to hundreds of parts per billion (mass fraction) for most gases [39]. Although this model does not account for variables such as temperature, hydrostatic pressure, variability in ionization efficiency, or fragmentation, sensitivity estimates based on the inlet system's physical characteristics correspond well with observed detection limits of atmospheric gases such as oxygen, argon, nitrogen, and carbon dioxide.

5.4 Ion fragmentation

Fragmentation peaks at M/Z = 20, 17, 16 and 14 can be predicted as functions of their relative intensities, normalized to the intensity of the unfragmented molecular ion. The M/Z = 17 peak is presumed to be a water ion fragment lacking a single hydrogen atom (OH^+), while the M/Z = 16 is presumed to be composed of hydrogen depleted water fragments (O^+), and doubly charged molecular oxygen (O_2^{2+}). Fragmentation peaks at M/Z = 20 and 14 are assumed to be exclusively composed of doubly charged argon and nitrogen, respectively. NEREUS fragmentation data (Table 5-2), with the exception of argon, generally appear in similar ratios[4] to those specified in the UNMIX algorithm [89].

M/Z ion ratio	UNMIX algorithm	NEREUS
Argon 20/40	13%	27%
Nitrogen 14/28	14%	10%
Water 17/18	21%	26%
Water 16/18	1%	2%
Oxygen 16/32	9%	10%

Table 5-2: Ion fragmentation ratios

[4] Oxygen ion contribution to the M/Z = 16 peak is calculated assuming a NEREUS water fragmentation ratio that is normalized to the UNMIX ratio.

5.5 Temperature associated peak height variation

Tests were conducted to determine the effects of membrane temperature on instrument sensitivity. Prior modeling of inlet membrane kinetics suggested that decreasing membrane temperature would cause a simultaneous decrease in membrane permeability, resulting in an overall decrease in instrument sensitivity. Testing was carried out by conducting sequential scans while the instrument's membrane inlet was submerged in a beaker of filtered water. The water was first chilled to approximately 1°C and air bubbles were flushed from the surface of the membrane before scanning commenced. Scans were then conducted in direct succession while the water warmed and the water's temperature was recorded. The peak height data was then time correlated with temperature measurements to produce a temperature-ion peak data series for water, nitrogen, oxygen and argon ions. With the exception of argon, data from all gases within the temperature range of 5 to 22 °C reveal a generally exponential relationship between ion sensitivity and membrane temperature. Data taken at temperatures below 5 °C appear to diverge from the exponential trend and appear to plateau to a constant value. The cause of this low temperature trend is unclear, and maybe due to any number of mechanisms, including: 1) the membrane material undergoing a discontinuous change in its permeability, 2) membrane material being at a greater temperature than the sample water, or other analyte influx mechanisms dominating such as: 3) degassing from internal vacuum system surfaces, 4) decreased ion pump pumping efficiency, or 5) vacuum system leaks.

A near exact correlation is visible between the slopes of M/Z = 17 and 18, signifying that M/Z = 17 is an ion fragment (OH^+) of water vapor. In contrast, the ion peaks at M/Z = 16 exhibit a slope more closely following that of M/Z = 32, suggesting that the M/Z = 16 peaks are predominantly composed of doubly charged oxygen gas (O_2^{2+}), not hydrogen depleted water ion fragments (O^+). Peak heights at M/Z = 40 appear to exhibit a trend of increasing amplitude as a function of increasing temperature, which is the inverse of all other M/Z peaks. This irregularity is likely caused by decreased ion pumping efficiency at lower temperatures and may be further intensified due to the fact

that argon, a noble gas, is relatively difficult to sequester with the diode-type pump used by NEREUS (see section 5.6).

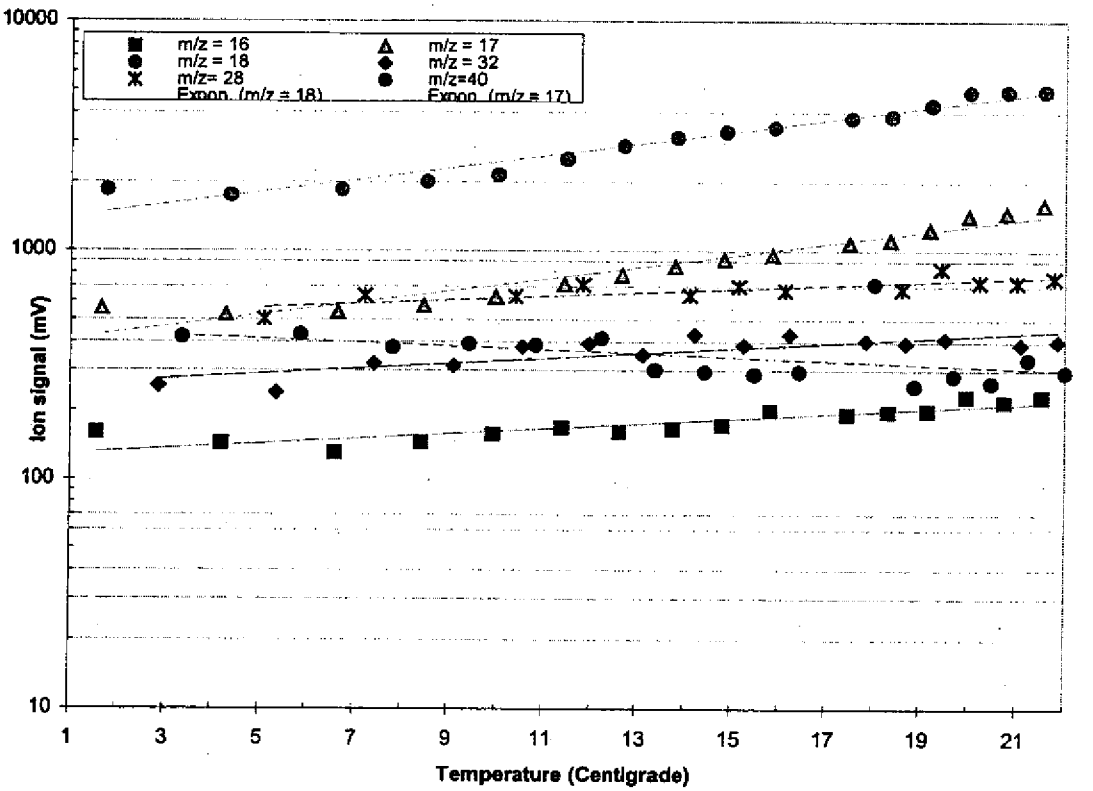

Figure 5-10: \Ion peak height of dissolved gases in atmospheric equilibrium as a function of temperature

Theoretically, the membrane permeability of these gases should change as an exponential function of temperature, where permeability equals the pre-exponential permeability constant multiplied by the negative exponent of the activation energy of permeation divided by the Boltzmann constant multiplied with the absolute temperature of the membrane (Equation 5-1) [90]. This relationship can be augmented with temperature dependent Henry's Law gas solubility constants [91] to model expected sensitivity variation across a temperature range.

$$P = P_0 \times e^{-E_p/RT}$$

Equation 5-1: Membrane permeability as a function of temperature

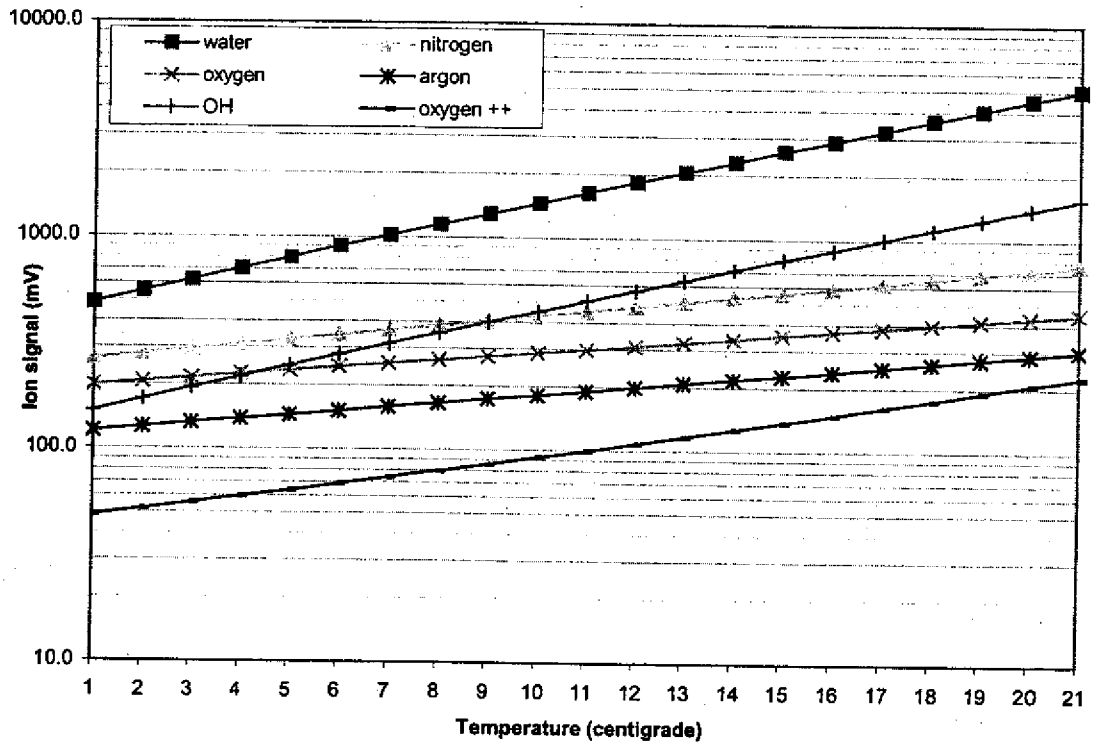

Figure 5-11: Model of NEREUS ion peak height sensitivity as a function of temperature (i.e. with respect to membrane energy of activation and Henry's Law solubilities in freshwater). Data points are normalized to NEREUS spectrum data from filtered water at 22°C.

Model data derived using these parameters for water vapor, nitrogen and oxygen demonstrate exponential trends similar to measured data trends (Figure 5-11). Although, model calculations suggest a more precipitous decrease in permeability as the membrane's temperature decreases than the experimental data, the slope ratios of these gases (i.e. model slope ratios compared with measured slope ratios) exhibit a closer degree of congruence.

5.5.1 Temperature dependent detection limits

The temperature dependent permeability parameters may also be coupled to previously modeled expected instrument detection limits [39] to yield dissolved gas detection limits of the instrument at varying temperatures. This model, which takes into

account the membrane thickness, surface area, permeability of the membrane to a gas, and the equivalent partial pressure of dissolved gas to determine a volumetric flux rate of the analyte gas, assumes that the analyzer requires a minimum gas influx rate of approximately 10^{-12} grams of argon per second, or approximately $10^{10.2}$ gas molecules per second, to generate a detectable Faraday cup signal. Using this model, minimum NEREUS detection limits of individual gas species can be estimated. By applying the ideal gas equation, the measured molecule flux rate can be expressed in terms of a volumetric flux rate at standard temperature and pressure. Volumetric flux rate, Q (cm^3 @STP/sec), can then be used to find the equivalent partial pressure, p_1 (atm), of the gas encountered on the external surface of the membrane (Equation 5-2) [92].

$$Q = \frac{P\,A}{l}(p_1 - p_2)$$

Equation 5-2: Inlet gas flux as a function of membrane geometry, permeability, and gas concentration.

The permeability coefficient, P ([cm^3@STP·cm]/[cm^2·sec·atm]), of the membrane to a given gas is calculated as a function of temperature using Equation 5-1. The membrane surface area, A (cm^2), and thickness, l (cm), are known, and the internal partial pressure of the gas, p_2 (atm), is assumed to be negligible. An estimate of minimum detectable dissolved gas concentration can be calculated from this partial pressure using Henry's law constants.

Temperature dependent detection limits can also be estimated by simply considering the signal-to-noise ratios of ion peaks, while taking into account gas solubility at a given temperature because the concentration of a gas is determined by its Henry's law equilibrium with the atmosphere. Thus, minimum detection limit estimates are calculated by dividing the equilibrated gas concentrations by their ion signal, and then multiplying these terms with the appropriate noise value. Based on overall NEREUS noise characteristics (section 5.2), a minimum noise value of approximately 2.5 mV can be achieved when signal averaging 10,000 times. Although the oxygen and nitrogen ion peaks contained in temperature data appear to be attenuated by a factor of two or more

(dissolved oxygen and nitrogen peaks at room temperature are typically in the vicinity of 1000 and 2000 mV, respectively), order of magnitude estimates from this data indicate that the NEREUS instrument is capable of detecting dissolved oxygen and nitrogen in concentrations as low as 0.1 to 0.01 μl/l.

5.6 Variable ion pump efficiency

During bench testing of the NEREUS instrument it became apparent that the pumping efficiency was variable. Occasionally, sharp increases in ion pump current demand were observed, along with a simultaneous heightening of ion peaks at M/Z = 28, 32 and 40, suggesting that bursts of sequestered gases from the pump's walls were being reemitted. According to the Varian product literature,

> When an ion pump is new or has been regenerated, for example by baking, the surface layer of the cathode is clean and the gas re-emission from it is negligible. In this condition, the ion pump is called 'unsaturated' and the pumping effect is due both to the gettering effect as well as to ion implantation and diffusion. As the number of gas molecules implanted into the cathode increases, the re-emission due to the ion bombardment increases. As a consequence, the net pumping speed decreases until an equilibrium condition between ion implantation and gas re-emission is reached. In this condition, the ion pump is 'saturated' and the net pumping speed (due only to the gettering action of the material sputtered from the cathode) is about half the pumping speed of the unsaturated pump... The main characteristic of noble gases is that they do not react with any other element. Therefore, the film produced by the sputtering of cathode material does not provide getter pumping for helium and argon. Moreover, since these gases do not tend to diffuse into the cathode, the pumping effect due to the ion implantation is not permanent. Nevertheless, all the ion pump elements have some capacity to remove these gases. Noble gases are pumped by being buried by titanium. Noble gas ions can be neutralized and scattered from the

cathode without losing their energy. These neutral atoms maintain enough energy to implant or stick on the anode and on the pump walls where they will be buried by sputtered titanium and thus permanently pumped. In the Diode configuration, the neutralization and back scattering probability is very small, thus the pumping speed for noble gases is only a small percentage of the nitrogen pumping speed. Moreover, when operating at a relatively high argon partial pressure (i.e., higher than 10^{-8} mbar), sudden bursts of pressure due to the re-emission of temporarily implanted argon in the cathode is observed. After this occurs, a Diode pump is not able to pump more argon until its source is stopped. This phenomenon is known as 'argon instability'. [93]

This explanation is consistent with the observed sporadic increases in argon ion peak height, and may also account for the similar behavior encountered with oxygen and nitrogen ion peaks. It is hypothesized that a sudden re-emission burst of argon from the pump may trigger an avalanche of other gases from internal pump surfaces. The scenario is especially likely if the ion pump has been used for an extended period without having undergone regenerative baking-out, thus allowing the gas load buried within the pump walls to build up.

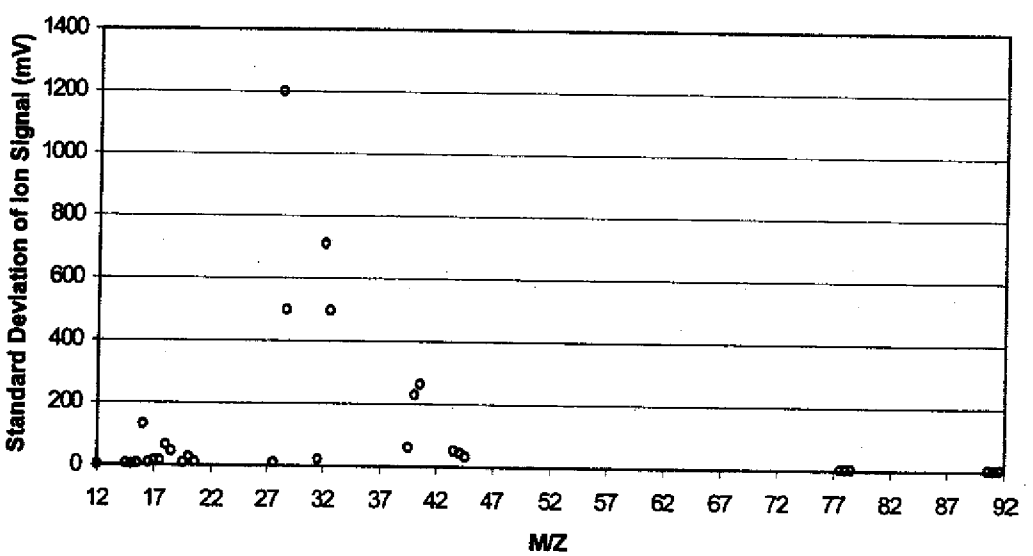

Figure 5-12: NEREUS ion signal variability, recorded while submerged in a flume, based on 9 consecutive spectrum scans executed using a peak jumping algorithm.

Data from 9 consecutive scans within a 7 minute period during submerged testing (section 5.8) of the instrument in a laboratory flume filled with stationary water revealed greatest peak height variability among M/Z = 28, followed by 32 and 40. Although the instrument was submerged in water, peak height variability at M/Z = 18 and 17 was considerably less than 16, and orders of magnitude below that of M/Z = 28, 32 and 40, suggesting that the deviation was unlikely to have been caused be vacuum system leaks or variable ionization. Furthermore, there was no appreciable variability in peak heights at regions near M/Z = 12, 15, 78 and 91, indicating that electrometer drift was not significant. At the time of this test the ion pump had operated for more than 100 hours without bake out, while conducting NEREUS air spectrum analyses. After experiencing similar degassing events during the first tethered NEREUS deployment, this ion pump was replaced prior to its second tethered deployment and recorded comparatively negligible argon and nitrogen signal variation during that deployment.

Based on the observed instrument behavior and ion pump literature, it appears that periodic high-temperature bake out of the ion pump aids not only in extending pump life, but also minimizes background noble gas enrichment and facilitates stabilization of instrument sensitivity. NEREUS ion pump rejuvenation has been successfully completed on several occasions by removing the ion pump housing and heating the pump body to a temperature of approximately 125-150 °C. Once the ion pump body has reached its prescribed temperature, the pump-down inlet valve and vacuum envelope valves are opened and the system is evacuated using an oil diffusion pump in series with a roughing pump. Suitable results have been achieved when this pump down is performed for a period of at least 12 hours. This process requires that the ion pump's high voltage power supply be turned off, and care must be taken not to scorch the instrument's composite frame, nor to surpass the nearby analyzer magnet's Curie temperature.

5.7 Instrument response time

Several factors affect NEREUS response time, including electrometer response time, vacuum system conductance, membrane diffusivity, and diffusivity of gases across the unstirred water boundary layer residing outside of the membrane. However, prior

modeling suggests that NEREUS response time is primarily governed by membrane diffusivity [39].

The time required for gases to cross the membrane into the vacuum system can be predicted based on the diffusivity of a given gas within the membrane and on membrane thickness. Provided that the diffusion coefficient of the gas through the polymer is independent of concentration and constant, Fick's second law of diffusion (Equation 5-3)

$$\frac{\partial C}{\partial t} = -D\left(\frac{\partial^2 C}{\partial X^2}\right)$$

Equation 5-3: Fick's second law of diffusion

can be applied as a one dimensional diffusive transport model to estimate the rate of gas permeation across the membrane as a function of time, as the system approaches equilibrium [94]. If the gas concentration on the external surface is kept constant and gas concentration within the vacuum system is effectively maintained at zero, the cumulative gas flux into the vacuum system per permeable surface area, Q_t, can be determined at any point in time (Equation 5-4).

$$Q_t\left[\text{moles}/\text{cm}^2\right] = \frac{D\left[\text{cm}^2/\text{sec}\right]\cdot C_{ext}\left[\text{moles}/\text{cm}^3\right]}{X[cm]}\left(t[\text{sec}] - \frac{X[cm]^2}{6D\left[\text{cm}^2/\text{sec}\right]}\right)$$

Equation 5-4: Analyte gas influx

As t approaches ∞, a linear relation between Q_t and t develops, yielding a t-axis intercept, often referred to as time lag, L (sec) [95]. This time lag can be expressed in terms of membrane thickness, X (cm), and membrane diffusivity, D (cm^2/sec) (Equation 5-5).

$$L[\text{sec}] = \frac{X[cm]^2}{6D\left[\text{cm}^2/\text{sec}\right]}$$

Equation 5-5: Membrane response time lag

Steady state flow is underestimated by about 4% if a period of approximately three times the time lag is used [96]. Applying this time constant of 3L as an estimate of membrane response time, it is evident that membrane thickness strongly affects response time. Given a 1mil membrane thickness, and the various gas permeabilities of polyethylene, it is anticipated that the instrument is capable of accurately quantifying most atmospheric gases within 10 to 15 seconds. Higher molecular weight gases, including many common hydrocarbons, are predicted to require time frames on the order of minutes before converging upon a steady state value (Figure 5-13).

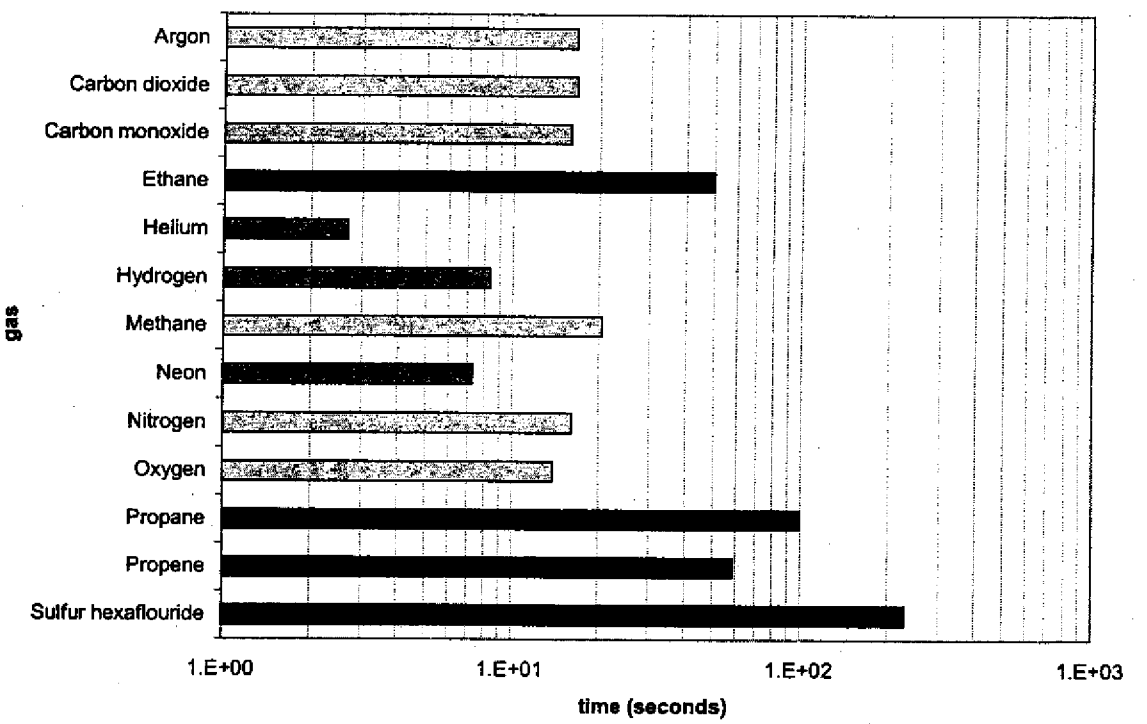

Figure 5-13: Calculated overall NEREUS time to steady state measurement for various gases

Investigations of instrument response time were conducted to corroborate the veracity of these models, using carbon dioxide and benzene. These two gases were chosen based on their low background concentrations in ambient air and expected low quantities of embedded molecules within the ion pump.

Carbon dioxide testing required that the embedded computer be programmed to monitor a single ion peak at M/Z = 44 and record electrometer voltage once per second. The testing was conducted by presenting the membrane inlet with an air sample with a fixed concentration of carbon dioxide. Time was then allowed for the carbon dioxide ion signal to stabilize. After the signal had sufficiently stabilized, the sample was then rapidly evacuated from the inlet using a roughing pump. It is estimated that the membrane inlet was pumped down to a small fraction of 1 atmosphere within less than one second. The data record shown in Figure 5-14 indicates that carbon dioxide ion peak height decreased by 95% within a time period of approximately 15 seconds, a value consistent with the model estimate of 17 seconds. The data also reveals an unexpected ion peak height increase during the initial pump down process. The cause of this transient increase is uncertain, but has been encountered during nitrogen pump down tests using the Hemond backpack portable mass spectrometer with an identical membrane inlet apparatus (Figure 5-15). This phenomenon may be due to the membrane becoming unseated from the backing plate, thereby increasing the total permeable cross section of the membrane and causing a transient intensification of gas flux.

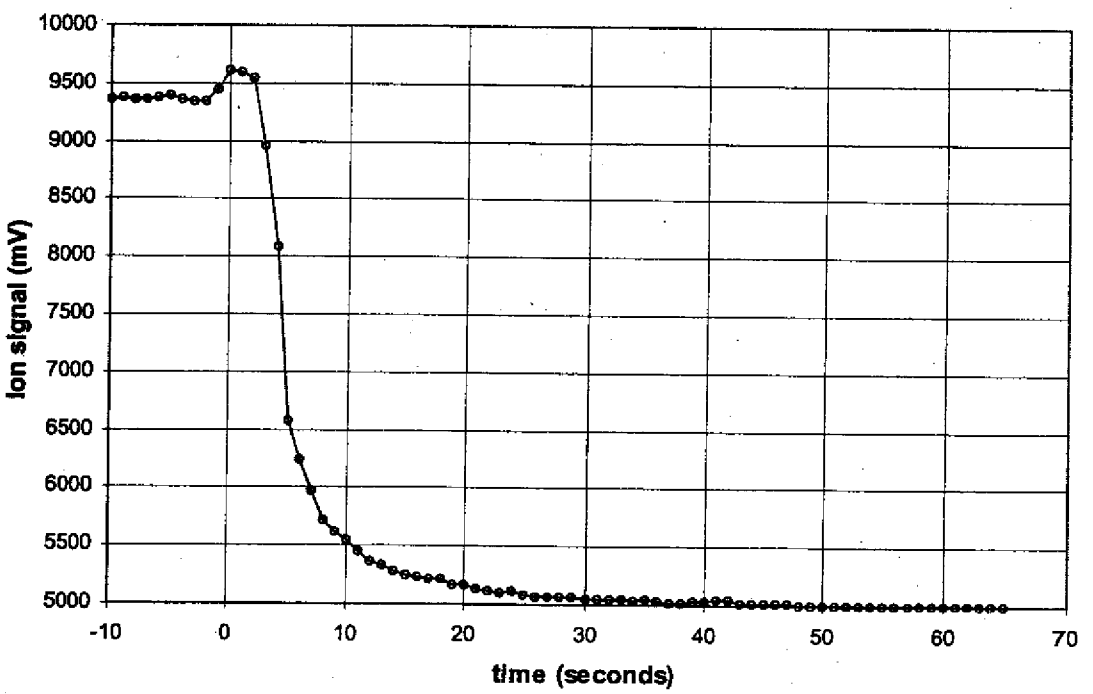

Figure 5-14: NEREUS time response to carbon dioxide

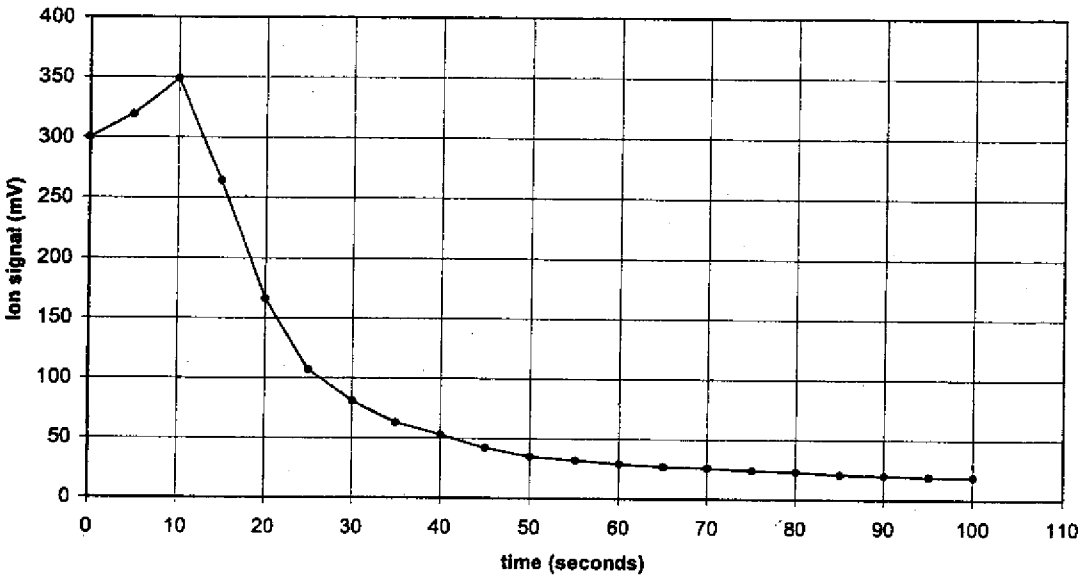

Figure 5-15: Time response of Hemond backpack portable mass spectrometer to nitrogen gas

Although a specific model has not been developed for NEREUS time response to benzene, tests were conducted to assess the overall instrument behavior when monitoring higher molecular weight hydrocarbons. Investigations were carried out by exposing the inlet to a near-instantaneous pulse of toluene rich air and then monitoring the subsequent decrease in the M/Z = 78 ion signal. The resulting curve show in Figure 5-16 indicates that the instrument's overall time response to benzene, assuming a 95% reduction to baseline standard, is on the order of 3 minutes. This value is somewhat faster than model estimates of the lower molecular weight hydrocarbons such as propane, propene and ethane. It remains unclear if this comparatively short response time of the NEREUS instrument to benzene is generally shared with other hydrocarbons, or if it is due to a preferential membrane permeability of aromatic hydrocarbons over aliphatic hydrocarbons.

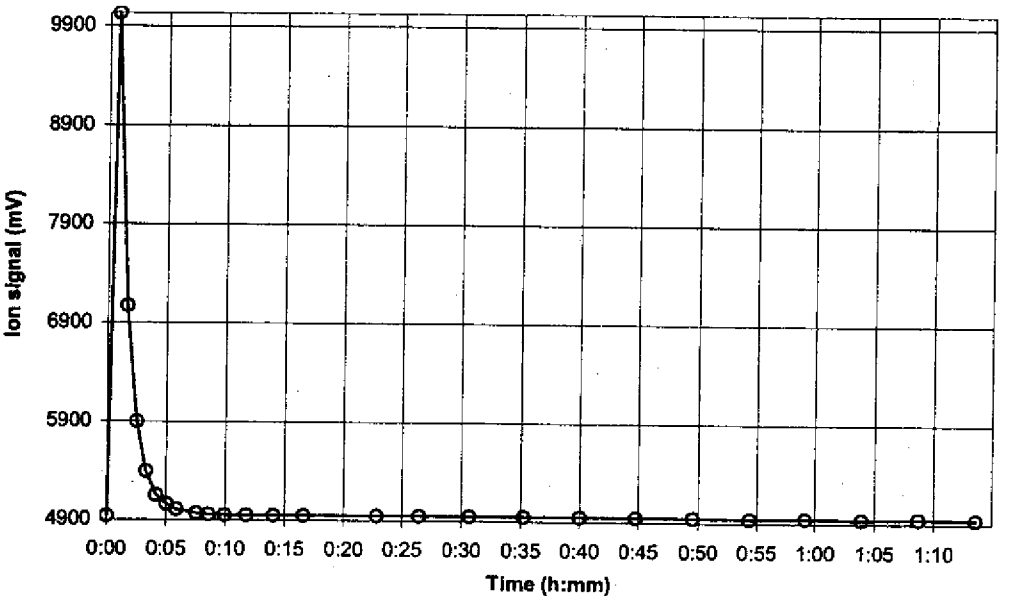

Figure 5-16: NEREUS time response to benzene

5.8 Submerged testing

NEREUS underwent submerged trial operation in a laboratory flume prior to deployment. This trial verified that the glass pressure sphere housing could be properly sealed so that its interior remained dry, that the instrument was approximately neutrally buoyant and maintained a more or less upright position when submerged. Rollover tests also confirmed that the instrument could withstand rapid overturning without damage. Scanning operations were carried out during these tests without any noticeable problems.

Chapter 6

DEPLOYMENT AND SEA TRIALS

Following bench testing of the NEREUS instrument has underwent a number of deployments as a buoyed sensor, towed sensor, and aboard an AUV. Beginning in August 2002, the NEREUS instrument was deployed as a tethered buoy sensor in Halls Brook and Boston Harbor. The instrument was then deployed in the Upper Mystic Lake as a towed body, followed by an AUV deployment in Boston Harbor during December of 2002.

6.1 Tethered deployments

Tethered deployments commenced on August 20, 2002 at the Halls Brook Holding Area (HBHA), a small body of contaminated water located approximately 30 km north of Boston, Massachusetts. This water body, also known as Lake Mishawum, contains high concentrations several types of volatile organic carbons (VOCs) including: benzene, diphenyl sulfone, *ortho*-hydroxybiphenyl, higher hydroxybiphenyls, and alkylated benzenes and are thought to originate from contaminated groundwater inflow to the hypolimnion [97]. In-situ monitoring of VOCs is desirable because substances such as benzene are known to rapidly undergo biodegradation when mixed with the metalimnetic and epilimninetic waters [98].

A vertical profile consisting of six spectra from 12 to 48 AMU was completed during this trial deployment. Each of these scans utilized 500X signal averaging. The deployment was executed by lowering the instrument with a Hydrolab sonde and an attached depressor weight from a rope through the water column to depths of: 0.5, 1, 1.5, 2, 2.5 and 2.7 meters. NEREUS ion peaks were displayed in real time via the radio transceivers and a shore-based laptop computer. Data from the Hydrolab sonde was stored and viewed via a cable connection to its Surveyor 4 logger at the surface.

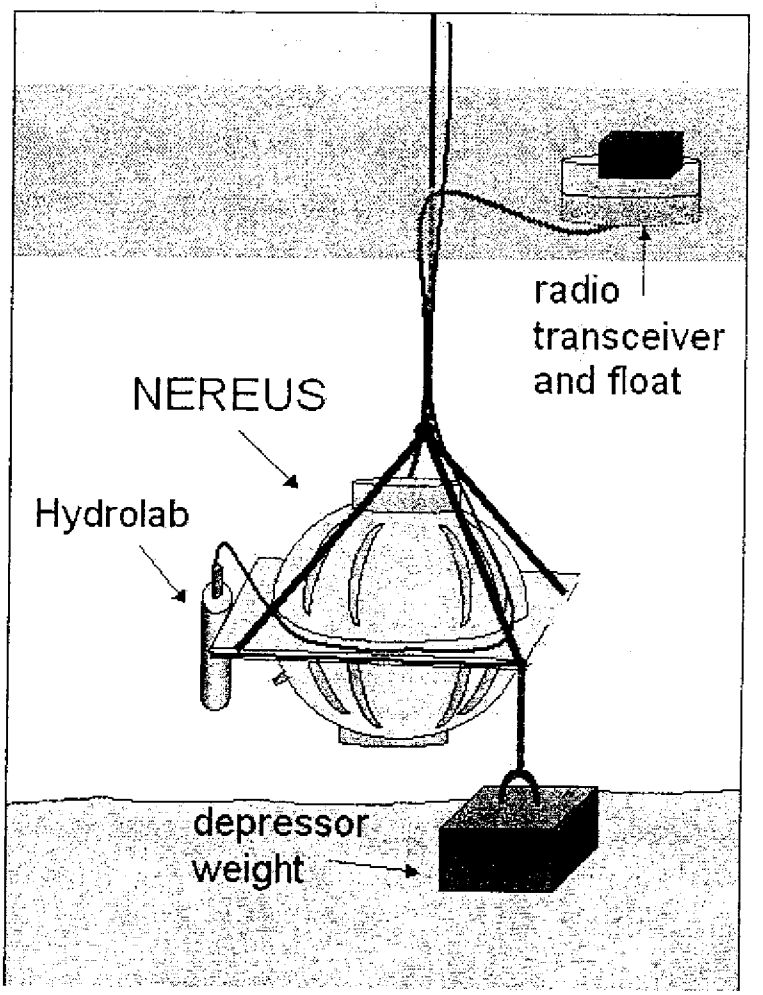

Figure 6-1: Tethered NEREUS configuration with Hydrolab

Data collected during from this deployment reveal the presence of carbon dioxide and methane in the surface water, and concentration increasing with depth, while oxygen concentrations exhibited an inverse trend, decreasing as a function of increased depth. Baseline clipping caused by high C^+ ion fragment peaks at M/Z=12 precludes direct measurement of the ion peak height above baseline (the embedded code normalized the baseline to M/Z=12 values during this deployment). Some ion peak tops such as methane, oxygen and argon (at M/Z= 15, 32 and 40 respectively) were completely concealed by the elevated baseline, while carbon dioxide and nitrogen ion peaks (at M/Z=44 and 28,

respectively) exceed the instrument's dynamic range at depths of 2.5 and 2.7 meters. However, quantitative estimates of the spectra peak heights can be reconstructed by scaling the water vapor peak at M/Z=18 to a uniform value and then adding the spectrum's scaling value to each of the spectrum's peaks. The resulting values suggest factor of three increases in methane and carbon dioxide concentrations at depth. Several peaks appear in M/Z regions that do not correspond to dissolved atmospheric gases, but it is unclear if these are VOC ion fragment peaks or simply artifact. Hydrolab data reveals the presence of a thermocline in the depth vicinity of 1 to 2 meters, coinciding with a similar dissolved oxygen trend, suggesting water stratification. Although the NEREUS spectra RMS noise is less than 5 mV, the oxygen ion peak trend does not correlate well with Hydrolab data, indicating that other sources of error dominate (i.e. baseline clipping).

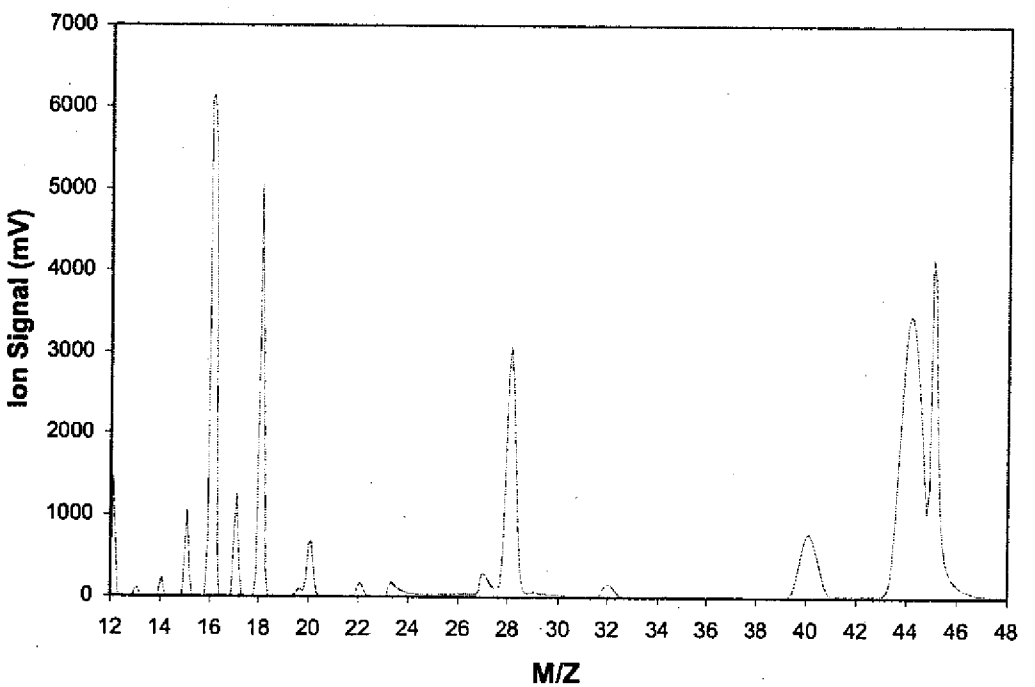

Figure 6-2: NEREUS spectrum from at 2 meters depth in the Halls Brook Holding Area

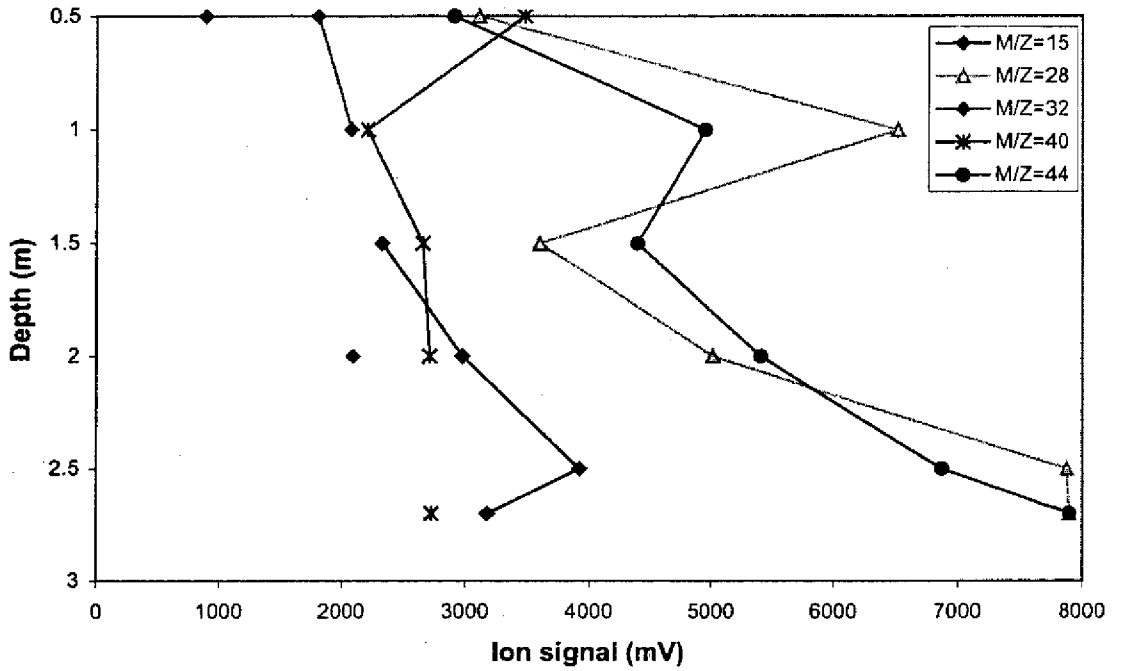

Figure 6-3: NEREUS depth profile of ion peaks in the Halls Brook Holding Area

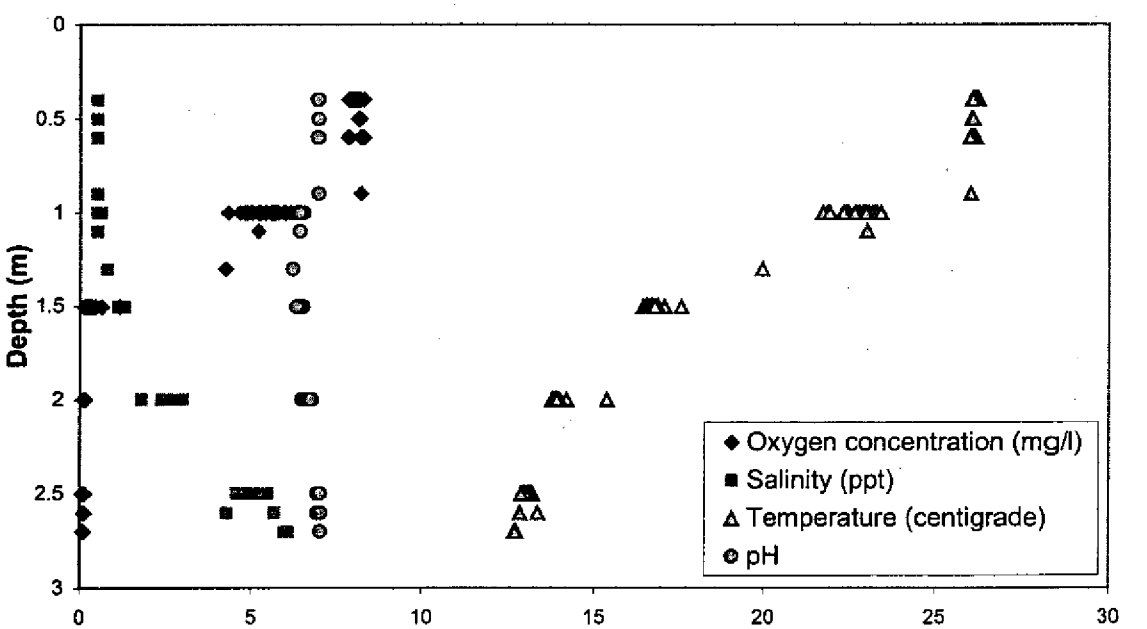

Figure 6-4: Hydrolab depth profile of dissolved oxygen, salinity and temperature in the Halls Brook Holding Area

Following this preliminary Halls Brook deployment, the NEREUS instrument baseline normalization algorithm was modified to use an ion signal at M/Z=11.5 to prevent clipping and a new membrane installed as a safety precaution against membrane failure. After installing the membrane and re-establishing the required vacuum system pressure, the membrane was heated to approximately 50°C with a hot air gun to encourage its conformation to the shape of the backing plate (Figure 6-6).

The August 24, 2002 NEREUS deployment in Boston's Inner Harbor demonstrated the instrument's depth capability, ability to operate in marine environments, and explored for possible pollutants. Over the past decade significant cleanup efforts have been made to clean up the harbor, but several pollution sources still remain such as combined sewer overflows (CSOs), which are known to discharge large quantities of hydrocarbons and trace organics during wet weather [99]. The deployment area, located at North 42 22.234' by West 71 03.419', experiences a diurnal tidal cycle typically of 3.5 meters amplitude and has a mean low-water depth of approximately 9 meters, causing the water to be well mixed. The tether used the same configuration as in the previous deployment, and scans were conducted across a spectral range of 12 to 150 AMU using a 2000X signal averaging routine and were conducted during high tide at depth intervals corresponding to 1.5, 3, 4.5, 6, 7.5, 9, 10.5 and 12 meters without failure.

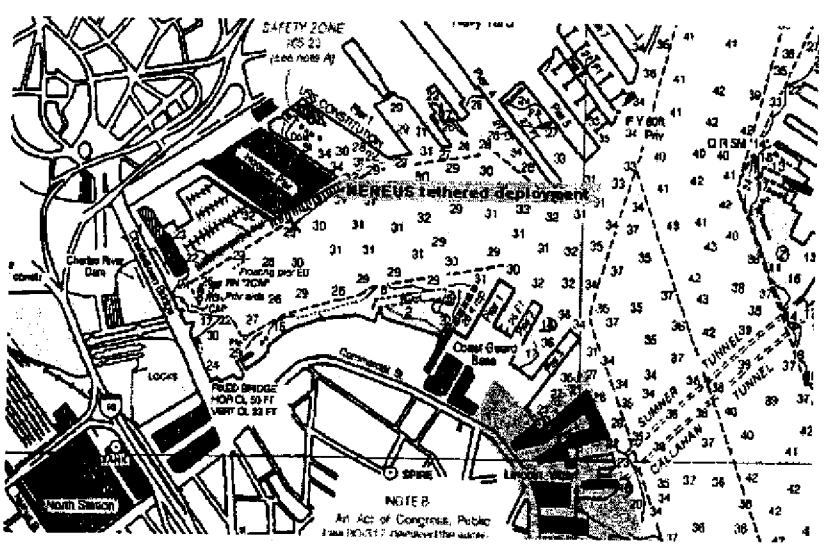

Figure 6-5: Location of tethered NEREUS deployment in Boston Harbor

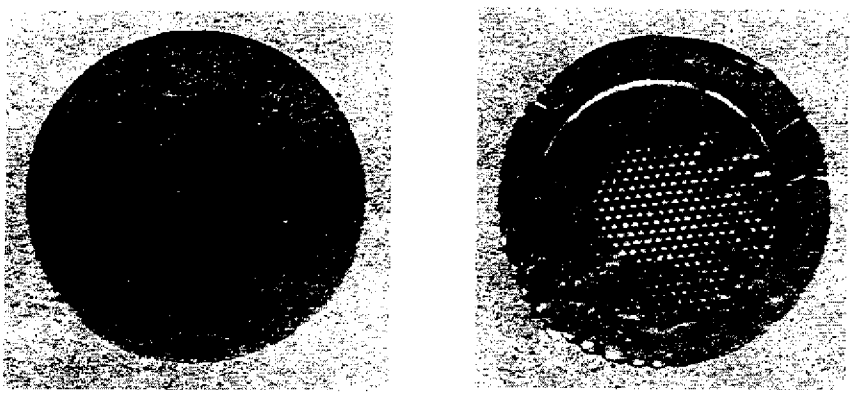

Figure 6-6: Microscopic comparison of a new membrane (left), and after heat forming and deployment to 12 meters depth (right)

The eight spectra generated during this deployment possess similar ion peak signatures and amplitudes, which is suggestive of a well-mixed body of water. All contain noise of approximately 2.5 mV RMS, and have peak amplitudes that are attenuated by around ½, compared with laboratory generated data. Factors contributing to attenuation may include diminished permeable cross section (due to increased membrane adherence to the backing plate), and to a lesser extent, decreased gas solubility in seawater, as well as decreased membrane permeability because of lower water temperature. Typically stable ion peaks such as water vapor, nitrogen, and argon exhibit trends of decreasing amplitude with increasing depth, with an ensemble average variation of 30%. Models of membrane permeability as a function of temperature suggest that the observed water temperature variation of 2.3 °C should affect an 18% variation in these ion peaks. The remaining variation is thought to be due to pressure effects on the membrane, particularly through increased pressure causing the membrane to sag and come into greater contact with the conically shaped holes of the backing plate, thereby decreasing the membrane's total permeable surface area. Permeation may also be effected by molecular-scale decreases in polymer permeability as a result of pressure increases [100], but it is unlikely that these molecular effects come to dominate until much greater depth.

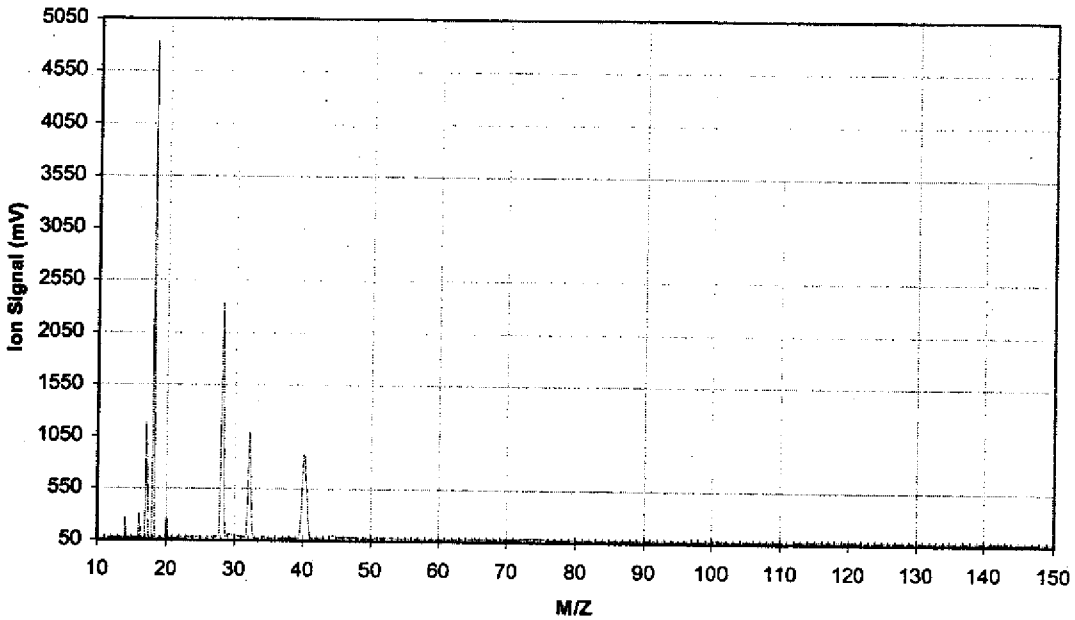

Figure 6-7: Boston Harbor spectrum at 1.5 meters depth

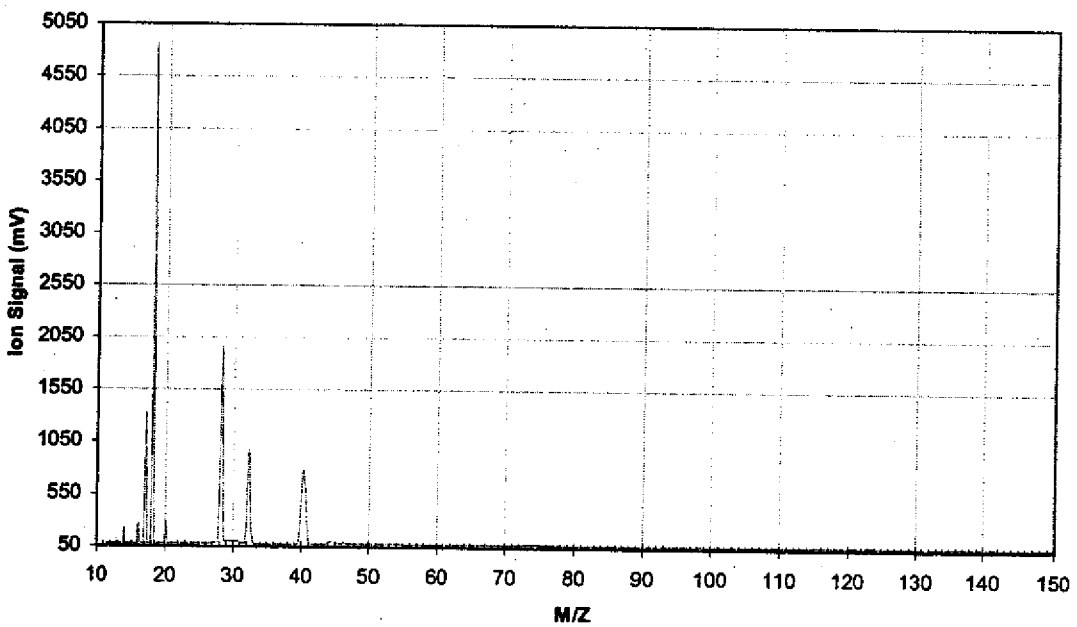

Figure 6-8: Boston Harbor spectrum at 3 meters depth

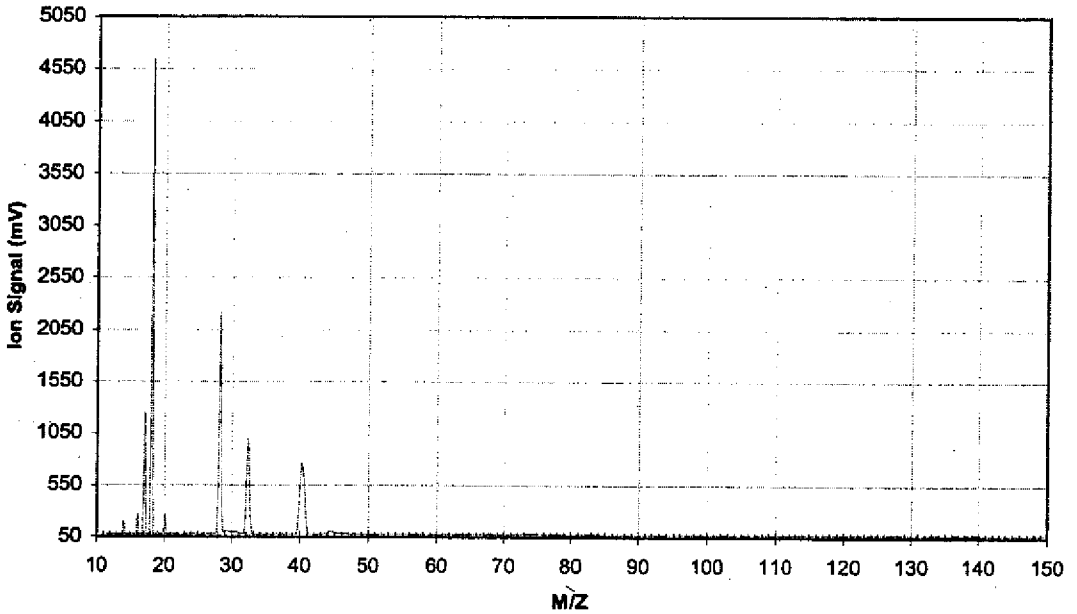

Figure 6-9: Boston Harbor spectrum at 4.5 meters depth

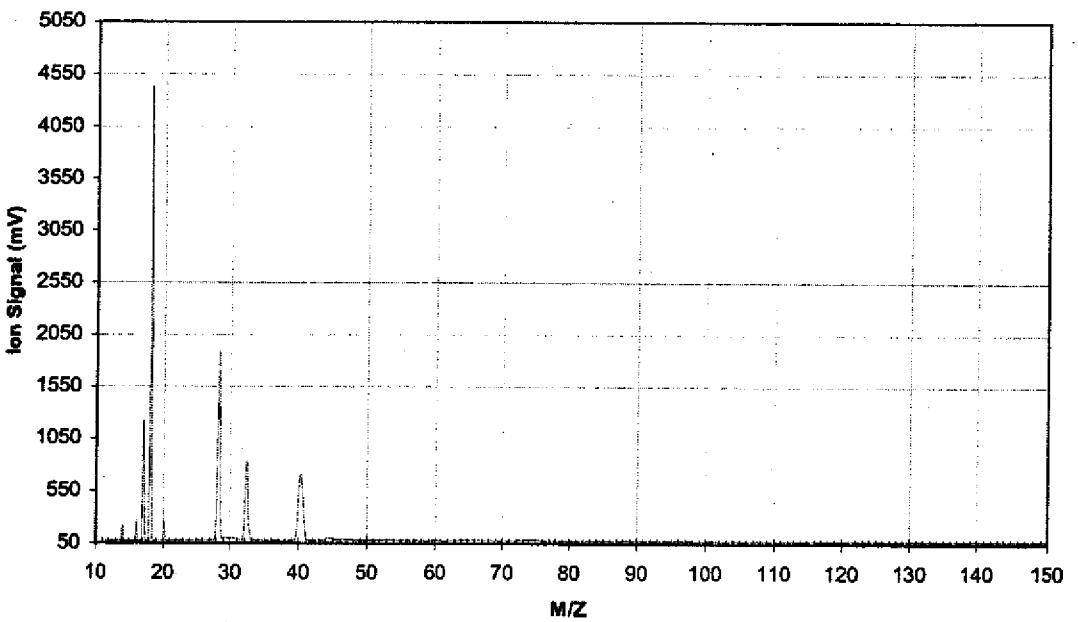

Figure 6-10: Boston Harbor spectrum at 6 meters depth

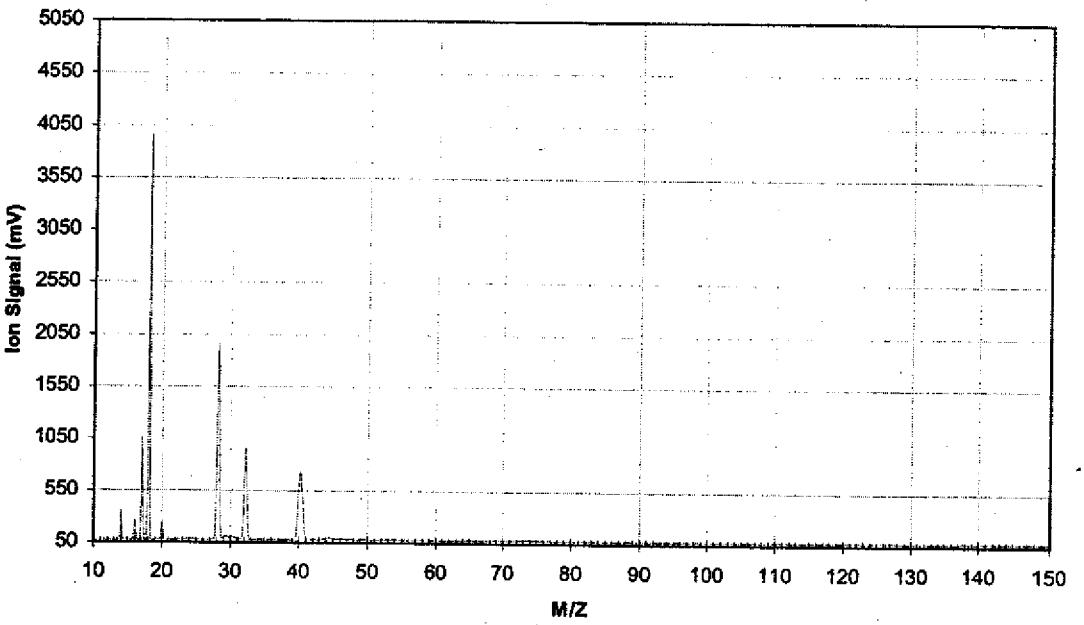

Figure 6-11: Boston Harbor spectrum at 7.5 meters depth

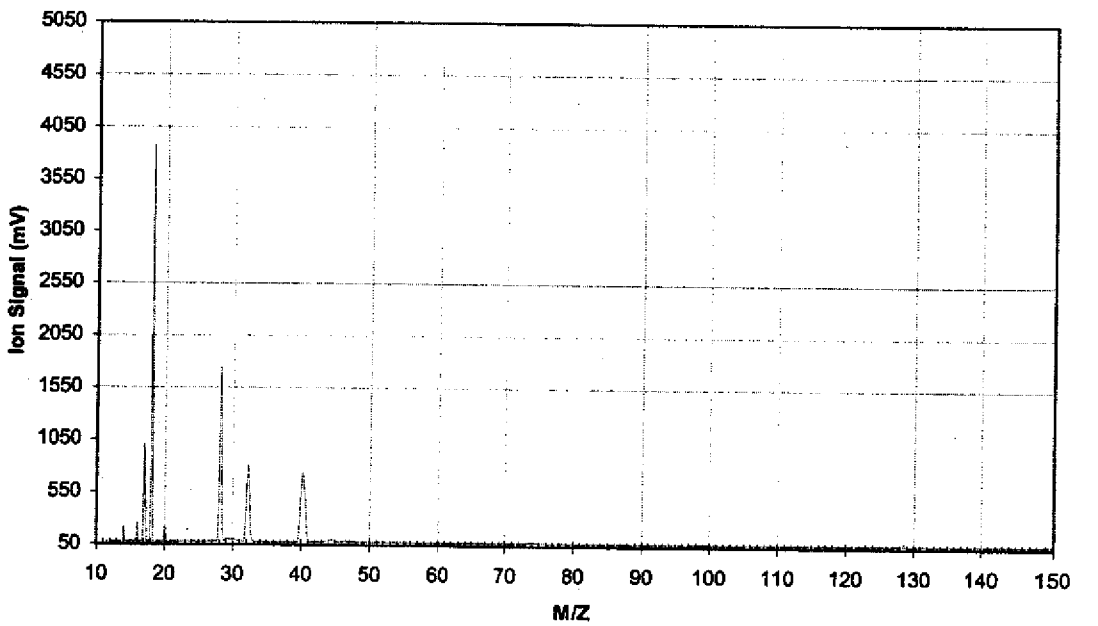

Figure 6-12: Boston Harbor spectrum at 9 meters depth

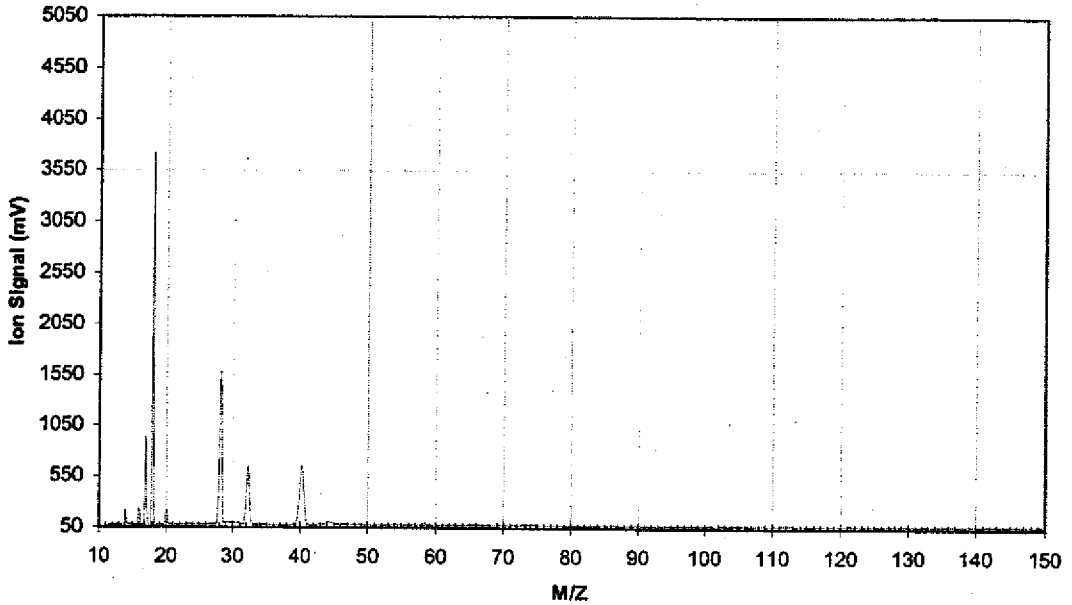

Figure 6-13: Boston Harbor spectrum at 10.5 meters depth

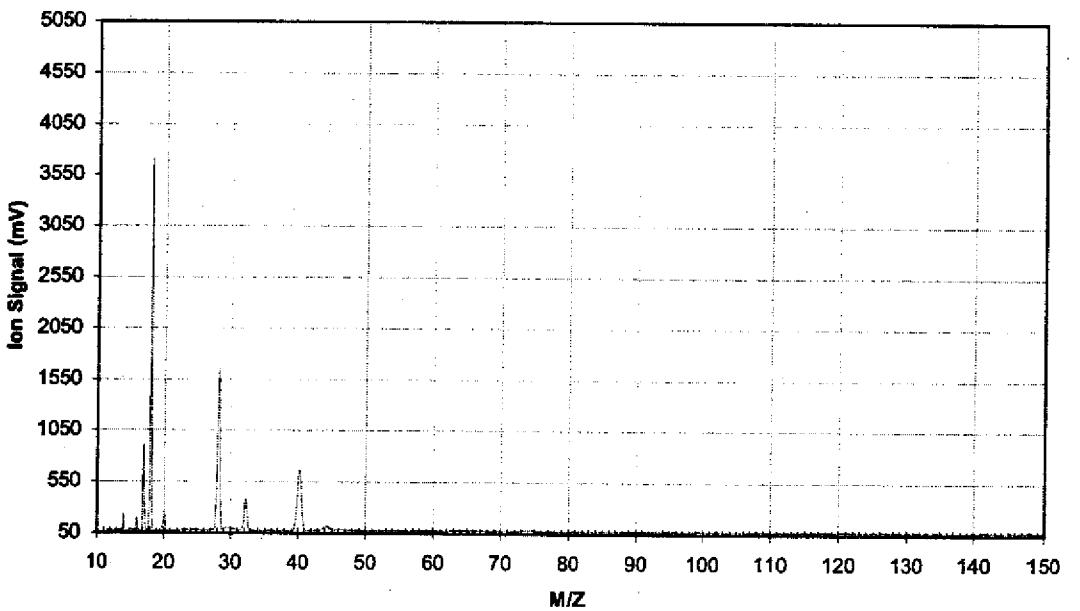

Figure 6-14: Boston Harbor spectrum at 12 meters depth

Methane, carbon dioxide and oxygen ion peak data exhibit obvious trends in the 3 to 4.5 meter depth range and then again at 12 meters depth. Given a mean high-water depth of 13 meters and the Harbor's soft mud bottom, the increase in these gases at 12 meters is apt to be the result of the instrument being near or partially buried within the uppermost portions of anoxic sediments. Simultaneous decrease in oxygen signals recorded at this depth by both the Hydrolab and NEREUS support an anoxic bottom sediment hypothesis. The causation of the methane and carbon dioxide ion signal increase in the upper depth range of 3 to 5 meters is less clear because they do not coincide with proportional decreases in oxygen or any observable deviation in salinity or temperature. A plausible explanation may be that this region of the water column contains effluent from nearby ship bilges and holding tanks or drainage culverts lining the Hoosac seawall (these drainage culverts lie at approximately 3 meters depth during high tide), but more investigation is needed to clarify the origin of this chemical feature.

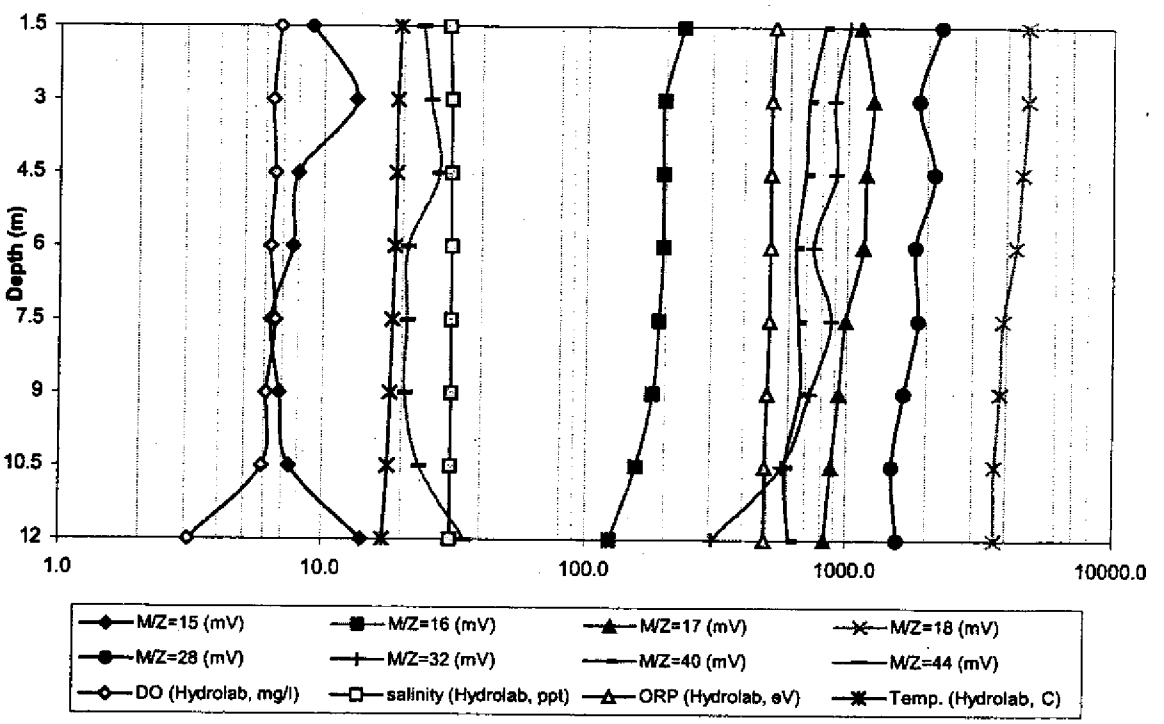

Figure 6-15: Depth profile of Boston Harbor

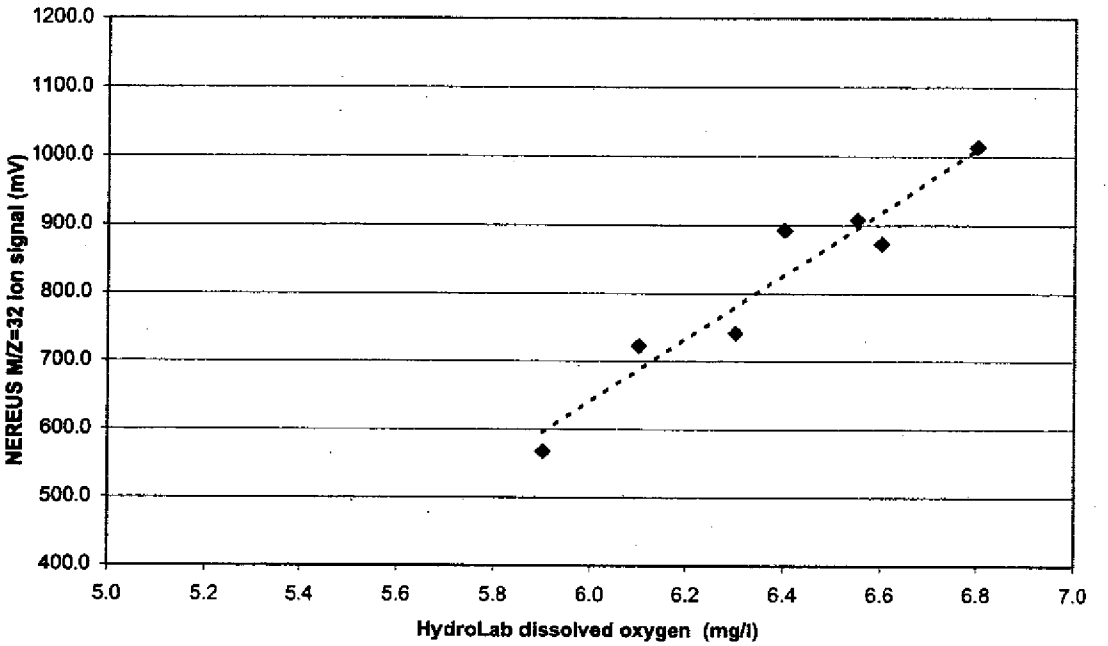

Figure 6-16: Oxygen signal correlation of NEREUS and Hydrolab data from Boston Harbor

NEREUS oxygen ion peak data at M/Z=32 exhibit a high degree of correlation with Hydrolab dissolved oxygen data, matching all trend slopes and yielding a statistical R^2 value of 0.93. The minimum NEREUS detection limit for oxygen is estimated to be approximately 4.62 mg/l, by applying a linear least squares line fit to this data and assuming a characteristic noise of 2.5 mV and a signal-to noise ratio of 3. This detection limit is roughly an order of magnitude higher than bench top estimates. However, given the overall peak height attenuation to approximately 1/5 of full scale, the instrument detection limits can be decreased to less than 1 mg/l by simply increasing electrometer gain or permitting more analyte influx (i.e. allowing greater permeable membrane surface area).

6.2 Towed deployment

After successfully completing buoyed deployment, the NEREUS instrument underwent towed deployment in the Upper Mystic Lake on December 13 and 15, 2002. The objectives of these deployments were to ascertain instrument performance when used

in a tow body configuration and to develop a detailed three-dimensional chemical map of this ice-covered lake.

The upper mystic lake is an eutrophic, dimictic, kettlehole lake with a surface area of approximately 50 hectares, volume of 7,000,000 m^3 and average depth of 15 m [101]. The lake sediment is contaminated with toxic metals, including: arsenic, cadmium, chromium, copper, and lead from industrial chemical and tannery waste release during the early 1900s [102]. Bathymetric features include a central basin with a maximum depth of 25 meters, and a shoal in the northern third of the lake with a maximum depth of 9 meters [103]. Prior investigations have observed a seasonal thermocline which appears in early spring, causing an anoxic hypolimnion to develop at a depth of 8 to 10 meters, and then gradually deepen over the course of fall. Observations indicate that the bottom 9 meters remain stratified into the winter. Oxygen depletion from biological respiration and redox cycling of metals causes the hypolimnion to become anoxic by early summer [104].

The first deployment on December 13 was conducted by "mowing the lawn" along transects mostly within the oxic epilimnion, while the second December 15 deployment focused more on carrying out transects across the epilimnetic/hypolimnetic interface. Both deployments made use of a 14' aluminum boat equipped with a 5 hp outboard motor and the tether apparatus to tow the instrument through the water. Boat velocity was kept to approximately 0.5 meters per second in order to minimize oscillatory motion of the instrument and prevent the tether from seizing in the ice layer which ranged in thickness from ¼" to 1". A sounding line rigged with a 25 lb. weight was suspended in front of and to a depth 2 meters below the towed instrument package, with the aim of contacting the lake bottom or submerged debris before the instrument package. The December 13 deployment used the external radio transceiver and float, whereas the December 15 deployment required that the radio transceiver be integrated inside the pressure sphere and a dummy plug for the MIL-9 electrical feed through so that the instrument could be sent to a depth of 25 meters (the MIL-9 radio transceiver cable is only 15 meters long). Total duration for both deployments was approximately 6 ½ hours. In this time period more than 300 spectrum scans were conducted (mass range 12-150 AMU, at 0.1 AMU intervals and 500 to 1000X signal averaging). Over 2/3 of these

spectra maintain sufficiently high signal-to-noise ratios to contain meaningful data. A major noise source appears to have been caused by microphonic vibration of the electrometer and faraday cup detector when the instrument tether strummed while being towed through the water and large sheets of broken ice. Nonetheless, the volume and quality of data collected during these brief deployments is unparalleled.

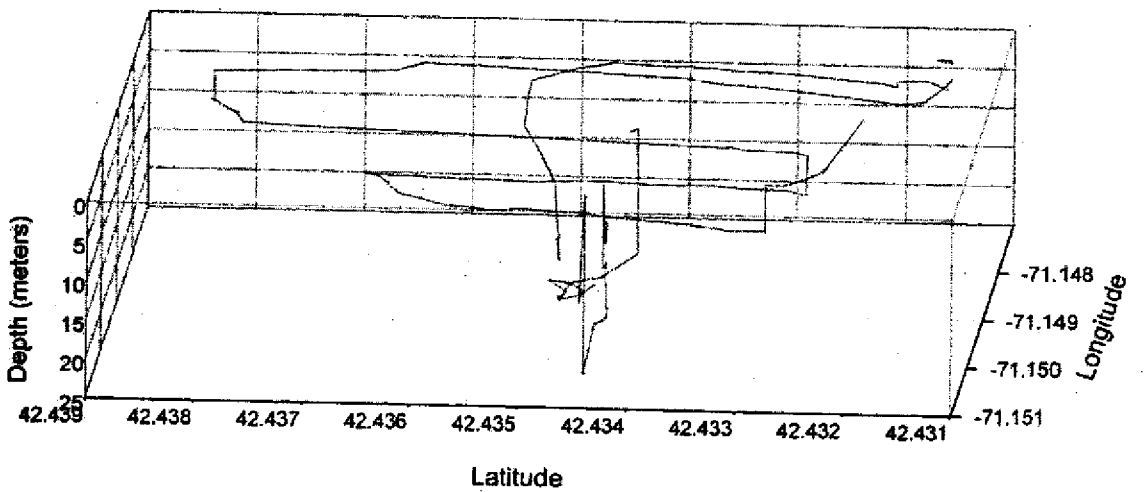

Figure 6-17: 3-D map of towed NEREUS deployments in Upper Mystic Lake

Hydrolab, conductivity and temperature data clearly show the presence two stratified layers, interfacing at a depth of approximately 13 meters. Hydrolab malfunctioning, due to battery failure in the cold winter temperatures, allowed only 54 of the NEREUS spectra to be compared with Hydrolab data. NEREUS and Hydrolab dissolved oxygen data trends generally parallel each other and correlation comparison reveal statistical R^2 values of 0.83 (Dec. 13) and 0.84 (Dec. 15) that are similar to the Boston Harbor tethered deployment. The decreased correlation between oxygen data may be caused by a spatial aliasing of up to 15 meters, providing sufficient time for one instrument to sample anoxic water in the hypolimnion and the other to sample oxic epilimnion water. This aliasing is due the boat's velocity of 0.5 m/s and asynchronous sampling as much as 30 seconds apart. Hydrolab dissolved oxygen data collected on December 13 exhibit relatively high variability at one and five meter depth transects (Figure 6-20). It is unknown whether this variability is due to dissolved oxygen heterogeneity at the sampled depth transects or

Hydrolab sensor drift. However, it is worthwhile noting that Hydrolab dissolved oxygen variability within the epilimnion is less pronounced within the December 15 data (Figure 6-21). Regression based extrapolation of December 13 data indicates that the NEREUS minimum detection limit for oxygen is in the range of 3 mg/l; while December 15 data suggests a detection limit of 0 mg/l when ion signal is below 75 mV.

Carbon dioxide peaks are clearly identified throughout the entire water column, and increase significantly as a function of depth below the thermocline (Figure 6-20, Figure 6-21). Although a methane signal at M/Z=15 is absent in the epilimnion, peaks begin to emerge at the thermocline and demonstrate an increasing trend with depth, similar to that of carbon dioxide. In contrast, NEREUS determinations of oxygen concentration remain relatively stable within the epilimnion, and decrease substantially within the hypolimnion. These chemical features are consistent with biologically induced anoxia and methanogenesis within the hypolimnion.

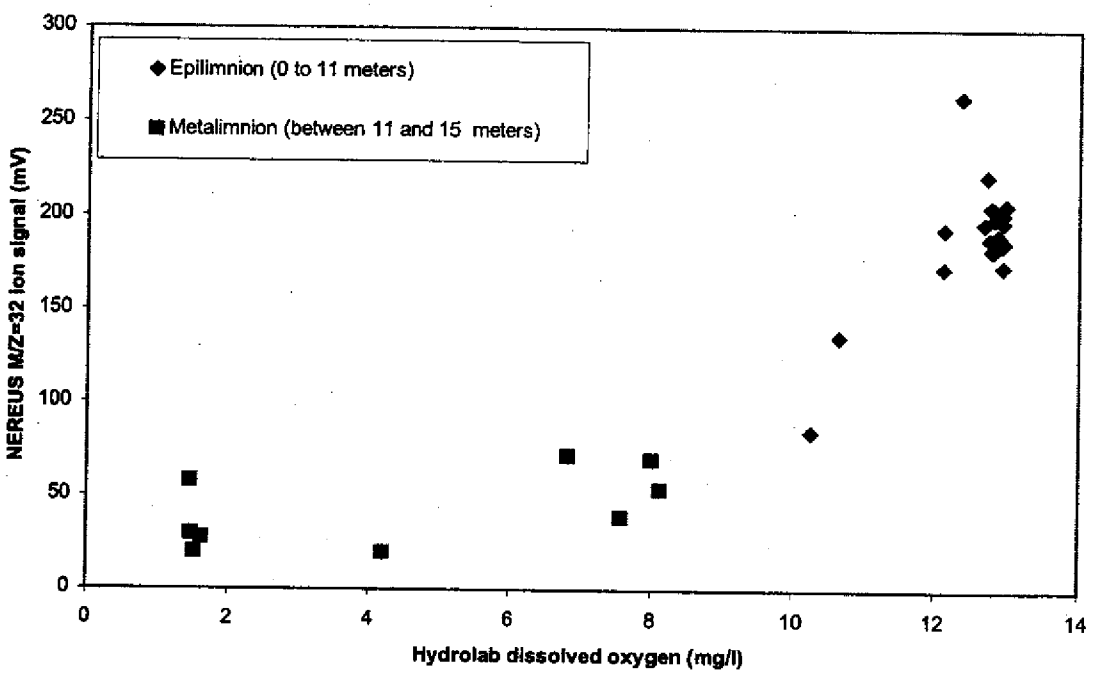

Figure 6-18: Oxygen signal correlation of NEREUS and Hydrolab data from Upper Mystic Lake, Dec. 13

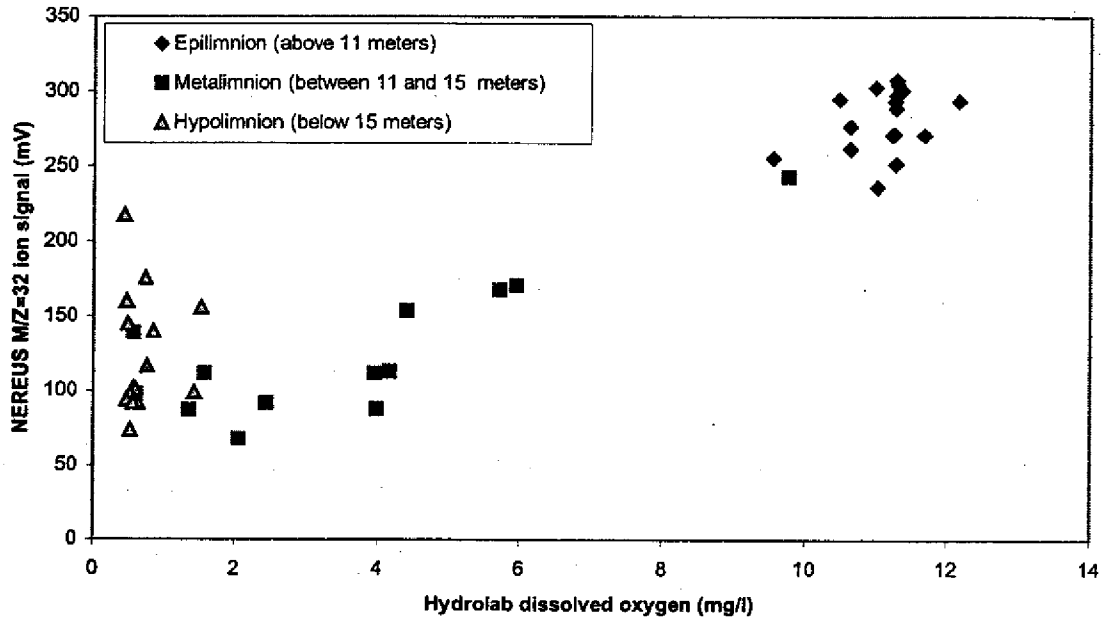

Figure 6-19: Oxygen signal correlation of NEREUS and Hydrolab data from Upper Mystic Lake, Dec. 15

The low water temperatures of 2 to 4° C decreased the instrument's inlet membrane permeability appreciably, attenuating peak heights by roughly a factor of 3. Furthermore, temperature variations are likely to cause increased permeability (and therefore increase ion signal strength) in the higher temperature hypolimnion over that of the epilimnion.

Ion peak amplitude differences across the two sampling days are most pronounced when comparing epilimnetic oxygen concentrations. Possible reasons for this may include increased photosynthetic productivity from one day to the next (although this is unlikely because of the continuous cloud cover and ice cover during these dates), influx of new waters from upstream sources (also unlikely due to a forebay residence time on the order of 10 days [105]), or most likely because of sensor drift. Sensor drift may be due to any of a number of factors, including variability in electrometer gain, variability in ionization efficiency, increased baseline signal (i.e. through decreased pumping efficiency of ion pump and gas buildup). The relative stability of carbon dioxide, methane, and hypolimnetic oxygen signals suggest that electrometer gain and ionization efficiency remain largely unchanged from one day to the next.

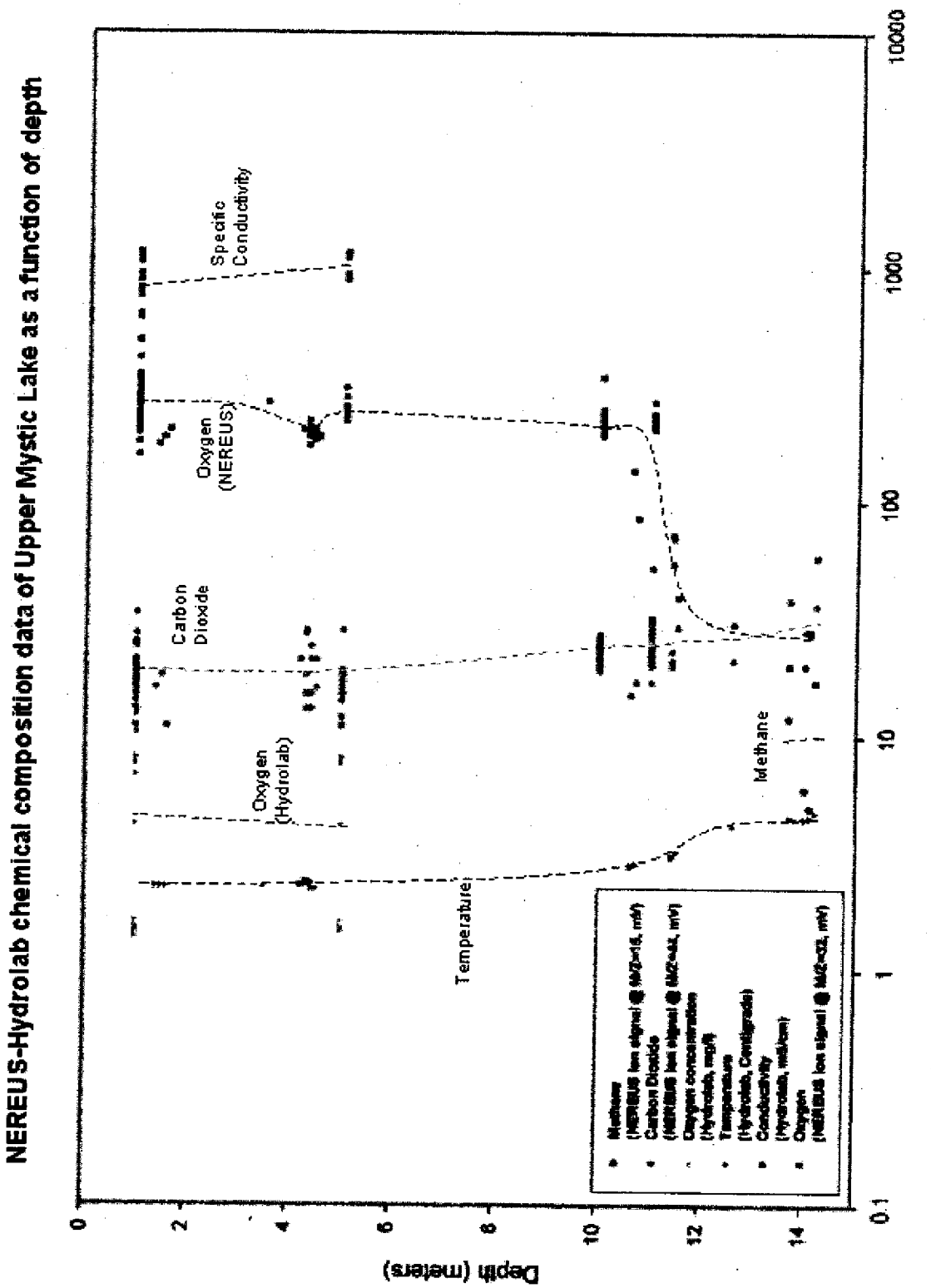

Figure 6-20: Chemical profile of Upper Mystic Lake, December 13, 2002

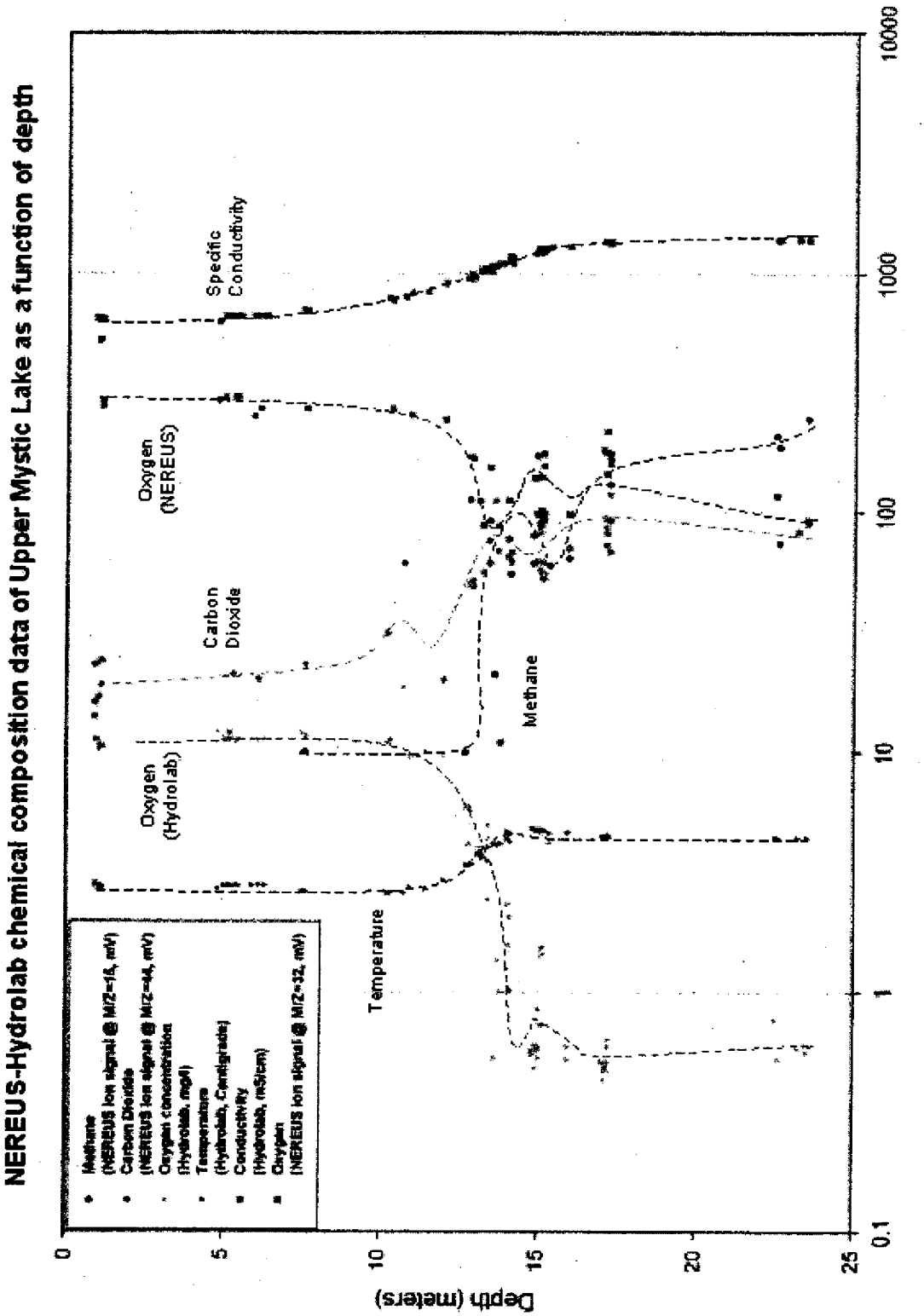

Figure 6-21: Chemical profile of Upper Mystic Lake, December 15, 2002

6.3 AUV deployment

On December 19 2002 the Kemonaut vehicle and NEREUS payload underwent sea trials in Boston Harbor demonstrating the cargo carrying capacity, maneuverability, and overall seaworthiness of the Kemonaut design as well as the ability of the NEREUS instrument to collect meaningful chemical data while operating onboard a moving AUV platform. A relatively confined region of Boston's Inner Harbor near to the Charles River Locks was selected for operations because of its unobstructed flat bathymetry, relatively low frequency of boat traffic during the winter months (compared to other regions of the harbor), and absence of underground tunnels or electrical cables thereby avoiding potential electromagnetic interference to the vehicle navigation system.

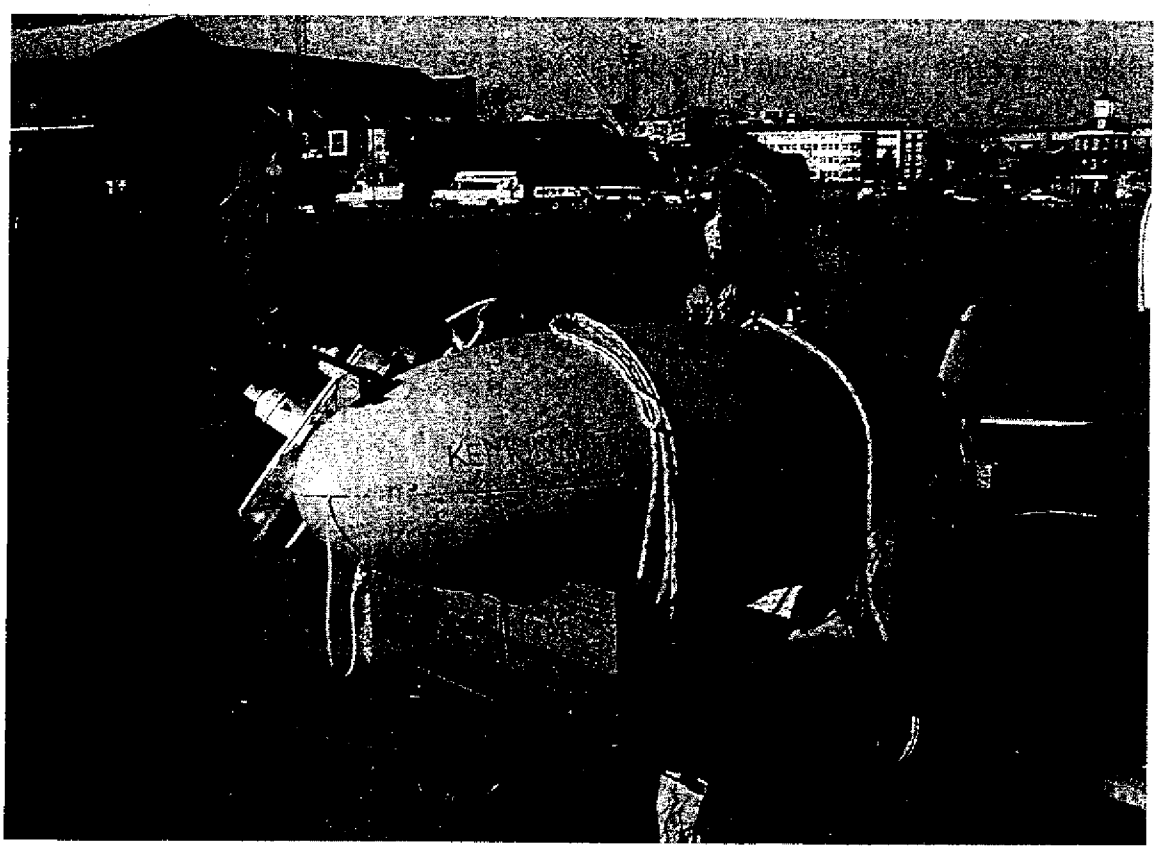

Figure 6-22:The Kemonaut AUV prior to deployment in Boston Harbor

Operations began with the deployment of four GIB buoys with attached hydrophones around the perimeter of the test area. These buoys were positioned in more or less a rectangular pattern to maximize the triangulation distance while minimizing propagation path obstructions and interference with shipping traffic. Buoy rodes were anchored in place using a 5 kg weight attached to 2 meters of 3/8" steel chain to prevent drift in the channel's +1 kt current and 3.5 meter tidal cycle.

Boston Harbor's Pier 4 served as the operations base station for radio communication with Kemonaut and crew aboard a skiff that served as an intercept boat. Operations base station was setup in the cargo bed of a Ryder truck, parked at the end of the pier to provide a clear view westward out over the Harbor.

Kemonaut was ballast tested for marine deployment from a two-ton electric hoist once GIB transponders were in position and functioning. Based on results from earlier freshwater ballasting, an additional 3.8 kg of weight had been fitted to the vehicle while undergoing assembly in the lab. This additional weight was distributed in two equally weighted 1.8 kg bags of lead shot. The first bag was zip-tie wrapped to the internal 10 lb dive weight in the nose of the vehicle, and the second weight was wired tightly to the external aft surface of the vehicle, directly below the two 10 lb dive weights, using 4 corrosive links. These corrosive links cause the ballast weight to be jettisoned after a period of 12 hours, thereby improving the prospects of successful recovery in the event of a vehicle system failure. Although theoretically buoyant for seawater, the vehicle proved to be correctly ballasted without any additional weight. Salinity tests confirmed the harbor water to be slightly brackish at 26-28 parts per thousand, thus helping to account for the density disparity. A small ~300 cc piece of floatation foam was added inside the bow of the vehicle to achieve neutral trim.

Kemonaut and NEREUS clock synchronization and systems checks were performed subsequent to ballasting. After satisfying all checks, the AUV was released from its lift hoist and towed into position using a 16 ft skiff equipped with a 35 hp outboard engine. Once in position, mission commands were relayed to Kemonaut from the base station using the spread spectrum radio modem and operations commenced once the vehicle was in position.

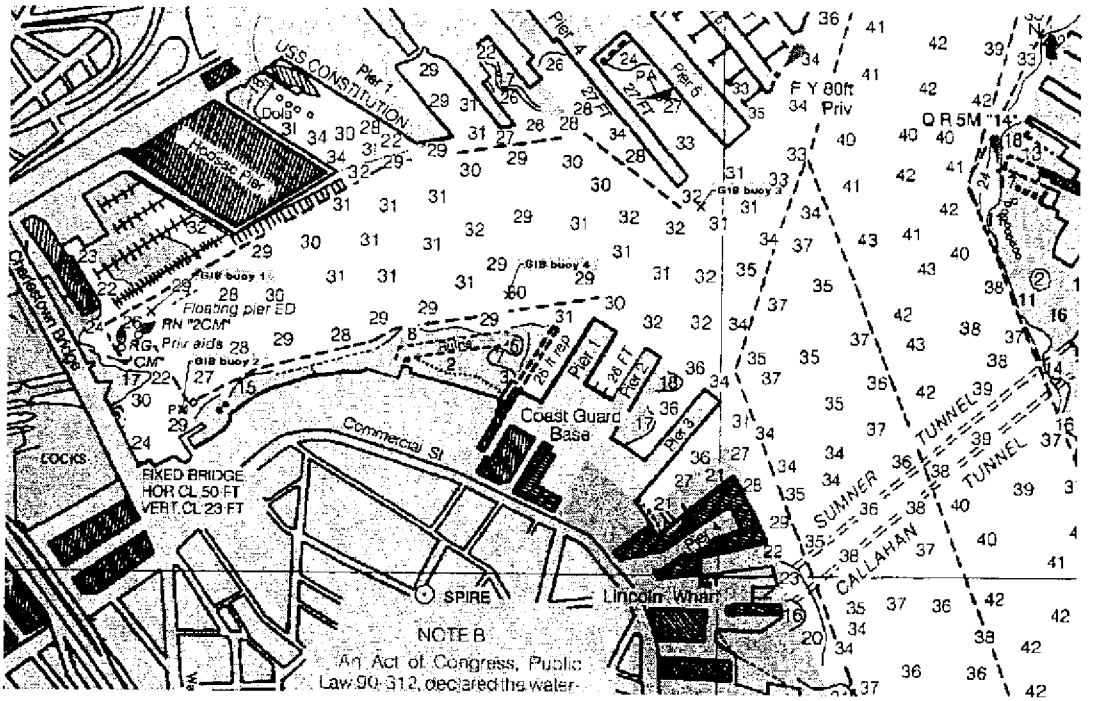

Figure 6-23:Nautical Chart of Boston Harbor showing GIB placement and overall area of operation

Two initial surface missions were conducted to verify proper vehicle tracking with the GIB hydrophone array, while maintaining visual contact. Following the two surface runs, Kemonaut performed a total of 6 submerged missions, ranging in duration from 2 to 6 minutes and reaching a maximum depth of 6.3 meters. Each dive mission was conducted as level, straight line, run for a specified time duration with the aim of reducing mission complexity and keeping altitude and heading reference system (AHRS) error from critically affecting the navigation system. The navigation system was set to abort its mission if the vehicle's sonar altimeter sensed a distance of less than 3 meters from the bottom to prevent the vehicle from colliding with the harbor bottom. The intercept boat tracked the submerged AUV using GIB hydrophone position fixes of the vehicle relayed verbally over VHF radio from the base station. After each dive the intercept boat was sent to visually inspect Kemonaut for obvious signs of damage and to prevent other nearby vessels from colliding with the somewhat concealed AUV. In

addition to visual inspection after surfacing, NEREUS instrument status was evaluated via a dedicated radio link from a laptop computer located in the intercept boat. As a measure of caution, missions were conducted at progressively deeper target depths of 2, 4 and 6 meters. Mission duration was also increased incrementally from 2 minutes on first dive to a maximum of 8 minutes on the sixth dive.

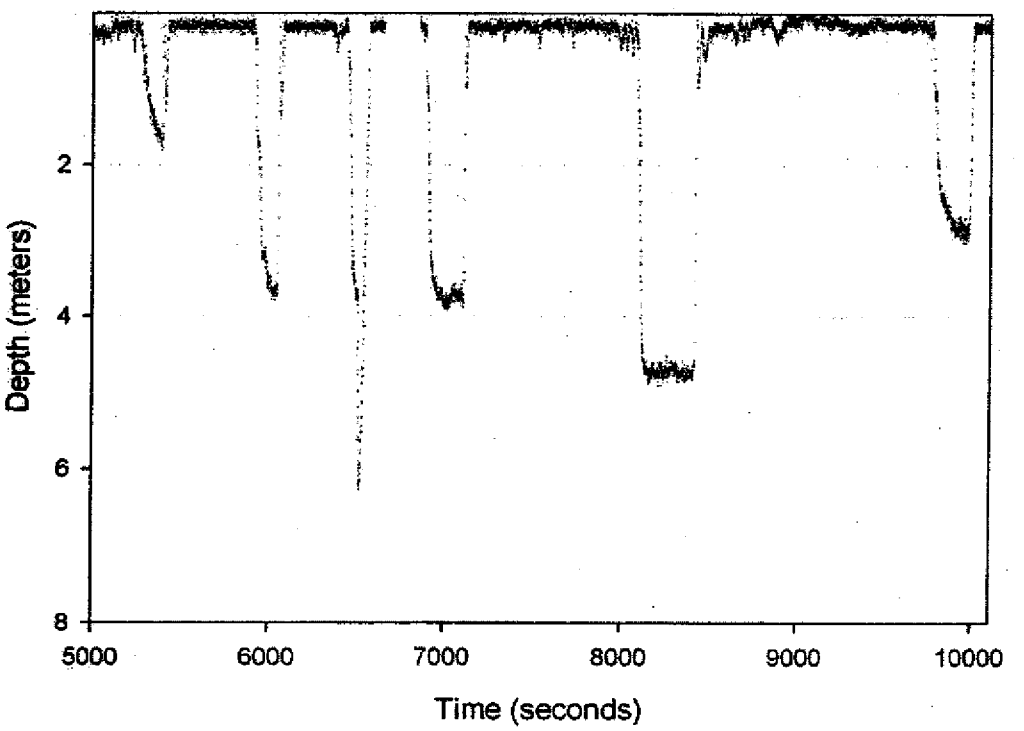

Figure 6-24: Kemonaut pressure transducer record

After satisfactory completion of its first and second dive to respective depths of 2 and 4 meters, Kemonaut was requested to dive to a depth of 6 meters on its third mission and reached a maximum depth of 6.3 meters before resurfacing. At the time it was unclear if the bottom avoidance override had been triggered by an acoustic return from an obstruction lying on the harbor bottom. Although later analysis of sonar altimeter data revealed that this had not been the case, in the interest of vehicle safety, a decision was made at that time to conduct the next dive at a depth of 4 meters, but with an increased mission duration of 5 minutes. Kemonaut executed this dive mission cleanly by quickly rotating itself nearly 180° to assume the proper heading and then maintaining its straight

course for the remainder of the mission, logging some 400 meters in distance. The fifth dive mission was setup to better ascertain the repeatability of the vehicle's navigation and control system by retracing this fourth dive. Consequently, Kemonaut was towed back to the vicinity of its previous starting position and instructed to dive to a depth of 5 meters for a duration of six minutes using the same heading as dive 4. Again, Kemonaut performed capably, following to within 1 meter of its previous track line for a distance of over 200 meters. The sixth and final dive mission was intended to further test the AUV's ability to maintain a straight and level track line and to allow the NEREUS instrument adequate time to collect multiple chemical spectra while at depth. Mission duration was specified for 8 minutes and a shallow depth of 3 meters was chosen in order to minimize the chances of bottom collision. The desired heading was increased in a similar attempt to prevent the AUV from being run aground on the ruins near the harbor channel's southern sea wall and Coast Guard piers. Despite these efforts, Kemonaut was forced to abort the dive mission approximately 4 minutes into the run because the human operator assigned heading had inadvertently directed the vehicle to swim in a northwesterly track, passing underneath the USS Cassin Young and a barge before swimming into a shallow dry dock area, causing the bottom avoidance override procedure to trigger, thus forcing the vehicle to surface.

Based on recorded MOOS pressure sensor data, Kemonaut has demonstrated a dive rate capability of up to 0.18m/s, and is able to maintain a prescribed depth to within ±0.3 meters (Figure 7). Despite uncertainties caused by variability in near-surface acoustic signal propagation, GIB hydrophone tracking revealed that Kemonaut was able to maintain a high degree of lateral accuracy (Figure 6-25, Figure 6-26). The extent of Kemonaut's dynamic control is evident when comparing the GIB track logs from dive missions four and five, particularly in light of the fact that these dives were performed while in the presence of a current with a flow rate exceeding 1.5 kts.

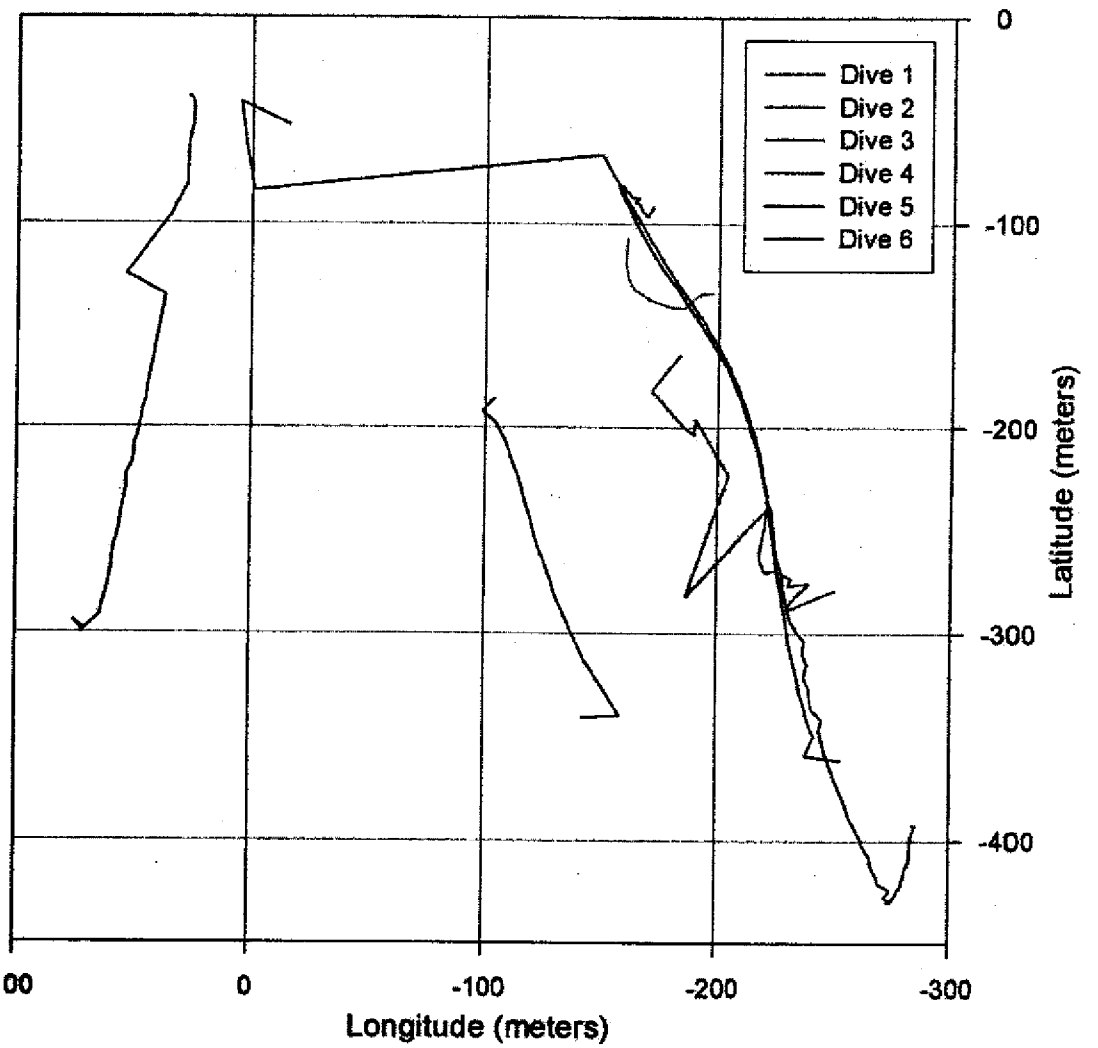

Figure 6-25: 2-D GIB hydrophone surface track log of Kemonaut dive missions

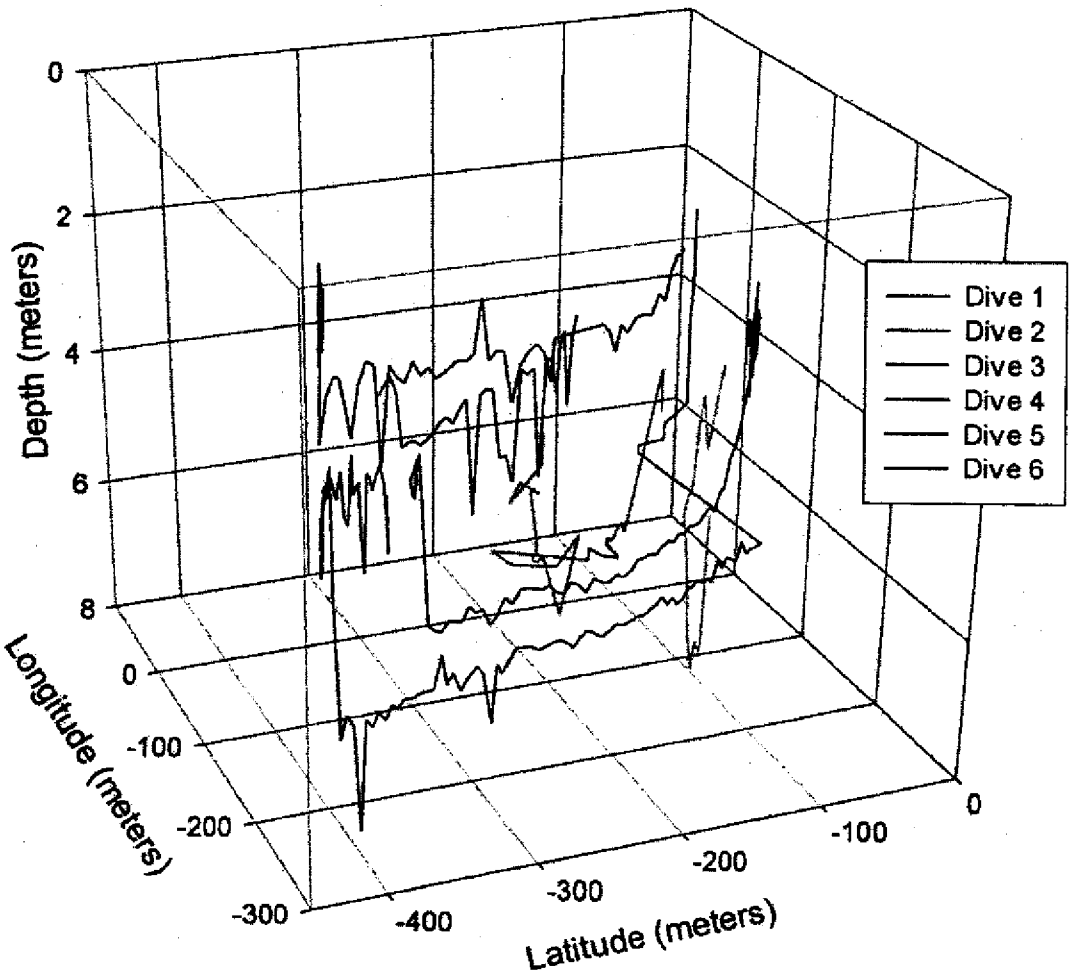

Figure 6-26: 3-dimensional GIB hydrophone track log of Kemonaut dive missions

The NEREUS instrument, which operated for the duration of its time aboard the Kemonaut vehicle, collected approximately 90 individual spectra over the course of these three hours, with each spectrum consisting of 693,000 discrete measurements. The NEREUS instrument appeared to be largely unaffected by vehicle motion through the water or vibration from the vehicle's propulsion and control system while underway.

The NEREUS instrument conducted spectral scans of volatile dissolved gases ranging in molecular weight from 12 to 150 Daltons while operating onboard Kemonaut. These scans were performed at a mass step interval of 0.1 Dalton to ensure that ion peak shape

could be clearly resolved. Signal averaging was kept to 500 samples per data point in an effort to minimize the amount of time required for a complete spectral scan while still maintaining an adequate S/N ratio. Automated radio communications between the instrument and its remote computer terminal (used for monitoring the instrument) were scheduled to occur during the electrometer stabilization period before the instrument took a measurement to further decrease time requirements. NEREUS was able to complete an entire scan once every 98 seconds using these techniques. Although spectral scans can be conducted much faster by further limiting the mass-to-charge range, mass step interval and signal averaging, this mode was chosen so that high molecular weight hydrocarbons could be clearly identified in the event of being encountered by the AUV.

Post-deployment analysis of NEREUS data revealed the presence of dissolved atmospheric gases, principally nitrogen, oxygen, and argon (Figure 6-27). Due to the cold temperatures encountered on this day (an air temperature of -5 to -1° C and a water temperature of 2 to 4° C) the instrument's inlet membrane permeability was significantly decreased, causing all spectra to exhibit attenuated peak heights. Nevertheless, relative ratios of these gases remained consistent with previous NEREUS data collected during buoyed deployment in this area of Boston Harbor. RMS noise was typically about 5 mV, but exhibited sudden dramatic increases, to hundreds of millivolts, appearing to coincide when the intercept boat occasionally bumped into the AUV while it was being towed.

NEREUS spectrum data was processed upon completion of the six dive missions to quantify ion peaks and then merged with MOOS track log data by way of time stamp synchronization. The resulting data shows a noticeable variability in dissolved gas concentration near the water's surface (Figure 6-28). This anomaly is likely to be the result of air bubble entrainment from breaking waves generated by the +20kt wind blowing that day. Further analysis of the data did not reveal the presence of any hydrocarbon fractions or xenobiotic molecules.

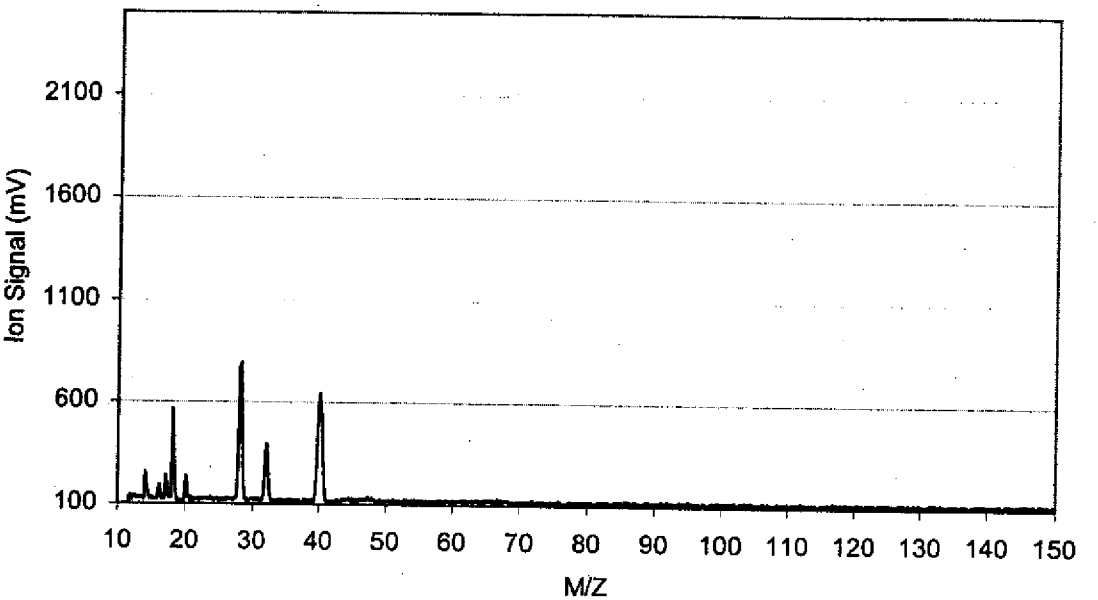

Figure 6-27: A typical NEREUS spectrum that was recorded while onboard the Kemonaut AUV, showing dissolved nitrogen, oxygen and argon.

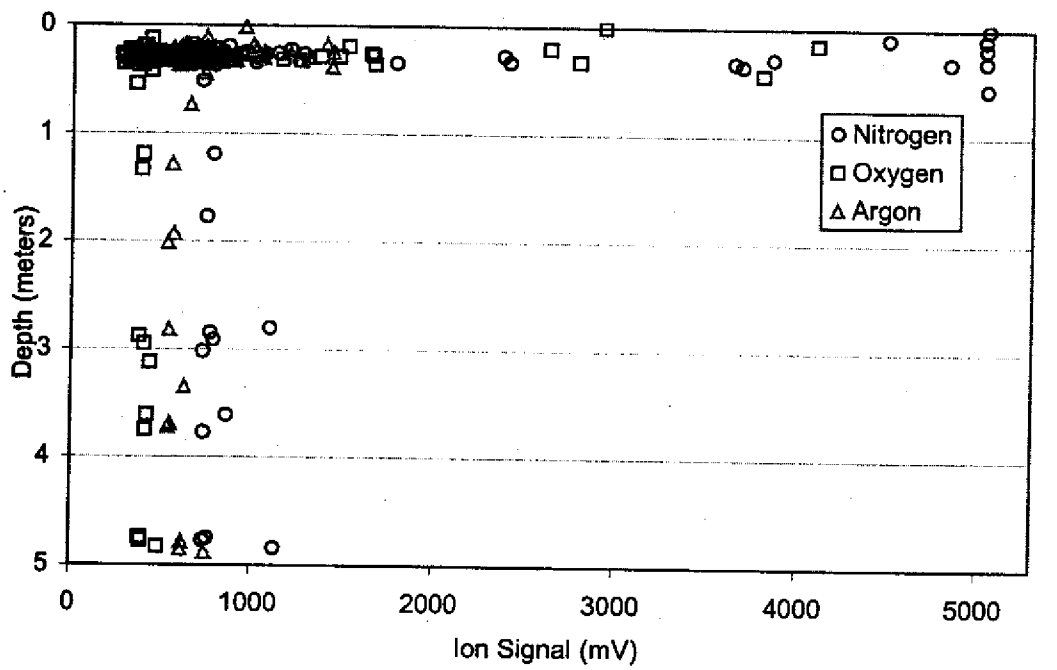

Figure 6-28: NEREUS record of dissolved gas ion signal during Kemonaut deployment in Boston Harbor

Chapter 7

CONCLUSIONS AND FUTURE WORK

Several capabilities of the NEREUS mass spectrometer and Kemonaut AUV were demonstrated through bench testing and deployments. These deployments rigorously tested the system's ability to not only survive in real-world environments but to collect meaningful data while operating in harsh environments such as an ice-covered lake, or a busy marine port. NEREUS met or exceeded all of the original design goals, including: size, power, weight, response time, depth capability, sensitivity, endurance and reliability. The Kemonaut vehicle has proven to be a small, easily deployable, low cost, yet robust platform with adequate stability and cargo carrying capacity to deploy the NEREUS instrument. Thus far, all tests and operations have been successfully completed without instrument or vehicle failure. Moreover, large quantities of scientifically valuable data were collected during these initial deployments. At present, the instrument and vehicle system is well suited for scientific assessment of dissolved gases in shallow, freshwater and coastal marine environments. Further research and development may greatly extend system usefulness by virtue of increased depth limit, greater detector sensitivity, elevated scan speed, multiple sensor integration, increased vehicle endurance and closed-loop navigation. It is worthwhile noting that the NEREUS instrument was constructed with a materials cost of approximately $5,000, and $3,000 for the Kemonaut vehicle. These budgetary constraints required that all hardware components be completed with just a single design and build iteration. Nearly all NEREUS components were fabricated by hand and, in several cases, component parts were fashioned from discarded materials found around the MIT campus. Kemonaut development was similarly challenging because it required in-house fabrication and was completed, from concept to vehicle deployment, in just six weeks. Despite these budgetary and time constraints, the Kemonaut-NEREUS system is a technologically advanced environmental data collection tool that offers new and unique capabilities for understanding the subsurface aquatic environment.

7.1 Toward routine operation

Kemonaut vehicle characteristics allow rapid, low-cost access to the subsurface; meanwhile, the NEREUS instrument is well suited for identifying chemical structures within this environment. Together, this platform and sensor permits straightforward, automated monitoring of dissolved gases such as nitrogen, carbon dioxide, methane and oxygen. Better understanding of role and variability of these gases in biogeochemical cycles are critical for insight into ecological, atmospheric, geologic and hydrologic dynamics. Several deployment missions are currently possible for the Kemonaut-NEREUS system in its current configuration, including detailed survey of small lakes, synoptic assessment of larger water bodies and calibration of chemical sensor networks.

The Kemonaut-NEREUS system is probably best suited for monitoring dissolved gases in lakes with simple bowl-shaped bathymetry, such as the Upper Mystic Lake. This type of environment is less challenging to navigation for a number of reasons. First, currents are generally below a few centimeters per second and the lake volume is relatively small, enabling full coverage by a single vehicle within a short period of time. Second, collision obstacles such as large debris resting proud of the bottom and deep draft vessels are not commonly present. Third it is unusual for lake bottom debris and geology to generate magnetic signatures of sufficient intensity to cause significant course deviations. Furthermore, the relatively short vehicle track lines do not permit large spatial deviations. Fourth, acoustic noise and reflections (i.e. from corrugated metal seawall pilings) are uncommon in such lakes, minimizing acoustic navigation error. Finally, although the corrosive drop weights are unlikely to function reliably in anoxic freshwater environments, the lake's small and closed volume facilitates recovery in the event of vehicle failure. Limnologic deployments may involve the vehicle swimming vertical sinusoids or maintaining fixed depth along a grid pattern to determine variations in stratification depth (*i.e.* when during a period of internal seiching) or localized chemical concentration heterogeneity.

More challenging freshwater deployments may include deployment in ice-covered Antarctic lakes. Many of these lakes are super-saturated with respect to nitrogen, oxygen, argon, and carbon dioxide, but the contributions of their biological and non-biological sources are not well understood [106]. Nitrogen, oxygen and argon gases together have

been used to determined the fraction of gas produced by biology compared to freezing and also determine the nature of the freezing process [107]. However, research indicates that significant variability in gas concentrations occur throughout the water column and sampling is limited by the time required to drill multiple boreholes in ice up to 5 meters thick as well as the abilities of scuba divers to collect subsurface samples [108]. NEREUS deployments in the Upper Mystic Lake has demonstrated its ability to operate within a frozen lake, and subsequent Boston Harbor deployment established that the instrument and AUV both operate satisfactorily in water temperatures less than 5°C. Thus, the Kemonaut-NEREUS system should be able to withstand the harsh Antarctic environment, and if equipped with a LBL navigation system may prove valuable not only in increasing the data collection rate, but also by eliminating the need for scuba divers to perform dangerous sample collection work below the thick ice cover.

Yet another type of near-term deployment can be monitoring of coastal marine areas for pollution from sewage or hydrocarbon spills. The instrument package could potentially be used in areas such as Boston Harbor, where recent cleanup efforts have lead to the creation of a new offshore outfall and the closing of sewage outfalls within the harbor [109]. The instrument and vehicle could easily identify areas of decreased oxygen and increased methane and carbon dioxide, which may help in identifying remaining pollution sources to the Harbor. This type of mission would only require simple straight-line surveys and therefore could be conducted using Kemonaut's existing navigation system.

7.2 System optimization

Although the instrument and vehicle met or exceeded their design goals, a few areas of potential improvement were identified, both in the instrument and vehicle, following the deployment tests. Each improvement is easily achieved with simple modifications to hardware components or algorithms. Improvements to NEREUS may include a modified inlet system, designed without recesses that trap gas bubbles within the inlet housing and a membrane mounting apparatus that permits easy membrane replacement and increased operational depth. The cycloid tube possesses a 180° sector analyzer and Faraday cup for M/Z = 1 to 12 scanning. This secondary analyzer, which is necessary for measuring

hydrogen gas and helium, can be utilized if a second electrometer and switching circuitry is incorporated. Redesign of the circuit to incorporate an "auto-zeroing" or "chopper-stabilized" operational amplifier [110] in its first gain stage may further increase electrometer signal-to-noise ratio by limiting electrometer bandwidth to a narrow range around 30Hz [111]. The dual electrometer configuration should also include a system for scalable electrometer gain (permitting greater dynamic ion peak measurement range) and additional vibration isolation (to damp vehicle or tow body vibration). Tow body vibration can also be decreased by enclosing the NEREUS instrument within a streamlined protective fairing and by using a short shock line (e.g. bungee cord) connected between the towline and the instrument to decouple surface craft motion and towline strumming from the instrument. Signal-to-noise characteristics of NEREUS data may benefit from additional post-processing techniques such as median filtering when the system is exposed to excessive vibration or impacts. A median filter for electrometer data can potentially help reduce noise by automatically rejecting sample outliers and thereby preventing large oscillatory signals from influencing data values (i.e. averaging only a subset of sample measurements that are centered about the median). Both the NEREUS instrument and Kemonaut AUV can benefit from high energy-density storage batteries such as rechargeable lithium polymer or lithium ion batteries. Further advance of navigation and signal processing software will improve accuracy and expand system capabilities. This may include the development of a closed loop navigation system augmented with navigation sensors such as a long base line (LBL) array, an active hydrophone and GIB transponder onboard the vehicle, a Doppler velocity log (DVL), or a high-precision spread-spectrum acoustic network such as the EXACT system. Finally, incorporation of an acoustic telemetry system will allow both Kemonaut and NEREUS to communicate with external agents while submerged, permitting its use as a nexus of chemical data, linking nearby fixed arrays such as sensor buoys that may be distributed throughout a body of water.

7.3 Sensor integration and real-time data interpretation

In-situ submerged deployment presents the challenges of monitoring large spatial volumes and highly dynamic environmental states when *a priori* knowledge is limited.

These factors, when combined with the limited communication bandwidth available to a maneuvering underwater platform, require that autonomous decision and control processes be employed. The NEREUS system uses an autonomous architecture to both control the instrument and interpret data in real time. However, data generated by other sensors (such as temperature, depth, height above bottom, salinity and various chemical parameters) remain external to the NEREUS decision control process. Instrument-platform control and data collection can be greatly enhanced through sensor integration and real-time data assimilation, thereby improving state-based decision processes and real-time forecasting of environmental conditions [79, 112]. For example, uniform temporal or spatial chemical sampling may be inefficient if a chemical feature is localized or intermittent. If a uniform coarse sampling strategy is used, the phenomenon may become aliased or be overlooked completely. Then again, a fine-scale sampling strategy may over sample, leading to monitoring inefficiency.

Currently, the NEREUS instrument uses an embedded type of expert system intelligence that allows the instrument to identify individual ion peaks and vary its sampling interval in real-time, according to the rate of change of ion signatures. Its capability to intelligently monitor multiple chemicals may be broadened through integration of other sensors onboard the Kemonaut AUV or with a distributed array of sensors using acoustic or radio telemetry. Such *in-situ* data distribution is advantageous because it cooperatively permits rapid, automated procedures such as in-situ calibration, data assimilation, forecasting, state-based monitoring, and chemotactic navigation (Camilli and Hemond 2002). Several sensor networks, including the LEO 15 [113] site off New Jersey's coast, and the proposed Neptune array [114] in the Pacific Ocean can potentially use the Kemonaut-NEREUS system to rapidly measure multiple ions across wide spatial domains, providing synoptic coverage of large-scale transient chemical phenomena, and to supplement data collected by other moored, drifting, ship-borne and airborne instruments.

7.4 Future prototypes

As new materials and technologies become available, more capable prototypes can be derived from the Kemonaut-NEREUS system's design. It is difficult to accurately predict

what types of innovations are ahead, but these future generations of autonomous submersible mass spectrometers and AUVs may include many of the promising technologies that are just now emerging. These may include new power systems such as fuel cells, which enable month-long, multi-thousand kilometer mission durations [115, 116]. Other AUV advances may include advanced vehicle control systems that permit vehicle hovering, and precise navigation even in energetic environments such as surf zones [117, 118]. Control system evolution may also permit more flexible missions through feature-based concurrent mapping, which incorporate environmental measurements in navigation estimation to improve navigational performance in unmapped environments [119]. These adaptive control systems may assimilate chemical data in real-time from an onboard mass spectrometer, making possible chemotactic navigation. In addition to higher-level instrument behaviors, future submersible mass spectrometers will be much smaller due to high-energy product rare-earth magnets and metals with increased B-field permeability [30]. Micro electro-mechanical systems (MEMS) will, undoubtedly, also cause overall sensor size to shrink considerably, reducing the vacuum requirements and thereby also decreasing the instrument's power requirement. It is conceivable that advances in MEMS and integrated circuit technologies will soon lead to the development of sub-centimeter-scale ion path length analyzers operating at pressures of a few Torr, permitting the use of much smaller, lower cost AUVs. At some point these mass spectrometers should diminish in size, power, and cost to a point that they can be carried as payload on miniature autonomous vehicles which can be simultaneously deployed as a self-configuring distributed network by a single person to cover an entire volume. Such systems will revolutionize the way we observe the aquatic environment, enabling an *in-situ* presence to explore and understand chemical processes at appropriate spatial and temporal frequencies.

REFERENCES

1. Cohen, J.E., et al., *Estimates of coastal populations.* Science, 1997. **278**(5341): p. 1211-1212.
2. Aristotle, *The Complete Works of Aristotle the Revised Oxford Translation*, in *Problems (Physika Problemata)*, J. Barnes, Editor. 1984, Princeton University: Princeton. p. 1514.
3. Edgerton, H.E., *Diving Deep on the Bathyscaphe*, in *MIT Institute Archives and Special Collections: Edgerton Collections.* 1988: Cambridge.
4. Ballard, R.D., *The History of Woods Hole's Deep Submergence Program*, in *50 Years of Ocean Discovery*, O.S.B.N.R. Council, Editor. 2000, National Academy Press: Washington, D.C. p. 67-84.
5. Fricke, J.R., *Down to the Sea in Robots*, in *Technology Review.* 1994. p. 46-55.
6. Brooks, R.A., *Flesh and Machines How Robots Will Change Us.* 2002, New York: Pantheon. 260.
7. Mindell, D.A., *Between Human and Machine Feedback,Control, and Computing before Cybernetics.* 2002, Baltimore: Johns Hopkins. 439.
8. Walter, W.G., *An Imitation of Life.* Scientific American, 1950. **182**(5): p. 42-45.
9. Walter, W.G., *A Machine that Learns.* Scientific American, 1953. **185**(5): p. 60-63.
10. Brooks, R.A., *A Robot that Walks; Emergent Behaviors from a Carefully Evolved Network.* 1989, Massachusetts Institute of Technology Artificial Intelligence Laboratory: Cambridge. p. 12.
11. Bernard, D., et al. *Spacecraft autonomy flight experience: The DS1 Remote Agent Experiment.* in *Proceedings of the AIAA Conference 1999.* 1999.
12. Bellingham, J.G., et al. *Performance Characteristics of the Odyssey AUV.* in *8th International Symposium on Unmanned Untethered Submersible Technology.* 1993. Portsmouth NH.: Autonomous Undersea Systems Institute.
13. Bellingham, J.G., *New oceanographic uses of Autonomous Underwater Vehicles.* Marine Technology Society Journal, 1997. **31**(3): p. 34-47.
14. Singh, H., D. Yoerger, and A. Bradley. *Issues in AUV Design and Deployment for Oceanographic Research.* in *Proceedings of the 1997 IEEE International Conference on Robotics and Automation.* 1997. Albuquerque: IEEE.
15. Purcell, M., et al. *New Capabilities of the REMUS Autonomous Underwater Vehicle.* in *Oceans 2000.* 2000. Providence, Ri.
16. Butler, B. and M.R. Black. *The Theseus AUV, Two Successful Missions.* in *Proceedings of the Tenth International Symposium on Unmanned Untethered Submersible Technology.* 1997. Lee, New Hampshire.
17. Bellingham, J.G., et al. *A Second Generation Survey AUV.* in *Proceedings of the IEEE Symposium on Autonomous Underwater VehicleTechnology (AUV '94).* 1994. Cambridge, Ma.: IEEE.
18. Bales, J.W. and E.R. Levine. *Sensors for Oceanographic Applications of Autonomous Underwater Vehicles.* in *AUVS-94.* 1994. Arlington: Association for Unmanned Vehicle Systems.

19. Thomson, J.J., *Cathode Rays.* The London, Edinburgh, and Dublin Philosophical Magazine, 1897. **44**: p. 293.
20. Kiser, R.W., *Introduction to Mass Spectrometry and its Applications.* 1965, Englewood Cliffs, Nj: Prentice-Hall. 356.
21. Thomson, J.J., *Rays of positive electricity and their application to chemical analyses.* 1913, London: Longmans, Green and Co. 132.
22. Thomson, J.J., *Multiply-charged Atoms.* The London, Edinburgh, and Dublin Philosophical Magazine, 1912. **24**(6): p. 668-672.
23. Syage, J.A., et al., *Field-portable, high-speed GC/TOFMS.* Journal of the American Society for Mass Spectrometry, 2001. **12**(6): p. 648-655.
24. Niemann, H.B., et al., *The Galileo probe mass spectrometer: Composition of Jupiter's atmosphere.* Science, 1996. **272**(5263): p. 846-849.
25. Palmer, P.T. and T.F. Limero, *Mass spectrometry in the US space program: Past, present, and future.* Journal of the American Society for Mass Spectrometry, 2001. **12**(6): p. 656-675.
26. Neuman, J.A., et al., *Fast-response airborne in situ measurements of HNO3 during the Texas 2000 Air Quality Study.* Journal of Geophysical Research-Atmospheres, 2002. **107**(D20): p. art. no.-4436.
27. Richardson, L.B., *Thesis: A field-usable membrane-probe mass spectrometer*, in *Deptartment of Civil Engineering.* 1988, Massachusetts Institute of Technology: Cambridge. p. 62.
28. Baykut, G. and J. Franzen, *Mobile Mass-Spectrometry - a Decade of Field Applications.* Trac-Trends in Analytical Chemistry, 1994. **13**(7): p. 267-275.
29. Hemond, H.F., *A Backpack-Portable Mass-Spectrometer for Measurement of Volatile Compounds in the Environment.* Review of Scientific Instruments, 1991. **62**(6): p. 1420-1425.
30. Sinha, M.P. and A.D. Tomassian, *Development of a Miniaturized, Lightweight Magnetic-Sector for a Field-Portable Mass Spectrograph.* Review of Scientific Instruments, 1991. **62**(11): p. 2618-2620.
31. Sinha, M.P. and G. Gutnikov, *Development of a Miniaturized Gas-Chromatograph Mass- Spectrometer with a Microbore Capillary Column and an Array Detector.* Analytical Chemistry, 1991. **63**(18): p. 2012-2016.
32. Takahashi, T., C. Wunsch, and e. al., *Applications in Analytical Chemistry to Oceanic Carbon Cycle Studies.* Oceanographic Measurements; Technologies for Chemical Measurements. 1993, Washington D.C.: National Academy Press. 85.
33. Johnson, J.E., *Evaluation of a seawater equilibrator for shipboard analysis of dissolved oceanic trace gases.* Analytica Chimica Acta, 1999. **395**(1-2): p. 119-132.
34. Park, S., *Surface Seawater Sampling Device During Navigation.* Ocean Research, 1995. **17**(1): p. 59-63.
35. Matz, G., W. Schroder, and G. Kibelka, *Submersible Membrane Introduction - Gaschromatograph - Mass Spectrometer.* unpublished, Technische Universitat Hamburg-Harburg.
36. Short, R.T., et al., *Underwater mass spectrometers for in situ chemical analysis of the hydrosphere.* Journal of the American Society for Mass Spectrometry, 2001. **12**(6): p. 676-682.

37. Kibelka, G., et al., *Underwater Mass Spectrometry for Detection of VOCs and Dissolved Gases*. unpublished, Center for Ocean Technology Applied Microsystems Ltd.
38. Hemond, H.F. and R. Camilli. *Underwater Mass Spectrometers: Some Critical Engineering Issues*. in *Third Workshop on Harsh-Environment Mass Spectrometry*. 2002. Pasadena, Ca.
39. Camilli, R., *Thesis: The Development of Components for an In-situ Mass Spectrometer*, in *Department of Civil and Environmental Engineering*. 2000, Massachusetts Institute of Technology: Cambridge. p. 102.
40. Einfeld, W., et al., *Environmental Technology Verification Report*. 1997, US Environmental Protection Agency, Office of Research and Development: Washington DC. p. 1-78.
41. Poel, L.v.d., *Product Survey on Commercial AUVs*, in *Hydro International*. 2002. p. 37-39.
42. Conrad, R. and W. Seiler, *Methane and Hydrogen in Seawater (Atlantic-Ocean)*. Deep-Sea Research Part a-Oceanographic Research Papers, 1988. **35**(12): p. 1903-1917.
43. Schmidt, U. and R. Conrad, *Hydrogen, Carbon-Monoxide, and Methane Dynamics in Lake Constance*. Limnology and Oceanography, 1993. **38**(6): p. 1214-1226.
44. Scranton, M.I., P. Donaghay, and J.M. Sieburth, *Nocturnal Methane Accumulation in the Pycnocline of an Anoxic Estuarine Basin*. Limnology and Oceanography, 1995. **40**(4): p. 666-672.
45. Tilbrook, B.D. and D.M. Karl, *Methane Sources, Distributions and Sinks from California Coastal Waters to the Oligotrophic North Pacific Gyre*. Marine Chemistry, 1995. **49**(1): p. 51-64.
46. Brekke, T., O. Lonne, and S.E. Ohm, *Light hydrocarbon gases in shallow sediments in the northern North Sea*. Marine Geology, 1997. **137**(1-2): p. 81-108.
47. Deangelis, M.A. and M.I. Scranton, *Fate of Methane in the Hudson River and Estuary*. Global Biogeochemical Cycles, 1993. **7**(3): p. 509-523.
48. Chen, G.T. and F.J. Millero, *Gradual Increase of Oceanic Co2*. Nature, 1979. **277**(5693): p. 205-206.
49. Whiticar, M.J., *Diagenetic relationships of methanogenesis, nutrients, acoustic turbidity, pockmarks and freshwater seepages in Eckernforde Bay*. Marine Geology, 2002. **182**(1-2): p. 29-53.
50. Scranton, M.I. and K. McShane, *Methane Fluxes in the Southern North-Sea - the Role of European Rivers*. Continental Shelf Research, 1991. **11**(1): p. 37-52.
51. Frenzel, P., B. Thebrath, and R. Conrad, *Oxidation of Methane in the Oxic Surface-Layer of a Deep Lake Sediment (Lake Constance)*. Fems Microbiology Ecology, 1990. **73**(2): p. 149-158.
52. Dafner, E., A. Obzhirov, and O. Vereshzhagina, *Distribution of methane in waters of the Okhotsk and western Bering Seas, and the area of the Kuril Islands*. Hydrobiologia, 1998. **362**: p. 93-101.
53. Diaz, J.A., C.F. Giese, and W.R. Gentry, *Mass spectrometry for in-situ volcanic gas monitoring*. Trac-Trends in Analytical Chemistry, 2002. **21**(8): p. 498-514.

54. Sutton, A.J., et al., *Implications for eruptive processes as indicated by sulfur dioxide emissions from Kilauea Volcano, Hawai'i, 1979-1997.* Journal of Volcanology and Geothermal Research, 2001. **108**(1-4): p. 283-302.
55. Tsunogai, U., et al., *Peculiar Features of Suiyo Seamount Hydrothermal Fluids, Izu- Bonin Arc - Differences from Subaerial Volcanism.* Earth and Planetary Science Letters, 1994. **126**(4): p. 289-301.
56. Lilley, M.D., M.A. Deangelis, and L.I. Gordon, *Ch4, H-2, Co and N2o in Submarine Hydrothermal Vent Waters.* Nature, 1982. **300**(5887): p. 48-50.
57. Kodera, M., G. Igarashi, and M. Ozima, *Noble-Gases in Hydrothermal Plumes of Loihi Seamount.* Earth and Planetary Science Letters, 1988. **87**(3): p. 266-272.
58. Gamo, T., et al., *Methane Anomalies in Seawater above the Loihi Submarine Summit Area, Hawaii.* Geochimica Et Cosmochimica Acta, 1987. **51**(10): p. 2857-2864.
59. Sigurdsson, H., *Kick'em Jenny*, R. Camilli, Editor. 2002, personal communication.
60. Robertson, R., et al., *The explosive eruption of Soufriere Hills Volcano, Montserrat, West Indies, 17 September, 1996.* Geophysical Research Letters, 1998. **25**(18): p. 3429-3432.
61. Robertson, R.E.A., *An Assessment of the Risk from Future Eruptions of the Soufriere Volcano of St-Vincent, West-Indies.* Natural Hazards, 1995. **11**(2): p. 163-191.
62. Ishibashi, J.I., et al., *Helium and Carbon Geochemistry of Hydrothermal Fluids from the North Fiji Basin Spreading Ridge (Southwest Pacific).* Earth and Planetary Science Letters, 1994. **128**(3-4): p. 183-197.
63. Karl, D.M., C.O. Wirsen, and H.W. Jannasch, *Deep-Sea Primary Production at the Galapagos Hydrothermal Vents.* Science, 1980. **207**(4437): p. 1345-1347.
64. Alper, J., *Oases in the oceanic desert.* ASM American Society for Microbiology News, 1990. **56**(10): p. 536-538.
65. Tsunogai, U., et al., *Fresh water seepage and pore water recycling on the seafloor: Sagami Trough subduction zone, Japan.* Earth and Planetary Science Letters, 1996. **138**(1-4): p. 157-168.
66. Bussmann, I. and E. Suess, *Groundwater seepage in Eckernforde Bay (Western Baltic Sea): Effect on methane and salinity distribution of the water column.* Continental Shelf Research, 1998. **18**(14-15): p. 1795-1806.
67. Fingas, M. and C. Brown, *Remote sensing of oil spills.* Sea Technology, 1997. **38**(9): p. 37-&.
68. Fingas, M. and C. Brown, *A review of the status of advanced technologies for the detection of oil in and with ice.* Spill Science & Technology Bulletin, 2000. **6**(5-6): p. 295-302.
69. Lehr, W., J. Galt, and e. al. *Tracking the North Cape Oil Spill.* in *Proceedings of the 19th Arctic and Marine Oilspill Program.* 1996. Calgary.
70. Wang, Z.D., et al., *Characterization and source identification of hydrocarbons in water samples using multiple analytical techniques.* Journal of Chromatography A, 2002. **971**(1-2): p. 173-184.
71. Hoch, J. and B. Kok, *A Mass Spectrometer Inlet System for Sampling Gases Dissolved in Liquid Phases.* Archives of Biochemistry and Biophysics, 1963. **101**: p. 160-170.

72. Allen, G., *Final Report: Mass Spectrometers*. 1996, Massachusetts Institute of Technology: Unpublished: Cambridge.
73. Maden, A. and M. Hayward, *Sheet Materials for Use as Membranes in Membrane Introduction Mass Spectrometry*. Analytical Chemistry, 1996. **68**: p. 1805-1811.
74. Robinson, C.F. and L.G. Hall, Review of Scientific Instrumentation, 1956. **27**: p. 504.
75. Bleakney, W. and J.A. Hipple, *A New Mass Spectrometer with Improved Focusing Properties*. Physical Review, 1938. **53**: p. 521-528.
76. Brooks, R.A., *A.I. Memo 864: A Robust Layered Control System For a Mobile Robot*. 1985, Massachusetts Institute of Technology: Cambridge. p. 1-25.
77. Russell, S. and P. Norvig, *Artificial Intelligence a Modern Approach*. 1995, Upper Saddle River, Nj.: Prentice Hall. 932.
78. Carver, S.J., et al., *Evaluating field-based GIS for environmental characterization, modeling and decision support*. International Journal of Heographical Information Systems, 1995. **9**(4): p. 475-486.
79. Vivoni, E.R. and R. Camilli, *Real-time Streaming of Environmental Field Data*. Computers and Geosciences, 2002. **29**(4): p. 457-468.
80. Gates, S.C. and J. Becker, *Laboratory Automation using the IBM PC*. 1989, Englewood Cliffs Nj.: Prentice Hall. 322.
81. Bellingham, J.G., et al. *A small long range vehicle for deep ocean exploration*. in *Proceedings International Offshore and Polar Engineering Conference*. 1992. San Francisco.
82. Curtin, T.B., et al., *Autonomous Ocean Sampling Networks*. Oceanography, 1993. **6**(3): p. 86-94.
83. Schmidt, H., et al. *Real-Time Frontal Mapping with AUVs in a Coastal Environment*. in *Oceans 96 MTS/IEEE*. 1996. Ft. Lauderdale, Florida.
84. Manley, J. and J. Rieffel, *GOATS 2000 September 25-October 12, 2000 AUV Operations Report*. 2000, MIT Sea Grant. p. 13.
85. Chryssostomides, C., *MIT Reports to the President, Sea Grant College Program*. 2001, Massachusetts Institute of Technology.
86. Newman, P., *This is the MOOS*, in http://oceanai.mit.edu/pnewman/MOOS/. 2000, MIT Sea Grant.
87. Manley, J., *AUV Sea Trials March 6 - 15, 2002 Key West, Florida Operations Report*. 2002, MIT Sea Grant AUV Laboratory: Cambridge. p. 15.
88. Damus, R., S. Desset, and J. Morash, *Xanthos vehicle control system*, R. Camilli, Editor. 2002.
89. Doherty, R.E., *An Algorithm for Mixture Component Determination For Use In Membrane Inlet Mass Specrometry*, in *Civil Engineering*. 1987, Massachusetts Institute of Technology: Cambridge. p. 272.
90. Brandrup, J., E.H. Immergut, and E.A. Grulke, eds. *Polymer Handbook*. 4th ed. 1999, Wiley-Interscience: New York.
91. Weiss, R.F., *The solubility of nitrogen, oxygen and argon in water and seawater*. Deep-Sea Research, 1970. **17**: p. 721-725.
92. Comyn, J., *Polymer Permeability*. 1985, New York: Elsevier Applied Science.
93. Varian, *Ion Pumps- vacuum products from Varian*. 2001.
94. Allen, G., *Comprehensive Polymer Science*. 1989, New York: Pergamon.

95. Crank, J., *The Mathematics of Diffusion*. 1975, Oxford University Press: New York.
96. Jenkins, R., P. Nelson, and e. al., eds. *Transactions of the Faraday Society*. 1970.
97. Wick, L.Y. and P.M. Gschwend, *By-products of a former phenol manufacturing site in a small lake adjacent to a Superfund site in the Aberjona watershed.* Environmental Health Perspectives, 1998. **106**: p. 1069-1074.
98. Wick, L.Y., et al., *Fate of benzene in a Stratified Lake receiving contaminated groundwater discharges from a Superfund site.* Environmental Science & Technology, 2000. **34**(20): p. 4354-4362.
99. Eganhouse, R.P. and P.M. Sherblom, *Anthropogenic organic contaminants in the effluent of a combined sewer overflow: impact on Boston Harbor.* Marine Environmental Research, 2001. **51**(1): p. 51-74.
100. Futo, I. and H. Degn, *Effect of Sample Pressure on Membrane Inlet Mass-Spectrometry.* Analytica Chimica Acta, 1994. **294**(2): p. 177-184.
101. Senn, D.B., *Thesis: Coupled Arsenic, Iron, and Nitrogen cycling in Arsenic-Contaminated Upper Mystic Lake*, in *Department of Civil and Environmental Engineering*. 2001, Massachusetts Institute of Technology: Cambridge MA. p. 284.
102. Spliethoff, H.M. and H.F. Hemond, *History of toxic metal discharge to surface waters of the Aberjona Watershed.* Environmental Science & Technology, 1996. **30**(1): p. 121-128.
103. Fricker, P.D., *Thesis: The Effect of Stratification and Bathymetry on Internal Seiche Dynamics*, in *Department of Civil and Environmental Engineering*. 2000, Massachusetts Institute of Technology: Cambridge MA. p. 174.
104. Senn, D.B. and H.F. Hemond, *Nitrate controls on iron and arsenic in an urban lake.* Science, 2002. **296**(5577): p. 2373-2376.
105. Andradottir, H., *Thesis: Circulation and Mixing in the Upper Forebay of the Mystic Lake System, Winchester, Massachusetts*, in *Civil and Environmental Engineering*. 1997, Massachusetts Institute of Technology: Cambridge. p. 109.
106. Andersen, D.T., C.P. McKay, and R. Wharton, *Dissolved gases in perennially ice-covered lakes of the McMurdo Dry Valleys, Antarctica.* Antarctic Science, 1998. **10**(2): p. 124-133.
107. Craig, H., R.A. Wharton, and C.P. McKay, *Oxygen Supersaturation in Ice-Covered Antarctic Lakes - Biological Versus Physical Contributions.* Science, 1992. **255**(5042): p. 318-321.
108. McKay, C.P., *personal communication on sampling methods in frozen Antarctic lakes*, R. Camilli, Editor. 2002.
109. Signell, R.P., H.L. Jenter, and A.F. Blumberg, *Predicting the physical effects of relocating Boston's sewage outfall.* Estuarine Coastal and Shelf Science, 2000. **50**(1): p. 59-71.
110. Horowitz, P. and W. Hill, *The Art of Electronics*. 2nd ed. 1989, New York: Cambridge University Press. 1125.
111. Landhal, C.E. and R.G. Merryman, *Modifications to CEC 21-620 Mass Spectrometer for Increased Sensitivity*. 1960, Los Alamos Scientific Laboratory of the University of California: Los Alamos NM. p. 1-20.

112. Camilli, R. and H.F. Hemond. *Multisensor Data Integration and Adaptive Sampling Strategies for an Autonomous Underwater Mass Spectrometer.* in *Third Workshop on Harsh-Environment Mass Spectrometry.* 2002. Pasadena, Ca.
113. Laursen, A.E. and S.P. Seitzinger, *The role of denitrification in nitrogen removal and carbon mineralization in Mid-Atlantic Bight sediments.* Continental Shelf Research, 2002. **22**(9): p. 1397-1416.
114. Delaney, J.R. and A.D. Chave, *NEPTUNE: A fiber-optic 'telescope' to inner space.* Oceanus, 2000. **42**(1): p. 10-11.
115. Aoki, T. and T. Shimura, *Fuel Cell for Long-Range AUV.* Sea Technology, 1997. **38**(8): p. 69-73.
116. Rudd, E.J. and D.W. Gibbons, *High energy density aluminum/oxygen cell.* Journal of Power Sources, 1994. **47**: p. 329-340.
117. Curico, J.A., F.S. Hover, and J.G. Bellingham, *CETUS: Design of a Production AUV.* Sea Technology, 1998. **39**(12): p. 10-17.
118. Hillenbrand, C., *UUV Science & Technology Trends.* Sea Technology, 1997. **38**(12): p. 10-15.
119. Smith, C.M., et al. *Feature-based concurrent mapping and localization for autonomous underwater vehicles.* in *Proceedings of IEEE Oceans.* 1997.